PARTIALLY AVERAGED NAVIER-STOKES METHOD FOR TURBULENCE CLOSURES: CHARACTERIZATION OF FLUCTUATIONS AND EXTENSION TO WALL BOUNDED FLOWS

A Dissertation

by

SUNIL LAKSHMIPATHY

Submitted to the Office of Graduate Studies of
Texas A&M University
in partial fulfillment of the requirements for the degree of
DOCTOR OF PHILOSOPHY

May 2009

Major Subject: Aerospace Engineering

PARTIALLY AVERAGED NAVIER-STOKES METHOD FOR TURBULENCE CLOSURES: CHARACTERIZATION OF FLUCTUATIONS AND EXTENSION TO WALL BOUNDED FLOWS

A Dissertation

by

SUNIL LAKSHMIPATHY

Submitted to the Office of Graduate Studies of
Texas A&M University
in partial fulfillment of the requirements for the degree of

DOCTOR PHILOSOPHY

Approved by:

Chair of Committee,	Sharath S. Girimaji
Committee Members,	Paul Cizmas
	Prabir Daripa
	Hamn-Ching Chen
Head of Department,	Dimitris Lagoudas

May 2009

Major Subject: Aerospace Engineering

ABSTRACT

Partially Averaged Navier-Stokes Method for Turbulence Closures: Characterization of Fluctuations and Extension to Wall Bounded Flows. (May 2009)

Sunil Lakshmipathy, B.E., Bangalore University;
M.S., Texas A&M University
Chair of Advisory Committee: Dr. Sharath S. Girimaji

The work presented in this dissertation concerns continued development, validation and verification of the partially averaged Navier-Stokes (PANS) method – a variable resolution closure model for turbulence. Linear eddy viscosity models (LEVM), which are popular because of their simplicity and affordability in terms of computational cost have fundamental deficiencies and cannot be trusted to accurately represent turbulence in realistic complex flows. The more high fidelity approaches such as large eddy simulations (LES) and direct numerical simulations (DNS) are out of realm of engineering applicability because of their high requirements in computing power. PANS, a variable resolution approach considered in this study, lies between LEVM and LES in terms of computational cost and is designed to prudently utilize the available computing power to improve accuracy.

This dissertation presents the various studies performed to characterize the PANS fluctuations and extend the model for use in various wall bounded flows. The road map towards our goal includes: (i) Comparing *a-priori* and *a-posteriori* eddy viscosity values to establish whether PANS is capable of producing the pre-specified level of reduction. (ii) Investigating the scaling of PANS fluctuations for different levels of prescribed resolution and establishing if the fluctuations abide by known turbulence scaling laws. (iii) Extending PANS to k-ω formulation which is better suited for wall-bounded shear flows, and (iv) Modifying the present LEVM to yield reasonable behavior in the rapid distortion limit where the turbulence is elastic in nature which ultimately affects PANS performance.

Results reported in this dissertation illustrate that the PANS closure yields reliable and predictable reduction in the modeled viscosity. The accuracy of the simulations improve as the effective damping is reduced by lowering the specified viscosity providing credibility to the PANS method as a bridging model that performs as intended.

ACKNOWLEDGEMENTS

I would like to express my sincere gratitude to my graduate advisor Dr. Sharath Girimaji for his guidance, generous support and patience during my graduate studies. I have been privileged to be a part of his research group. His advice in the subject matter as well as other research matters has definitely helped in shaping my professional qualities. I would like to thank Drs. Paul Cizmas, Prabir Daripa and Hamn-Ching Chen for serving on my graduate committee. The courses that I have taken under them have provided the knowledge to pursue my research effectively. I would especially like to thank Dr. Paul Cizmas and Dr. Prabir Daripa for their interest in my research and for their insightful comments which has helped in improving this dissertation.

I would like to thank Dr. Ravi Srinivasan for his valuable suggestions during my research and for discussing the intricacies of CFD and graduate life during the numerous coffee breaks that we took. His input has been helpful in the success of this work. I would like to acknowledge the support of my fellow graduate students in the turbulence research group including Sawan Suman, Gaurav Kumar, Dasia Reyes, Rebecca Bertsch, Sriram Arasanapalai and Anand Mishra for those enjoyable sessions that we had to discuss the various aspects of turbulence thereby enriching my knowledge in this field and making my research enjoyable. I would also like to thank my former colleague Eunh-Wan Jeong who laid the groundwork for this research.

The staff of the aerospace engineering department has been extremely helpful in making sure that the department is an enjoyable place to work. I would like to thank Ms. Colleen Leatherman and Ms. Karen Knabe for the arrangement of many administrative matters.

Finally, I would like to thank the Texas A&M Supercomputing facility for providing me access to their computing resources.

I am indebted to my family who made a lot of sacrifices for my success. Their endless support and encouragement was instrumental in completing this work.

TABLE OF CONTENTS

LIST OF FIGURES

LIST OF TABLES

CHAPTER I

INTRODUCTION

1. Background

The objective of this research is to aid in the development and validation of a new variable resolution (VR) turbulence model for engineering applications. Traditional turbulence models fall at opposite extremes of the computational demand spectrum. The Reynolds-averaged Navier Stokes method (RANS), steady or unsteady, widely considered the default model for simulating turbulent flows in today's industry is computationally the least expensive model. Current computing-power has outgrown the computational demand posed by RANS [1]. These models are generally of low fidelity in complex flows. Conversely, the more accurate large-eddy simulations (LES) and direct numerical simulations (DNS) are restricted in their application because of their high requirements in computing power [2]. Recent research efforts are directed towards development of VR methods that lie between RANS and LES in terms of computational cost and are designed to prudently utilize the available computing power to improve accuracy. Increase in the accuracy of the model is achieved by resolving more scales of motion than RANS, but significantly lesser than a typical LES.

As discussed by Spalart [3], turbulent flow predictions involve two principal challenges: 1) prediction of growth and separation of the turbulent boundary layer and 2) momentum transfer after separation. The RANS models fail to address challenge 1 because the geometry-dependent dynamically active scales of motion are not amenable to the Reynolds averaging process. Furthermore, RANS models inhibit mixing of the separated boundary layer. The Partially-averaged Navier Stokes (PANS) model proposed by Girimaji [4] and the turbulence model of interest in this study is able to resolve these

---

This dissertation follows the style of *Journal of Turbulence*.

geometry dependent scales and model the smaller scales of motion which are amenable to statistical averaging. PANS, based on Sagaut [5], can be classified as a universal VR model that can be tuned via a rescaling factor to be RANS accurate or DNS accurate. PANS is not zonal and the rescaling factor is active everywhere within the domain thus eliminating any transition effects.

PANS can seamlessly vary the rescaling factor smoothly between DNS and RANS and hence has the capability to optimize the physical fidelity of the solution with the available computing-power. The premise of using the PANS model is to capture the large unsteady scales of motion by placing the cut-off in the inertial range of the energy spectrum and model the high frequency part of the spectrum using modified RANS models. A significant portion of the energy spectrum (more than LES) is modeled thereby placing additional emphasis on the accuracy of the closure model. We use two-equation RANS model which is purported for modeling the entire turbulence spectrum to provide closure for the unresolved flow field. The aim is to decrease the modeled viscosity from its parent RANS value leading to weaker damping of the larger wave numbers thereby enabling the computational grid to resolve these unsteady energy-containing active scales of motion. The decrease in the eddy-viscosity is achieved by modifying the transport equations of the original RANS model. How well RANS performs as a sub-filter stress (SFS) model is a challenging question addressed in this study.

The advantages of VR models are that they provide intermediate accuracy at intermediate costs. Improved accuracy by increasing scale resolution in simulating turbulent flows comes at the cost of increasing computing power. The growing trends in computer power demands use of more sophisticated closure models for turbulence so as to capture the massive separation in complex geometry more accurately and VR models are aptly suited for such applications. There are a number of VR models being proposed and being pushed into mainstream application without adequate investigation of the model validity. Therefore this study is aimed at validating the PANS turbulence model by analyzing the performance of the model via simulating fundamental flow situations which pose challenging complexities for the model to capture.

2. Research Description

PANS, the VR model of interest in this study, is a seamless bridging model that can vary its resolution from RANS to DNS depending on the rescaling factors f_k and f_ε. f_k is the ratio of unresolved to total turbulent kinetic energy and f_ε is the ratio of unresolved dissipation rate to total dissipation rate. Since, closure for the SFS is obtained using RANS model the scaling of the SFS term is achieved by modifying the transport equations of the original RANS models such that the modified eddy-viscosity obtained from these equations is less than the original RANS eddy-viscosity. Smaller the rescaling factor. Finer should be the grid resolution.

PANS is among several VR models currently being proposed. Some of the VR models being tested include Detached Eddy Simulations (DES) [6], Unsteady-RANS (U-RANS) [7], very large eddy simulation (VLES) [2], hybrid RANS/LES, Flow Simulation Methodology (FSM) [8], and Limited Numerical Scales (LNS) [9] method. DES is a zonal approach in which the gray area is the transition region between RANS and LES. VLES, U-RANS, FSM, LNS and PANS are based on modifying the original RANS model.

Preliminary analysis of the PANS model performed by Girimaji [4] has demonstrated promising performance of PANS as an effective VR model. Current work builds on the previous work [4, 10, 11] to further validate and formally analyze the PANS model performance.

3. Research Contribution

In the present work the research emphasis is on validation of the PANS modeling paradigm. In the course of this research we seek answers to the following queries which would define our research objectives and facilitate in establishing the modeling prowess of PANS.

- Can modeled viscosity be controlled in a pre-specified manner? – addressed in study 1
- Are the fluctuations physical? – addressed in study 2
- Can the near-wall behavior be improved? - addressed in studies 3 & 4
- Can commutation errors be minimized? – not addressed in this dissertation

3.1. Study 1. Viscosity ratio recovery

This study focuses primarily on two strategies used by adaptive eddy-viscosity schemes to achieve the accuracy-on-demand paradigm. In the first, used by PANS, the reduction in the modeled viscosity is achieved by modifying the RANS model transport equations. The transport equations are now functions of the rescaling factor. In the second, used by LNS, FSM, U-RANS and VLES, the reduction in the modeled viscosity is achieved by modifying the coefficient C_μ in the Boussinesq relation. The present study compares the merits of the two proposals by analyzing whether the reduction in the modeled viscosity is achieved to the extent specified.

3.2. Study 2. Length and time scales in VR models

The objective of this study is to better characterize the fluctuations obtained from VR models. Characterization of the modeled turbulent flow field is an important aspect in turbulence model development. Many VR models produce fluctuations that could be spurious and not amenable to turbulence physics. A common feature of VR models is to place the cut-off in the inertial range of the energy spectrum. For such a cut-off, modeling becomes an important issue and to evaluate the performance of the sub-filter stress model, we need a detailed characterization of the modeled flow field. In RANS, the modeled flow field is characterized by describing the evolution of the representative turbulent length and time scales. In grid-based VR methods, the only available information about the modeled flow field is the modeled viscosity. Therefore, it is difficult to characterize the modeled turbulent flow field without being able to construct the representative length and time scales. In viscosity-prescribed VR methods, the available information about the modeled flow field include statistics of the unresolved eddy viscosity ν_u, unresolved kinetic energy k_u, and unresolved dissipation ε_u. Availability of additional information in viscosity prescribed methods enables better characterization of such closure models and thus helps in understanding its performance. We perform simulations to demonstrate that the PANS fluctuations (i) scale in a self similar manner for different cut-off wavenumbers; (ii) self similar scaling is similar to DNS scaling and (iii) the scaling follows standard turbulence scaling arguments.

3.3. Study 3. PANS k_u-ω_u model formulation and validation

In this study we first develop the k-ω version of the PANS model. Then we will analyze the performance of the PANS k_u-ω_u model based on the SFS closure model. Previous work [10, 11] in PANS modeling was performed using the RANS k-ε model as the closure model for the sub-filter stresses. The PANS k_u-ω_u formulation takes advantage of the superiority of the k-ω model over the k-ε model in the near-wall region. RANS k-ω model is known to be numerically more stable than the k-ε model primarily in the viscous sub-layer of the boundary layer. The value of specific dissipation rate, ω, is well defined near the wall as opposed to ε. We demonstrate that PANS k_u-ω_u model predicts the turbulent kinetic energy behavior close to the solid boundary with good accuracy in comparison to the PANS k_u-ε_u model.

3.4. Study 4. New variable C_μ model for turbulence in the rapid distortion limit

The PANS model inherits the properties of its parent RANS model and hence when PANS is applied to flows where turbulence to mean shear time scale ratio (Sk/ε) is much higher than typical values as in out-of equilibrium turbulent flows, it is unable to predict a physically realistic flow field. The reasons for this anomalous behavior are investigated in RANS perspective. Modifications to the standard model are proposed to render these models to better predict turbulence in this scenario. These modifications involve varying the model constant C_μ depending on the normalized strain rate, and normalized rotation rate. Proposed modifications for the C_μ model are based on rapid distortion analysis since the state of turbulence for large Sk/ε is governed by rapid distortion theory (RDT). The proposed C_μ models are validated for flow past an airfoil at maximum lift condition. Results from this simulation show that the model predicts realizable stresses at all times and provide a more accurate representation of the flow field.

4. Test Cases

Validation of the PANS model and the realizability based model is performed by simulating established test cases using CFD tools. The test cases chosen are:

4.1. Backward facing step flow

The backward facing step (BFS) flow is a test case with a simple geometry but complex flow features. The separation in this case is induced by a geometric singularity i.e. the step. The boundary layer which separates at the step reattaches downstream forming primary and secondary recirculation zones under the separated boundary layer. The separation, reattachment and redevelopment of the turbulent boundary layer along with the large vortical structures pose a complex flow pattern for the turbulence models to capture.

4.2. Cylinder flow

Flow past a circular cylinder incorporates a range of flow features that makes this a challenging test for any turbulence model to predict. It involves separation that is not induced by a geometric singularity but rather by surface curvature. The thin separated shear layers interact in the wake to produce large scale vortices. This case tests the capability of the model to address the issue of growth and separation of the turbulent boundary layer in adverse pressure gradient flows.

4.3. Airfoil flow

The airfoil flow is a test case that includes several complex flow phenomena such as laminar-to-turbulent transition, streamline curvature, growth and separation of the turbulent boundary layer. At the leading edge of the airfoil, the flow encounters large strain rates due to curvature of the geometry. The experiments predict the flow near the leading edge to be laminar. Modeling this flow field using a turbulence model becomes complicated as the flow experiences a state of turbulence that is difficult to capture using standard RANS model.

Simulated flow field of the above test cases using the turbulence models of interest in this research are compared with published experimental observations and numerical results. We perform both qualitative and quantitative analysis of the results for a thorough understanding of the performance of the turbulence models.

5. Dissertation Outline

The papers which discuss the studies listed in Sections 3.1 – 3.4 are presented in this dissertation as Chapters starting from Chapter III. Chapter II addresses the numerical issues associated with performing the various computations to achieve the research objectives. Chapter III presents the paper which investigates the filtering consistency in

PANS. A comparison between two different approaches to achieve hybridization is presented and evaluated. In Chapter IV, a new framework to characterize the PANS fluctuations is presented. Formalization and validation of the PANS k_u-ω_u model is presented in Chapter V. In Chapter VI, the modification of the RANS model to extend the model applicability to turbulence in the RDT limit is proposed and evaluated for airfoil flow. A successful validation of the modified RANS model for out-of-equilibrium turbulence situations would lead to better PANS closure models. Finally, Chapter VII summarizes the important conclusions from each of the studies performed. The figures and tables referred in various chapters are presented in Appendix A.

CHAPTER II

NUMERICAL VALIDATION

1. Introduction

The test cases described in the previous chapter are simulated using the Fluent CFD package. The capabilities of this package are summarized in Lakshmipathy [12]. The nature of the PANS governing equations which are formally derived in Chapter V allow for easy implementation of the model in any Navier-Stokes solver with RANS turbulence model. In this dissertation the rescaling factors f_k and f_ε are maintained constant for the entire domain and are not a function of space. The minimum f_k chosen for the cylinder flow simulation and backward facing step simulations are $f_k = 0.5$ and f_k 0.4 respectively. Smaller f_k values would require larger grids and smaller time-steps tending towards the extreme limit of PANS which is DNS. The various PANS simulations are performed by modifying the RANS model parameters as per the desired viscosity reduction to be achieved (See Chapter IV).

2. Cylinder Flow

Three PANS computations were performed to study the effect of grid refinement for the cylinder flow test case with f_k set to 0.5 which is the smallest f_k simulated for the cylinder flow test case. Having a grid that can support $f_k = 0.5$ resolution would yield a grid independent solution for any of the higher f_k (≥ 0.5) computations. The grid details for the three runs are presented in Table 1.

The *medium* grid has about 1/3rd more points in the streamwise as well as in the radial direction compared to the *coarse* grid. The grid resolution in the spanwise direction for both these grids is identical. Another level of refinement for the grid is performed in the radial and spanwise direction to generate the *fine* grid.

Figure 1 presents the mean streamwise velocity statistics along the wake centerline obtained from the three different grids simulated. In the near-wake region, all three grids predict the separation bubble of similar size. In the far-wake region, the *medium* and the *fine* grid simulations show very similar behavior for the mean velocity statistics Adding more points in the streamwise direction for the fine grid runs produces discernible variation of the mean velocity statistics in this direction. The mean streamwise velocity statistics at two different locations in the near-wake region (x/D = 1.0 and x/D = 3.0) are shown in Figure 2. The *medium* grid and the *fine* grid simulations show identical behavior for this velocity statistics. The *coarse* grid shows a shallower velocity defect at x/D = 3.0 compared to the *medium* and *fine* grid results. The time-averaged distribution of coefficient of pressure on the cylinder surface for the three PANS computations plotted in Figure 3 show that the there is no significant variation of the wall statistics with grid refinement. Figure 1, Figure 2 and Figure 3 clearly show that the results obtained from *medium* grid computation is adequate enough to accurately represent the performance of PANS model computations with $f_k = 0.5$. The PANS calculations for $f_k = 0.5$ is grid insensitive in the medium to fine range.

3. Backward Facing Step Flow

A grid resolution study for the BFS case is performed using a 2D domain for the smallest f_k considered in this study which is $f_k = 0.4$. Performing the grid resolution study for the smallest f_k would automatically ensure grid independent results for the other f_k value computations performed using the same grid. Three grids are considered for the grid resolution study labeled as coarse, medium, and fine. The details of these grids are presented in Table 2. Figure 4 compares the performance of various grids in predicting the coefficient of friction (C_f) along the bottom wall. The coarse grid predicts the separation to occur further away from the step whereas the medium and fine grid results predict a shorter reattachment length. The medium and fine grid results are very close to one another and there is no significant change in the results as we increase the grid resolution. This plot concludes that the medium grid is sufficient enough to get trustworthy results.

Results from the time-step study for the medium grid are presented in Figure 5 which shows the C_f distribution along the bottom wall. Two cases were simulated to study the time-step dependency on the results. In the first case ‘dt1’, the time-step advancement was established so that the minimum CFL condition was less than 5. In the second case ‘dt2’, the time-step was increased by 10 orders of magnitude. As can be observed, the two plots present identical results for the C_f distribution implying that the coarser time-step would provide sufficiently accurate results.

CHAPTER III

EXTENSION OF BOUSSINESQ TURBULENCE CONSTITUTIVE RELATION FOR BRIDGING METHODS[*]

1. Introduction

Bridging models [13, 14] are purported for turbulence simulations at any degree of resolution between Reynolds averaged Navier-Stokes (RANS) and direct numerical simulations (DNS). By combining the advantages of RANS and large eddy simulations (LES), bridging models – much like hybrid methods – offer an adaptive balance between computational effort and accuracy. The computational paradigm is one of accuracy-on-demand: fine resolution when the complexity of flow physics or accuracy requirement demands it and coarse resolution, even RANS, at other times. In a typical bridging method computation, the intent is to resolve dynamically crucial large scales and model all the other scales of motion (including inertial range). Thus, by resolving more scales of motion than RANS, but substantially lesser scales than LES, these methods potentially offer improved accuracy over RANS at a computational cost substantially lower than standard LES. The cut-off between resolved and unresolved scales is dictated by the local grid size and can, in principle, vary in time and space in a calculation for most efficient utility of the numerical grid.

The overall accuracy of a bridging computation depends on the combination of numerical resolution which determines the cut-off length scale and the physical fidelity of the constitutive relation, which supplies the subgrid eddy viscosity or stress for a given cut-off. If the closure model is poor, high numerical resolution alone cannot yield the best possible results on a given grid. Therefore, it is imperative that we combine maximum affordable resolution with the best possible closure model. For a given grid, a successful bridging calculation involves three major elements: (i) Controlled and

---

[*] Reprinted with permission from “Extension of Boussinesq turbulence constitutive relation for bridging methods” by Lakshmipathy, S., and Giriamji, S. S., 2007, *Journal of Turbulence*, **8**(31), 1 - 21.

predictable reduction of eddy viscosity from RANS value (ii) leading to the physical liberation and computation of more scales of motion (iii) resulting in improved accuracy of calculation as more scales are computed directly and accurately.

While the bridging computational paradigm is very appealing, modeling eddy viscosity as a function of cut-off length scale can be very challenging. If the cut-off is in the dissipation range, one can invoke the equilibrium assumption – production balances dissipation locally at the cut-off wavenumber – leading to a Smagorinsky-type algebraic relation between unresolved eddy viscosity and cut-off length scale:

$$\nu_u \sim \Delta^2 S \tag{3.1}$$

where Δ is the grid-size and S is the resolved strain rate magnitude. The implicit assumption here is that the spectral cut-off length scale is equal to grid size. In general, when the cut-off is located at larger scales, a more sophisticated eddy viscosity relation is needed –

$$\nu_u = \nu_u(u_u, l_u) \tag{3.2}$$

where u_u and l_u are the velocity and length scales that characterize the unresolved motion. To motivate a general closure model for the unresolved eddy viscosity valid for cut-off at any scale of motion, we look to the tried and tested RANS two-equation model.

Two-equation turbulence closure model with the Boussinesq constitutive relation has long been used for RANS turbulence computations. The Boussinesq eddy viscosity hypothesis relates the turbulent stresses to the mean strain:

$$\left\langle u_i u_j \right\rangle = \frac{2}{3} k \delta_{ij} - 2 \nu_T S_{ij} \tag{3.3}$$

where $\left\langle u_i u_j \right\rangle$ is the turbulent stress, k is the turbulent kinetic energy, δ_{ij} is the Kronecker delta, ν_T is the turbulent eddy viscosity, and S_{ij} is the mean strain field. The eddy viscosity is given by

$$\nu_T = C_\mu \frac{k^2}{\varepsilon} \text{ where } u_u = k^{\frac{1}{2}} \text{ and } l_u = k^{\frac{3}{2}} / \varepsilon \tag{3.4}$$

where, ε is dissipation and C_μ is a model coefficient calibrated to give reasonable agreement over a wide range of flows. Modeled transport equations are solved for the kinetic energy and dissipation. To this day, Boussinesq-based two-equation models continue to be the most popular RANS approach for practical computations due to their robustness, low computational burden and reasonable level of accuracy. Therefore, two-equation model with Boussinesq constitutive closure is a natural candidate for bridging method as well.

Two major proposals are currently under consideration for the adaptation of Boussinesq two-equation model to bridging method. In one approach (Very large eddy simulations – VLES [14]; Limited Numerical Method – LNS [9]; and Flow Simulation Methodology – FSM [8]), the viscosity reduction is attempted by lowering the value of C_μ by a factor which depends on the purported cut-off length scale. In the second method (Partially-averaged Navier-Stokes – PANS [4]; Partially-integrated turbulence method – PITM [15]), it is proposed that the requisite viscosity reduction is best achieved by modifying the transport equations for the unresolved kinetic energy and dissipation rather than changing the Boussinesq model coefficient. Clearly, the numerical resolution must be compatible with the desired viscosity reduction in both cases. In practice, the reduction factor in both methods is specified based on the local grid spacing.

The objective of this paper is to compare the two proposals in two important benchmark test cases: flow past circular cylinder and flow over a backward-facing step. Comparison will be performed in three categories. First, we will examine how well the two models achieve the prescribed level of viscosity reduction. Second, we will compare qualitative features of the computed results from the two methods to verify if the flow characteristics are physically plausible. Finally, we will evaluate the accuracy of the model computations against available data for different levels of viscosity reduction prescription.

In Section 2, we present more details on the proposals to extend the Boussinesq constitutive relations to bridging turbulence models and formulate the basis of comparison. The computational details of the chosen test cases are presented in Section 3. In Section 4, the findings from the simulations are presented and discussed. Section 5 contains summary and discussion.

2. Model Equations and Comparison Criteria

In this section, we will first describe the two-equation Boussinesq-based bridging models and then establish the ground rules and criteria for comparing the two models.

2.1. The bridging models

We seek a closure relationship between the cut-off length and subgrid eddy viscosity. In the two models under consideration, the relation between the grid spacing and subgrid eddy viscosity is modeled in terms of an intermediary parameter called the viscosity reduction factor *R*. The physical significance of *R* is very important. It represents the **desired** reduction in viscosity from a hypothetical RANS calculation of the same flow on the same grid. Any given value of *R* corresponds to a specific cut-off length scale

[10]. Clearly, the smaller the value of *R*, more scales will be resolved resulting is higher degree of accuracy. The minimum value of *R* that can be used in a computation is restricted by the grid spacing [10]. When numerical resolution is very fine, *R* can be small and when resolution is coarse *R* will be closer to unity. Between the two limits, *R* is a smooth function of grid spacing. It is, however, important to note that larger values of *R* is permissible – reflecting the fact that the cut-off length scale can be larger than the grid spacing.

We will begin with the description of the so-called unsteady Reynolds-averaged Navier Stokes (URANS) [7] method which is a forerunner of the bridging methods and then present the bridging models.

2.1.1 URANS method

In this approach, unmodified RANS closure is used to model subgrid-scale (SGS) stress. The calculation is performed in a time-accurate manner on very fine grids with the expectation of capturing unsteady scales of motion that cannot be resolved in steady RANS. Thus, the governing equations are identical to those of RANS and the only difference is in the grid resolution which is finer than in the case of a steady RANS computation. We include this model for the sake of comparison with the bridging methods when appropriate.

2.1.2 PANS/PITM bridging method

In both the partially-averaged Navier-Stokes (PANS) [4] and partially integrated turbulence method (PITM) [15], the turbulent velocity field decomposition is based on the desired level of kinetic energy to be resolved. While PANS model is derived in physical space from RANS equations, the final closure is strikingly similar to the spectral closure development of PITM. In both instances, the Boussinesq constitutive relation itself is left unmodified and the entire onus of rendering the model sensitive to cut-off falls on the velocity and length scale transport equations. The closure models in both cases are derived rigorously from the parent RANS equations and we refer the readers to the original papers for the details. Here we just present the final model equations.

The Boussinesq constitutive relation for partially averaged fields is as given in equation (3.3) and the eddy viscosity is given by:

$$\nu_u = C_\mu \frac{k_u^2}{\varepsilon_u} \qquad (3.5)$$

where, k_u and ε_u are the unresolved kinetic energy and dissipation rate respectively. The reduction in the turbulent eddy viscosity is achieved by modifying the transport equations in a manner consistent with physics to yield lower values of k_u and ε_u such that the ratio of k_u^2/ε_u is smaller than its RANS counterpart. The transport equations for unresolved kinetic energy and dissipation are:

$$\frac{dk_u}{dt} = \mathrm{P}_u - \varepsilon_u + \frac{\partial}{\partial x_j}\left(\left(\frac{\nu_u}{\sigma_{ku}} + \nu\right)\frac{\partial k_u}{\partial x_j}\right) \qquad (3.6)$$

$$\frac{d\varepsilon_u}{dt} = f_k\left(C_{e1}\frac{\mathrm{P}_u\varepsilon_u}{k_u} - C_{e2}^{*}\frac{\varepsilon_u^2}{k_u}\right) + \frac{\partial}{\partial x_j}\left(\left(\frac{\nu_u}{\sigma_{\varepsilon u}} + \nu\right)\frac{\partial \varepsilon_u}{\partial x_j}\right) \qquad (3.7)$$

where, P_u is the PANS production. The PANS model coefficients are: C_{e1} = 1.44; $C_{e2}^{*} \equiv C_{e1} + f_k/f_\varepsilon\left(C_{e2} - C_{e1}\right)$; $\sigma_{ku} \equiv \sigma_k\ f_k^2/f_\varepsilon$ and $\sigma_{\varepsilon u} \equiv \sigma_\varepsilon\ f_k^2/f_\varepsilon$. C_{e2}, σ_k and σ_ε are RANS model parameters and are presented in the next paragraph. In the above equations f_k and f_ε are the PANS viscosity control parameters: $f_k\left(= k_u/k\right)$ is the desired fraction of the turbulent kinetic energy to be resolved and $f_\varepsilon\left(=\varepsilon_u/\varepsilon\right)$ gives the fraction of total dissipation rate to be resolved. The parameters f_k and f_ε control the model cut-off length scale and viscosity. In all the cases presented in this paper f_ε is taken to be unity as the Reynolds number is high enough.

2.1.3 VLES/FSM/LNS methods

As mentioned elsewhere [8, 9, 14], in these methods the reduction in eddy viscosity is effected by reducing the coefficient in the Boussinesq relation by a factor that depends on the desired cut-off length scale:

$$\nu_u = f\ C_\mu \frac{k_u^2}{\varepsilon_u} \tag{3.8}$$

where, f is the desired viscosity reduction factor and in practice is specified according to the local grid resolution. The model transport equations for the VLES, LNS and FSM remain unchanged from the RANS k-ε model equations and are given by:

$$\frac{dk_u}{dt} = \mathrm{P}_u - \varepsilon_u + \frac{\partial}{\partial x_j}\left(\left(\frac{\nu_u}{\sigma_k} + \nu\right)\frac{\partial k_u}{\partial x_j}\right) \tag{3.9}$$

$$\frac{d\varepsilon_u}{dt} = C_{e1}\frac{\mathrm{P}_u\varepsilon_u}{k_u} - C_{e2}\frac{\varepsilon_u^2}{k_u} + \frac{\partial}{\partial x_j}\left(\left(\frac{\nu_u}{\sigma_\varepsilon} + \nu\right)\frac{\partial \varepsilon_u}{\partial x_j}\right) \tag{3.10}$$

where, P_u is the turbulent production. The model parameters are: $C_{e1} = 1.44$; $C_{e2} = 1.92$; $\sigma_k = 1.0$; $\sigma_\varepsilon = 1.3$.

2.1.4 Viscosity reduction factor

As mentioned earlier, the viscosity reduction factor is defined as:

$$R = \frac{\nu_u \ (\text{Bridging model})}{\nu_T \ (\text{RANS})} \tag{3.11}$$

From the models, the desired viscosity reduction factor in PANS and FSM can be easily surmised:

$$R \ (\text{PANS}) = f_k^2 \tag{3.12}$$

$$R \ (\text{LNS, FSM}) = f \tag{3.13}$$

Thus, from the grid size and the relation between grid-size and *R*, the bridging model parameter can be specified for both models.

2.1.5 Important caveat

The closure models are derived from some simplified flow assumptions that may not be entirely valid in practical applications. It is very important to note that while *R* is the desired viscosity reduction factor, it is important to verify *a posteriori* if the desired level of reduction from the RANS calculation is indeed achieved in the computation.

2.2. Model comparison criteria

Our model comparison criteria are based on the examination of the three crucial elements listed in the introduction as keys to bridging model success: predictable viscosity reduction, liberation of more scales of motion and, ultimately, improved model accuracy. Clearly, the accuracy must improve with increase in the number of resolved scales.

2.2.1 Controlled viscosity reduction

First, and foremost, the successful adaptation of the Boussinesq two-equation approach to bridging method requires that the desired level of viscosity reduction be achieved in the calculation. To evaluate if the two proposed models posses this important quality, we propose the following test. We perform separate RANS and bridging computations of specified R (*a priori* viscosity reduction ratio) values on the same numerical grid. In each calculation, we obtain the time-averaged eddy viscosity as a function of space. Then we take the ratio of the RANS and bridging viscosities at each location yielding the computed (*a posteriori*) viscosity ratio. Comparison of the specified (*a priori*) and computed (*a posteriori*) viscosity ratios provides an important basis for evaluating the fidelity of the closure models. If there is a large difference between the specified and calculated eddy-viscosity ratios, then the cut-off and the closure model will be inconsistent with one another leading to unpredictable and unreliable results. Thus, for a reliable bridging calculation, the specified and computed eddy-viscosity ratios must be close.

2.2.2 Liberation of more turbulent scales

Direct computation of more unsteady scales of motion is crucial to the success of bridging methods. Bridging model viscosity reduction is purported to liberate scales of motion that would be suppressed in a RANS calculation. With increasing viscosity reduction, more and more scales of motion should be liberated. We will qualitatively examine the increase in unsteadiness with viscosity reduction.

2.2.3 Comparison with experiments

In the final step of our study, we will compare calculations from each model at different *R* values against experimental and LES data.

While both methods are purported for spatially changing resolution, we will perform the investigation for spatially-invariant specification of viscosity reduction factor due to two important factors. (i) The main reason for the spatially-invariant filter is the minimization of commutation error. When the filter size (related to viscosity reduction factor) varies with time or space in a manner that filtering and differentiation are non-commutative, there will be additional terms in the resolved and unresolved flow evolution equations. These extra terms cannot be modeled resulting in an error termed as the commutation error. (ii) It has been found that grid insensitive results are very difficult to obtain if the viscosity reduction factor is a function of grid spacing.

Therefore, we will restrict ourselves to constant viscosity reduction specification – spatially invariant *R*. For a given flow configuration, all URANS and bridging model calculations (for all *R* values) are performed on the same grid. From detailed sensitivity study, the grid used is shown to be in the grid-insensitive range for all *R* cases. As mentioned elsewhere, larger *R* values can be computed on the same grid as the model cut-off length scale is larger than the grid resolution. Thus, we ensure that any differences in the observed results are due only to the closure model and not grid related issues.

3. Test Case Description

The two benchmark flows chosen for this comparison study are: flow past a circular cylinder at Re_D 1.4×10^5 and flow past a backward facing step at Re_H 3.75×10^4. These flows exhibit large scale unsteadiness and other flow features that are not easily captured with simple RANS models. Simulations are performed for various values of *R* with PANS and FSM to compare the two bridging model proposals.

3.1. Cylinder flow computational details

The domain chosen for the cylinder flow simulations is box-shaped with dimensions as shown in Figure 6. The spanwise width of the cylinder is in accordance with the LES of Breuer [16]. Structured O-type grid is employed with 240 nodes along the wake centerline with the first grid point in the wall normal direction placed at $y^+ \sim 3$. In the circumferential direction, 320 grid nodes are uniformly distributed. The spanwise length of the domain is divided into 32 equal parts. Therefore, the grid has the same resolution as the fine grid cases of Breuer [16] in the circumferential and spanwise direction to accommodate the smallest *R* value case. The resolution along the wake centerline is less fine and the grid nodes are spaced at an expansion ratio of 1.2. At the inlet, zero-turbulence constant velocity field is specified such that the flow Reynolds number based on the cylinder diameter is 1.4×10^5. Outflow boundary conditions are specified at the outlet. The domain boundaries in the crosswise direction are specified as slip walls. Periodic boundary condition is imposed in the spanwise direction. The turbulence model is active at all times during the simulations. The turbulence model parameters are specified depending upon the closure used and the desired viscosity reduction factor *R*.

3.2. Backward facing step computational details

The computational domain used for the backward facing step simulations is shown in Figure 7. The grid resolution in the inlet section is 50×115×36. In the step section, there are 280 nodes along the flow direction. The grid is clustered near the step so that the y+ near the step wall is less than 1. The grid is gradually stretched in this direction with an expansion ratio of 1.05. Along the normal direction, there are 215 nodes with 100 nodes placed within the step height and the first grid point at $y^+ \sim 1$. The spanwise resolution in this section is same as the inlet section with 36 nodes distributed uniformly. At the inlet, a flat plate velocity profile is prescribed. The outlet is modeled as pressure outlet with zero gauge pressure. In the wall-normal direction, no-slip boundary condition is imposed at the bottom wall and slip condition at the top wall. In the z-direction, periodic boundary condition is imposed.

3.3. Flow solver

The simulations were performed using the commercially available Fluent CFD package, which is a finite volume code. For all the simulations, a double-precision solver with second-order upwind discretization for the momentum, turbulent kinetic energy and dissipation equations is used. Third-order MUSCL scheme was also used in select cases. As the difference between the second-order and third-order schemes was small for the quantities investigated in this paper, we present results only from the second-order scheme. It must be, however, pointed out that if unsteady velocity-gradient flow details must be captured accurately, the third-order MUSCL scheme must be employed. Continuity of the incompressible flow was ensured through SIMPLE algorithm. The near-wall regions are treated with enhanced wall treatment. Since the near-wall mesh generated for the test cases is sufficiently fine to resolve the laminar sub-layer, Fluent uses a two-layer zonal model in the wall region [17].

4. Results and Discussion

The test cases chosen in this study are long-standing benchmark flows widely used for validating turbulence models and verifying numerical schemes. The geometry is very simple to set-up but the flow physics exhibits complex features involving separation, large scale coherent structures and reattachment. The inflow and boundary conditions in each case is described in the previous section. To demonstrate the versatility of the bridging methods, k-ε two-equation formulation is used for the cylinder flow and k-ω model is used in the backward-facing step case.

Each simulation is started from a steady-state initial field and allowed to develop unsteadiness. The statistics are gathered after many flow-through times when the statistical stationarity of the flow field in clearly established. The number of flow through times for achieving statistical stationarity is a strong function of *R*. For fine-resolution runs (low *R*), the time taken for stationarity is significantly larger than that of low-resolution (high *R*) cases.

Detailed comparison between PANS results and published experimental and LES data for circular cylinder and backward-facing step cases will be presented in separate papers elsewhere. Here, our objective is to compare the two bridging proposals. Therefore, we will present only the pertinent results here to demonstrate the difference between the two proposals.

4.1. Results from flow past a circular cylinder at Re_D 1.4×10^5

4.1.1 Controlled eddy viscosity reduction

First, RANS calculation is performed to record the eddy viscosity as a function of space. Then, PANS simulations are performed with specified *R* values of 0.6, 0.49, 0.36, 0.25 and 0.16. In the case of FSM, computations are performed with *R* values of 0.8, 0.6, 0.49 and 0.36. Data from the first 30 shedding cycles are discarded to allow for vortex shedding to be established. Once statistically steady vortex shedding is established, flow data from subsequent 50 shedding cycles are gathered to compute the needed statistics. The bridging model eddy-viscosity is then obtained as a function of space. At each location, bridging-model to RANS eddy-viscosity ratio is constructed. Locations in which the background velocity is unaffected or modified by less than 2% of the background flow are not considered as the closure model does not play any role at these grid points. All the other locations constitute the statistical ensemble investigated.

The probability density function (PDF) of the computed PANS viscosity ratio is plotted in Figure 8(a) for each PANS simulation. The specified *R* value is also shown for each case. While there is some spread in the computed ratio distribution, the PDF peaks very close to the specified value in all cases. For reference, uniform distribution of eddy-viscosity ratio will yield a flat PDF at a value of about 1.0. The computed peak PDF value is about 10 clearly indicating the strong propensity of the computed viscosity to be close to the specified value. The eddy-viscosity ratio at over 75% of the flow field is within ±0.05 of the specified ratio in all cases. Closer examination of the flow field reveals that the departure from the specified value is seen mostly in areas where turbulent transport effects are significant. The reader should be reminded that the PANS formulation is based on homogeneous turbulence assumptions and, hence, can be expected to be somewhat inaccurate when transport is the leading cause of turbulence. The PANS (and PITM) paradigm is most valid when the local effects of production and dissipation are most dominant. In Figure 8(b), the most probable *a posteriori* PANS viscosity ratio is plotted as a function of specified (*a priori*) value. Clearly, the computations indicate that PANS/PITM bridging model successfully produce the desired level of viscosity reduction.

The PDF of the various FSM calculations are shown in Figure 9(a) and the specified *R* values are also indicated. It is immediately clear that the computed viscosity ratio values are far from the specified ones in this case. The peaks of the PDF are located far from the specified values. In Figure 9(b) we plot the most probable *a posteriori* viscosity ratio against the *a priori* one. The difference between the specified and computed ratio gets progressively worse with decreasing *R* value. In fact for the $R = 0.36$ case, the PDF is not too far from an uniform distribution implying very little correlation between specified and computed viscosity ratios.

To understand the reasons for the big difference between the two methods, we now plot the unresolved kinetic energy computed from the two approaches. In Figure 10(a), the PDF of the ratio of PANS to RANS unresolved kinetic energy is plotted for the various *R* calculations. A similar plot for FSM is shown in Figure 10(b). The fundamental difference between the two models is immediately evident. In the case of PANS, the level unresolved kinetic energy goes down progressively with *R* as specified. The PDF peaks fairly close to the specified value of $f_k = \sqrt{R}$. Lower levels of unresolved kinetic energy lead to reduced eddy viscosity. In the case of FSM, there is no discernible decrease in unresolved kinetic energy as a function of *R*. Rather surprisingly, there is a high probability of the FSM unresolved kinetic energy exceeding that of RANS kinetic energy with decreasing *R*, as indicated by the long and heavy tails of the PDF. Thus, the FSM kinetic energy behavior appears to be contrary to expectations.

4.1.2 Liberation of unsteady scales

The performance of the bridging models in resolving the turbulent flow structures is presented next. Figure 11, Figure 12, and Figure 13 show the instantaneous contour plots obtained from the two bridging methods studied for the case of $R = 0.16$. Although the results presented here are qualitative in nature, they help to identify important features of the two bridging proposals. Figure 11(a) and Figure 11(b) show the instantaneous x-vorticity contours obtained from the PANS and FSM respectively. The difference between the two results is striking. In the case of PANS (Figure 11(a)), the results goes from laminar two-dimensional flow over the cylinder to highly unsteady, strongly three-dimensional flow with energetic small scales in the wake Many of the flow details (striated rollers in the wake region) are qualitatively consistent with experimental observations. The FSM results (Figure 11(b)) on the other hand yield a two-dimensional flow pattern throughout the entire flow domain. In Figure 12(a) and Figure 12(b), the z-vorticity contours are compared. While FSM flow field exhibits regular laminar-like vorticity pattern, the PANS contours are irregular composed of a wider range of scales characteristic of turbulence. The reasons for the observed PANS and FSM behavior can be surmised from the instantaneous contour plots of turbulent eddy viscosity shown in Figure 13(a) and Figure 13(b). The contour color coding used in both cases is identical: the level of viscosity increases from blue to green to yellow to red. The PANS eddy viscosity levels are significantly lower that the FSM values as quantified in Figure 8(a) and Figure 8(b). Therefore, in FSM much of the small-scale motions, including all relatively weak three-dimensional structures, are suppressed leading to a laminar-type regular two-dimensional flow field. As $R = 0.16$ is the finest resolution examined, it can be expected that the FSM calculations of higher R values will be laminar-like and two-dimensional, a fact that is confirmed in our calculations (results not shown).

4.1.3 Comparison against data

We now compare PANS and FSM results against experimental data (Cantwell and Coles [18]) and LES computations (Breuer [16]). As mentioned earlier, a detailed comparison between PANS and published data will be performed elsewhere. Here, the focus is on comparing the accuracy of PANS and FSM.

Figure 14(a) shows the mean streamwise velocity along the wake centerline for the various PANS simulations. Experimental data [18], LES results [16] and URANS calculation are also shown for comparison. It is useful to note that URANS corresponds to $R = 1$ case. It is easy to see that as R decreases, the PANS results goes monotonically from the URANS to LES results. The circulation bubble size is well predicted by $R = 0.36$ case. The out-flow recovery is not very well predicted and probably can be improved by introducing a longer buffer zone between the fully-developed outflow condition and the flow region of interest. Notwithstanding that, it is very clear that the PANS model performance improves substantially with decreasing R: at $R = 0.36$ good agreement with data is obtained. For a given increment in R, the difference in PANS result is larger at large R values and very small at lower R values. For smaller R values, the mean velocity plot is only slightly different from the $R = 0.36$ case.

Figure 14(b) presents similar comparison of FSM calculations. Again, URANS case corresponds to $R = 1$ calculation. While the FSM accuracy certainly improves with decreasing R, the rate of improvement is much slower than PANS. For a given value of R, the FSM results are much inferior to the PANS computations. For a given R, due to higher FSM eddy-viscosity levels, there is less mixing in the wake leading to larger recirculation bubble size that what is seen in PANS results and LES data. The change from $R = 0.49$ case to $R = 0.36$ case is more substantial in PANS than in FSM. For values of $R < 0.36$, the FSM results do not show much improvement over the $R = 0.36$ case shown in the figure. The reason for this can perhaps be found in Figure 4 where the computed values of eddy viscosity are shown. It is very clear that the computed FSM eddy viscosity responds very slowly to decreasing R in the fine resolution range.

In Figure 15, the mean streamwise velocity statistics at two different x-planes in the near-wake region is presented. At $x/D = 1.0$, the bridging models predict a V-shaped velocity profile whereas the experiments and LES predict a U-shaped velocity profile. At the centre, the PANS model predictions are closer to the experimental observations than URANS and FSM. At $x/D = 3.0$, the URANS results predict the mean velocity defect to be higher than in experimental data. The PANS and FSM data agrees fairy well with experiments at this location.

4.2. *Results from backward facing step at* Re_H 3.75×10^4

The simulation of flow past a backward facing step is a challenging test case as it involves predicting the boundary layer accurately. The backward facing step simulations were performed using the k-ω turbulence model [19]. The PANS k-ω model has the advantage of predicting the turbulent boundary layer at solid walls without having to apply any viscous correction to reproduce the law of the wall [20].

4.2.1 Controlled eddy-viscosity reduction

For this test case, the results of eddy-viscosity reduction factor are presented only for the PANS case. Figure 16 shows the distribution of the computed viscosity factor from various PANS simulations along with the prescribed value. The peak of the computed ratio agrees very precisely with the specified value. Although the spread in the PDF is a little larger than in the cylinder case, it is clear that the eddy-viscosity reduction over a substantial portion of the flow field is close to the specified value. Much of the deviation from the prescribed value occurs close to the walls underscoring the need for better wall treatment. Accurate wall treatment at reasonable cost continues to be a major topic of research interest in LES and hybrid methods. We will address this issue in later works. Overall, this figure clearly validates the PANS/PITM eddy-viscosity reduction rationale.

4.2.2 Liberation of unsteady scales

The vorticity contours from PANS and FSM calculations ($R = 0.25$) are shown in Figure 17(a) and Figure 17(b) respectively. The shown PANS result is at an arbitrary time after statistical steady state is established. The PANS calculation again exhibits irregular three-dimensional flow structure with motions over a wide range of scales typical of turbulent flows. The shown PANS profile is used as the initial condition for the FSM calculation. Thus the FSM initial field is three-dimensional with energetic small scales. During the course of the FSM evolution it is found that the small scales and three-dimensional structures quickly disappear leading to laminar-type two-dimensional flow field. The predicted FSM flow pattern is similar to RANS results.

4.2.3 Comparison against data

Figure 18(a) and Figure 18(b) compare the mean velocity statistics obtained from the PANS and FSM model computations for $R = 0.25$. Figure 18(a) presents the results for the mean velocity statistics at $x/h = 1.0$ and Figure 18(b) shows the same statistics at several planes further downstream of the step region. The symbols in the plots represent measured data of Driver and Seegmiller [21] Recall (from Figure 17) that the flow fields that yield the PANS and FSM results are fundamentally different. At $x/h = 1.0$, the PANS model captures the trend for the mean streamwise velocity quite adequately. The FSM model predicts a shallow velocity profile in comparison to experimental data. At $x/h = 5.0$, the FSM computations do not capture the reverse flow characteristics of the flow since the model under-predicts the reattachment length. The PANS model captures the trend and the predicted value for the reattachment length is in agreement with experimental data. At x-planes further downstream, the FSM model always over-predicts the mean streamwise velocity inside the step region.

As mentioned earlier, a detailed comparison between PANS and experimental data will be presented elsewhere. The results presented here is merely for the purpose of comparing PANS bridging paradigm to the FSM approach.

5. Conclusion

The main objective of the present study is to evaluate the effectiveness of two bridging approaches: PANS and PITM on one side and VLES, FSM and LNS on the other. Each approach employs a Boussinesq constitutive relation and solves transport equations for length and velocity scales. The rationale for achieving viscosity reduction (over the base RANS model) is, however, fundamentally different. In the case of VLES, FSM and LNS it is proposed that the viscosity reduction can be achieved by lowering the value of the model co-efficient in the Boussinesq relationship. The FSM length and velocity scale equations are unaltered from the RANS form. On the contrary, in the PANS/PITM paradigm, the reduction of viscosity is attempted by modifying coefficients in the transport equations for length and velocity scales. The coefficient in the PANS Boussinesq relation is not modified.

For this evaluation, reasonably high Reynolds number simulations of flow past a circular cylinder and flow past a backward facing step are chosen as test cases as they are simple to set-up and experimental and other numerical data are readily available. Simulations using both the PANS and the FSM bridging models are performed for different viscosity reduction factors.

From our study, we conclude that PANS closure yields to a reliable and predictable reduction in subgrid viscosity. The reduction in viscosity leads to the liberation of scales of motion that are typically suppressed in a RANS calculation. Due to the direct computation of more scales of motion, PANS accuracy increases substantially with decreasing viscosity reduction factor. Overall, PANS appears to be a reasonable bridging model that performs as intended.

On the other hand, the FSM closure does not lead to the specified level of viscosity reduction. More importantly, there is clear evidence that unsteady scales of motion are not present in the calculations although the grid spacing is fine enough to resolve these scales of motion. Although some improvement is observed in the comparison against experimental data, this clearly is not due to the direct computation of more scales of motion.

The PANS and FSM observations are well in line with the fixed-point analysis of Girimaji et al. [11]. It is demonstrated in that paper that modifying the transport equations for the length and velocity scales offer the best approach to resolving more scales of motion. It is also argued that modifying the C_μ value alone is tantamount to a different choice of RANS model.

CHAPTER IV

CHARACTERIZATION OF SPATIAL AND TEMPORAL FLUCTUATIONS IN VARIABLE RESOLUTION PANS COMPUTATIONS

1. Introduction

Variable resolution (VR) models are envisioned because of the desire to compute the physics of turbulent flows as accurately as possible by utilizing the available computational resources efficiently. In a given flow, there are regions where the flow is very complex and needs a higher resolution to capture the turbulence physics accurately and other regions where turbulence is statistically stationary and Reynolds averaged Navier-Stokes (RANS) methods are sufficient to capture the flow physics accurately. Having a high resolution throughout the domain is not only computationally not viable but also unnecessary. VR models are capable of performing high resolution simulations in complex flow regions and RANS in the rest of the domain.

The premise of VR models is to alleviate the grid resolution requirements from an analogous LES computation by modeling a larger portion of the energy spectrum than LES. The spatial cut-off for VR methods is typically placed in the inertial range of the turbulent energy spectrum making $\nu_{LES} < \nu_{VR}$. Therefore, the grid resolution requirements for VR methods are not as stringent as in LES. VR models in the recent past have been subjected to a number of different classifications. Sagaut et al. [22] classify the VR models as global methods and zonal methods. Frölich and Von Terzi [23] classify VR models into segregated, unified and second generation unsteady RANS. Here we introduce a new classification. We classify VR models into *grid based methods* and *viscosity prescribed methods* based on the criterion in which they achieve hybridization.

1.1. Grid based methods

In grid-based methods, the mesh width determines the physical resolution of the simulated flow. In other words, the numerical resolution and the physical resolution of the flow are intimately inter-related. Detached eddy simulations (DES) [6] which is zonal hybrid RANS/LES model belongs to this category of VR models. The modeled viscosity ν_{VR} in grid-based methods varies with the local strain rate and the grid spacing:

$$\nu_{VR} \propto |S|\Delta^2 \tag{4.1}$$

In grid-based methods the grid spacing Δ completely characterizes the unresolved flow field and the only information we have of the unresolved field is the modeled viscosity ν_{VR}.

1.2. Viscosity based methods

In viscosity based methods, the level of unresolved viscosity is prescribed and the grid-size is chosen to accommodate the value of viscosity. By prescribing viscosity level at a fraction of RANS eddy viscosity value, more scales of motion are liberated. Some of the examples of viscosity-prescribed VR model include partially averaged Navier-Stokes (PANS) [4], partially-integrated transport model (PITM) [15] and flow simulation methodology (FSM) [8]. For a given modeled eddy viscosity, the grid resolution requirements can be estimated from turbulent scaling laws [10] as:

$$\Delta x \leq \sqrt{\frac{\nu_{VR}}{|S|}} \tag{4.2}$$

In viscosity-prescribed methods, the available information about the modeled flow field include statistics of the modeled viscosity herein we refer to as unresolved eddy viscosity v_u, unresolved kinetic energy k_u, and unresolved dissipation rate ε_u. Choosing a grid finer than that prescribed by equation (4.2) would only lead to increased numerical accuracy rather than increased scale resolution.

The flow field simulated by VR models as a result of scale separation is neither a statistically averaged flow field as in Reynolds averaged Navier-Stokes (RANS) nor a conventionally filtered field as in large eddy simulations (LES). Therefore, the theoretical background developed to present the existing methodologies is unsuitable for VR models. We need to put forth a new framework to analyze the performance of VR methods which is the aim of this study. Issues to be addressed include:

a) <u>Consistency of the filtering operation:</u> Many of the VR models do not have an explicit scale separation operation. The closure model takes care of the scale separation operation and account for unresolved scales. The closure model is scaled to provide a predetermined resolution. Addressing whether the predetermined resolution is achieved in the computation is an important aspect towards VR model validation. Chapter III deals with this investigating this issue for various VR models including PANS and as observed, in PANS, the closure model does achieve the predetermined resolution in its computations.

b) <u>Characterizing VR model fluctuations:</u> Many of the proposed VR model produce fluctuations that might not be physical or cannot be characterized as turbulence. We need a new methodology to characterize the fluctuation obtained from VR models to see whether they adhere to turbulence theory and current work address this issue.

c) <u>Commutation errors:</u> Many VR models do not address the errors associated with neglecting the terms associated with rate of change of filter-width in the filtered Navier Stokes equations. In the current study involving PANS, we have a constant filter-width minimizing the commutation errors.

While the objective of the RANS model is to accurately reproduce kinetic energy (k) and dissipation (ε) – alternatively specific dissipation (ω) – the VR models must satisfy a broader set of requirements. A good VR method must not only lead to accurate k and ε, it must also yield physically meaningful spatial and temporal fluctuations that represent the true character of turbulence. In this aspect, VR models have a lot in common with LES. In the context of LES, Muschinski [24] developed the concept of 'LES fluids' which are hypothetical non-Newtonian fluids with viscosity ν_{LES} greatly varying both temporally and spatially. It was argued that the non-Newtonian fluid must still abide by Kolmogorov's similarity hypothesis as the viscosity value does not affect large and intermediate scale dynamics. Kolmogorov's similarity theory is used as an effective method to characterize the fluctuations in the analysis of Muschinski [24]. Our goal is to develop a rationale approach along the lines of Muschinski to understand the spatial and temporal fluctuations in VR methods.

The objective of this paper is to characterize the spatio-temporal fluctuations of viscosity-prescribed VR models – focusing on PANS – to address (i) Whether these fluctuations follow Kolmogorov-type scaling laws. Such a demonstration will level credibility to VR model calculations. In Section 2, we formulate the length and time scales which would enable proper characterization of the PANS unresolved scales. Section 3 is the crux of this paper where we compute the distribution of the length and time scales and derive the VR analogue to Kolmogorov's scaling arguments. Section 4 concludes this work by summarizing the important observations.

2. Characteristic Turbulent Scales for VR Models

PANS, the VR model of interest in this study develops higher-resolution closures from the traditional RANS turbulence models by rescaling the transport equations in a formal manner to reduce the modeled eddy viscosity [4, 10, 11]. The rescaling parameters in PANS specify the fraction of total turbulent kinetic energy to be resolved (f_k) and the fraction of the total dissipation rate to be resolved (f_ε). For high Reynolds number flows the inertial range of the turbulent energy spectrum is well defined and hence $f_\varepsilon = 1.0$. In order to recover RANS or DNS limits, all that need to be varied is the f_k parameter. $f_k = 0$ corresponds to DNS limit and $f_k = 1.0$ corresponds to RANS limit. f_ε controls the Reynolds number effects. We prescribe the amount of reduction in the modeled viscosity to be achieved by the PANS model equations in comparison to the RANS eddy viscosity by prescribing f_k and f_ε. Since the closure for the sub-filter stresses (SFS) is provided using a RANS two-equation model, the characteristic length and time scales in PANS model are functions of ν_u, k_u, and ε_u. In this study we construct functional length scales – quantities with dimension of length derived from single point statistics of flow variables [25] – and time scales which are relevant to VR models.

2.1. Computational Kolmogorov length and time scales

In turbulence, the physical Kolmogorov length scale η given by equation (4.3) characterize the very smallest dissipative eddies. For a DNS calculation, eddies of the size of Kolmogorov length scale need to be resolved. Therefore η provides the guidelines for prescribing the grid-spacing (Δ) in a DNS calculation.

$$\Delta_{DNS} \approx \eta \sim \left(\frac{\nu^3}{\varepsilon} \right)^{1/4} \tag{4.3}$$

In viscosity prescribed VR methods, the smallest resolved eddy is dependent on the magnitude of eddy viscosity to be modeled. Knowing the modeled viscosity and extending the DNS scaling arguments to VR models, we define the computational Kolmogorov scale η_c, the VR model equivalent for the Navier-Stokes fluid dissipation length scale η, as the smallest length to be resolved in VR method. Scales smaller than η_c are dissipated by viscous action. The relation between ν_u and η_c, following dimensional reasoning, is given by:

$$\Delta_{PANS} \approx \eta_c\left(x\right) = \left(\frac{\nu_u^3}{\varepsilon_u}\right)^{1/4} \tag{4.4}$$

As in DNS, η_c provides the guidelines for fixing the grid resolution in VR model computation. The mesh-width Δ must be smaller than η_c for a trustworthy simulation.

The corresponding time scale associated with η_c is the computational Kolmogorov time scale of turbulence. It is a function of the modeled viscosity ν_u and modeled dissipation rate ε_u. From dimensional reasoning, we get:

$$\tau_g = \left(\frac{\nu_u}{\varepsilon_u}\right)^{1/2} \tag{4.5}$$

2.2. *Local viscous length and time scales*

While Kolmogorov length scale is the smallest in a simulation, the prevailing local length scale at any given location can be larger. We derive the local viscous length scale λ_u from the current resolved strain rate S_r and ν_u which are prominent parameters in a VR model computation. From dimensional reasoning the equation for the local viscous length scale which is a function of space and time is given by:

$$\lambda_u(x,t) = \left(\frac{\nu_u(x,t)}{S_r(x,t)} \right)^{1/2} \tag{4.6}$$

where, $S_r = \left[1/2 \left(\partial U_i / \partial x_j + \partial U_j / \partial x_i \right)^2 \right]^{1/2}$, U_i is the instantaneous velocity field obtained from the VR model simulation.

The dynamics of the PANS governing equations allow for time-scales to be associated with the above defined length scales. The corresponding local time-scale defined in this study is given by:

$$\tau_l = \frac{1}{S_r\left(x,t\right)} \tag{4.7}$$

The length and time scales defined above will enable us to identify the different aspects of turbulence structures present and thereby helps in understanding the performance of the turbulence model.

Analysis of the characteristic length and time scales of the unresolved turbulent field also facilitates in evaluating the computational cost associated with a VR model calculation. The computational cost for a VR model depends on the portion of the turbulence spectrum to be resolved. The increase in cost from a corresponding RANS computation can be estimated based on the desired reduction in modeled viscosity. The larger the ratio of ν_{RANS}/ν_u the higher the computational cost. Similarly, we can also estimate the reduction in effort from a corresponding DNS computation. The reduction in effort for a VR model computation compared to a DNS of the same flow is ~ $\left(\eta_c/\eta\right)^3$

3. Characterizing PANS Flow Field

In this section, using the previously defined characteristic length and time-scales, we will show that the PANS fluctuations (i) scale in a self similar manner for different cut-off wavenumbers; (ii) self similar scaling is similar to DNS scaling and (iii) the scaling follows standard turbulence scaling arguments.

We perform the PANS model analysis by simulating two complex flow configurations. These test cases are feature rich and exhibit a wide range of length and time scales. The first test case is flow past a circular cylinder and the second is the backward facing step flow. The parameters of the cylinder flow simulations correspond to the experimental study of Cantwell and Coles [18]. The Reynolds number of the flow based on the cylinder diameter is 1.4×10^5. The backward facing step (BFS) simulations are based on the experimental study of Driver and Seegmiller [21]. The Reynolds number based on the step height is 37,500. The calculations are performed using non-uniform grids and the computational details are presented in Lakshmipathy and Girimaji [26]. In the present paper, the results are restricted to presenting the characteristic length and time scales predicted by PANS model. A detailed analysis of the flow and turbulent statistics predicted by the model and its performance with respect to other turbulence models is presented elsewhere.

The computed PANS flow field need not necessarily correspond to the level of representation of the physical system as indicated by the imposed theoretical filter. The question of interest is whether the specified filter which in the case of PANS is specifying the amount of viscosity reduction to be achieved from the parent RANS model is reflected in the computed flow field. A study performed to address this issue for PANS is presented in Lakshmipathy and Girimaji [26]. It is shown that the computed PANS flow field is a correct representation of the implied theoretical filter.

In the following paragraphs we present the results from the length and time scale analysis of the PANS model. The PANS model computations are performed for various filter-widths (f_k) for both the test cases considered. From these computations we calculate the length and time scales of interest which are functions of space and are statistically averaged. The length and time scale distribution in the domain are presented as probability density function (PDF) plots.

Figure 19a and Figure 19b present the PDF of the ratio of local viscous length scale to the computational Kolmogorov scale $\left(\lambda_u/\eta_c\right)$ for the cylinder flow case and the BFS case respectively. The PDFs for the cylinder flow simulations imply that the scaling is self-similar and independent of the filter-width. Singh and Mittal [27] identified that the structure of turbulence for the cylinder flow test case resembles that of isotropic homogeneous turbulence. For the BFS case, we plot the length scale ratio obtained from a DNS study of decaying isotropic turbulence from Lee et al. [28] along with the PANS data for this ratio in Figure 19b. The self-similarity of the PANS results and its universal behavior in comparison to the DNS data implies that the structure of turbulence for these cases is identical. The comparison of the DNS and PANS results in Figure 19b confirm that the characteristic length scales scale in a self-similar manner for different filter-widths and this scaling is similar to DNS scaling. The most probable value for this ratio is close to unity implying that $\lambda_u \sim \eta_c$.

In Figure 20a and Figure 20b, the PDFs of the ratio of local viscous length scale of PANS to the Taylor length scale of RANS is plotted for the cylinder flow case and the BFS case respectively. The Taylor length scale is a functional length scale that determines the straining of small scales of turbulence in RANS and is given by:

$$\lambda = \frac{k^{3/2}}{\varepsilon} \tag{4.8}$$

One of the criteria for successful modeling using PANS is that local viscous length scales defined by equation (4.6) should be smaller than the RANS Taylor length scales and the computational Kolmogorov scales should be the smallest resolved length scales i.e. $\lambda > \lambda_u(x,t) \geq \eta_c$. From these figures we observe that for both the test cases simulated $\lambda_u < \lambda$ throughout the computational domain. The most probable value for this ratio decreases as we place the cut-off further towards the dissipation scales indicating that the model is performing as intended i.e. more scales of motion are being resolved than being modeled. The DNS limit in these plots is obtained by replacing the turbulent viscosity in the local viscous length scale by molecular viscosity. The RANS limit is at one. The PANS results are between the RANS and DNS limits and reducing the f_k value shifts the PANS PDF towards the DNS limit demonstrating the seamless bridging capability of PANS.

We plot the PDF of the ratio of smallest length scale to the RANS Taylor length scale - η_c/λ in Figure 21a and Figure 21b for the cylinder flow case and the BFS case respectively. The DNS limit which is obtained by using the molecular viscosity to calculate the Kolmogorov scales and the RANS limit for this ratio are plotted alongside for analysis purposes. The PANS results show that the PDF distribution of this length scale ratio lies entirely between the DNS and RANS limits. As we decrease the f_k value, we are reducing the induced viscous damping thereby more of the smaller scales are being liberated to be resolved by a computational grid that can sustain these high frequency scales of motion and hence the shift in the PDF values towards DNS limit. f_k, the resolution control parameter in PANS does perform as a bridging parameter between DNS and RANS limits.

Another indication of the PANS model performance as a seamless bridging model can be observed in Figure 22a and Figure 22b for the cylinder flow and the BFS respectively. In these figures we compare the ratio of the smallest length scale in PANS to the corresponding RANS length scale. The PDFs are presented for different f_k values.

The RANS length scales are computed from the RANS viscosity and dissipation rate. The DNS data is computed from molecular viscosity and from RANS dissipation rate. The DNS and the RANS limits form the bounds for the PDF plots. From these length scale ratios we observe that as we decrease the f_k value, the computational Kolmogorov scale does become smaller indicating that we are resolving more scales of motion and hence tending towards the DNS limit. These PDF plots also indicate the soundness of the PANS computations performed. The model performs as intended and the grid on which the simulations are performed does support the lowest value of viscosity prescribed in this study.

We plot the time-scales associated with η_c and λ_u which are τ_g and τ_l respectively. Figure 23a and Figure 23b present the PDFs of time scale ratio τ_l/τ_g for the cylinder flow and BFS test cases respectively. These figures again show self-similarity for various f_k values simulated for both the test cases. DNS data of Lee et al. [28] is plotted alongside the PANS results for the BFS. The self-similar scaling of PANS for various filter-widths and its similarity to DNS scaling is clearly indicated in Figure 23b.

4. Discussion and Conclusion

The purpose of PANS model is to provide closure for the unresolved scales at any physical resolution ranging from RANS to DNS. The filtered PANS governing equations can be considered as the equation of motion for a non-Newtonian fluid, the viscosity for which is higher than the material viscosity and is varying both spatially and temporally. The main goal of this study was to establish a method to characterize the modeled flow field thereby providing credibility to the PANS method as a bridging model that performs as intended.

The length and time scale analysis presented in section 3 indicate that the constructed length and time scales from filtered flow field follow turbulence scaling rules. The PDFs for various length scales consistently show a self-similar behavior of the model for various f_k values. Comparing the PANS behavior with a DNS, the unresolved flow field which is modeled using rescaled RANS model permits a Kolmogorov type analysis of the PANS model. The computational Kolmogorov length scale which was defined by extending the Kolmogorov scaling arguments for PANS method is indeed the smallest resolved length scale found in the computed flow field. The PDFs of the length scale ratios for various f_k values reflect our hypothesis that the modeled flow field can be subjected to turbulence theory arguments.

CHAPTER V

PANS k_u-ω_u MODEL: FORMULATION AND VALIDATION

1. Introduction

The Reynolds averaged Navier-Stokes (RANS) k-ω turbulence model is the second most popular model for industrial applications after the RANS k-ε model [29]. The model was first proposed by Kolmogorov [30] and ever since has been subjected to several different formulations. Kolmogorov's k-ω model lacked a production term in the equation for ω restricting its applicability. Also the model lacked a molecular diffusion term making the model strictly applicable to high Reynolds number flows and unable to be integrated through the viscous sub-layer. Wilcox [31] proposed the k-ω model with the production term included and re-established the closure coefficients. The primary advantage of k-ω formulation compared to k-ε is that the former can be integrated through the viscous-sub layer. The model equations allow for Dirichlet boundary conditions to be specified at the wall thereby making the model numerically more stable. The model does not require explicit wall-damping functions compared to the k-ε model as the specific dissipation rate, ω is large in the wall region. In the logarithmic region, the model gives good agreement with experimental results for adverse pressure gradient flows due to the lack of a cross diffusion term in the ω equation [32]. The model predicts the turbulent kinetic energy behavior close to the solid boundary with good accuracy and even describes the boundary-layer transition reasonably well. However, the lack of a cross diffusion term causes the model to be sensitive to small free-stream values of ω, adversely affecting the performance of the model in free shear flows. Even though, the sensitivity of the model is reduced for complex flows [32], the presence of small free-stream ω in the wake imparts ambiguity in the predicted results. Wilcox's revised k-ω model [19] improves the model prediction capability in self-similar free-shear flows without degrading the model's accuracy for boundary layer flows. This has been achieved by making the closure coefficients, which were previously constants, as a function of flow variables.

Over the last decade much of the focus in practical turbulence modeling has shifted from RANS to variable resolution (VR) methods [1]. VR methods provides for rational utilization of computational resources. The dominant energy containing turbulent structures which are geometry dependent are resolved by the grid whereas the passive universal structures are modeled using closure models. Partially averaged Navier-Stokes (PANS) method of Girimaji [4] – the VR model considered in this study – is among several other VR models [1] currently under development for engineering applications.

The theory of PANS modeling is based on combining the advantages of RANS with that of large eddy simulations (LES) [4]. PANS is designed to provide closure for unresolved scales of any level of cut-off resolution. The filter-width in PANS can be seamlessly varied between RANS limit and DNS limit. Closure model for the unresolved flow field in PANS is derived systematically from a parent RANS model. Preliminary analysis of the PANS model using RANS k-ε model as the closure model has provided promising results [10-12]. PANS model does accomplish its primary objective to perform variable resolution simulations. In the present paper, we extend the PANS model to k-ω formulation. PANS k-ω model would inherit the features of the parent RANS model thereby making the model numerically more robust and able to be integrated all way to the solid wall. Since the closure model is used only to capture a fraction of the turbulent energy spectrum, while the rest of the scales are resolved by the computational grid, some of the shortcomings of the model such as its sensitivity to freestream values of ω are suppressed.

In PANS k_u-ω_u model, the filter width is controlled by two parameters f_k – ratio of unresolved-to-total kinetic energy and f_ω – ratio of unresolved-to-total specific dissipation rate while the corresponding resolution control parameters for the PANS k-ε model are f_k and f_ε – ratio of unresolved-to-total dissipation rate [4]. Since ω is defined as dissipation rate per unit kinetic energy, the relation between f_ω and f_ε is $f_\omega = f_k/f_\varepsilon$. Each

f_k corresponds to a different cut-off filter in the energy spectrum. A zero value for f_k corresponds to a DNS type simulation where in the filter width is of the order of the Kolmogorov scales and $f_k = 1.0$ corresponds to a RANS type simulation with the filter-width of the order of the largest scales. In a PANS calculation f_k can take any value between zero and unity provided appropriate grid resolution is available. The value of f_ω depends on the flow Reynolds number. By specifying f_k and f_ω, the model can be tailored for any degree of physical resolution between RANS and DNS. However, the grid resolution must be adequate to capture the fluctuations liberated by the model. The relation between grid resolution and f_ε/f_ω will be derived later.

Our main objective in the present study is twofold. First, we derive the PANS k_u-ω_u formulation. Second, we validate the model by comparing it with PANS k_u-ε_u and other data available in literature. We will compare the performance of the PANS k_u-ε_u model and PANS k_u-ω_u model for two flow fields: flow past a circular cylinder at $Re_D = 1.4\times10^5$ and flow past a backward facing step at $Re_H = 3.75\times10^4$. These flow fields are ideal test cases to validate the performance of a turbulence model. Flow past a circular cylinder involves separation which is not induced by a geometric singularity and shear layer interaction in the wake region; In the case of flow past a backward facing step, the separation point is know *a priori*. The reversing vertical flow and reattachment zone provide well defined conditions and adequate flow complexities.

The organization of this paper is as follows, Section 2 presents the derivation of the PANS k-ω model. In Section 3, we present the results from the PANS k-ε and PANS k-ω simulations. Comparison of the results with available experimental and other numerical results is shown. We conclude with a discussion and summary in Section 4.

2. PANS k_u-ω_u Model Derivation

The PANS k-ω model derivation follows the same rationale as the PANS k_u-ε_u model [4]. To develop the PANS k-ω model equations, we start by deriving the filtered Navier-Stokes equations. The instantaneous Navier-Stokes equations are given by:

$$\frac{\partial V_i}{\partial t} + V_j \frac{\partial V_i}{\partial x_j} = -\frac{\partial p}{\partial x_i} + \nu \frac{\partial^2 V_i}{\partial x_j \partial x_j} \tag{5.1}$$

$$\frac{\partial^2 p}{\partial x_i \partial x_i} = -\frac{\partial V_i}{\partial x_j}\frac{\partial V_j}{\partial x_i} \tag{5.2}$$

The instantaneous velocity field, V_i is partitioned into resolved and unresolved parts using an arbitrary homogeneous filter which is constant preserving and commutes with spatial and temporal differentiation.

$$V_i = U_i + u_i \tag{5.3}$$

U_i is the resolved velocity field and u_i is the unresolved field. The filtering operation is denoted by the symbol $\langle\ \rangle$:

$$\begin{aligned} U_i &= \langle V_i \rangle \\ \langle u_i \rangle &\neq 0 \end{aligned} \tag{5.4}$$

Performing the filtering operation on the instantaneous Navier-Stokes equation (5.1) and Poisson equation (5.2) and, we obtain the governing equations for the resolved velocity field U_i:

$$\frac{\partial U_i}{\partial t} + U_j \frac{\partial U_i}{\partial x_j} + \frac{\partial \tau\left(V_i, V_j\right)}{\partial x_j} = -\frac{\partial \langle p \rangle}{\partial x_i} + \nu \frac{\partial^2 U_i}{\partial x_j \partial x_j} \tag{5.5}$$

$$-\frac{\partial^2 \langle p \rangle}{\partial x_i \partial x_i} = \frac{\partial U_i}{\partial x_j} \frac{\partial U_j}{\partial x_i} + \frac{\partial \tau\left(V_i, V_j\right)}{\partial x_i \partial x_j} \tag{5.6}$$

The filtering operation brings out an additional non-linear term $\tau(V_i, V_j)$ which is the generalized central second moment defined as [33]:

$$\tau\left(V_i, V_j\right) = \left(\left\langle V_i V_j \right\rangle - \left\langle V_i \right\rangle \left\langle V_j \right\rangle\right) \tag{5.7}$$

The closure problem arises due to the generalized central second moment also referred to as sub-filter stress (SFS) term, $\tau(V_i, V_j)$ in the PANS equations. The evolution equation for the SFS term is similar in form to its RANS counterpart and is given by [33]

$$\frac{\partial \tau\left(V_i, V_j\right)}{\partial t} + U_k \frac{\partial \tau\left(V_i, V_j\right)}{\partial x_k} = \mathrm{P}_{ij} + \Phi_{ij} - D_{ij} + T_{ij} \tag{5.8}$$

In the above equation, the various terms on the left-hand side (LHS) are production (P_{ij}), pressure-correlation (Φ_{ij}), Dissipation (D_{ij}) and transport (T_{ij}) of SFS stress.

$$\mathrm{P}_{ij} = -\tau\left(V_i, V_k\right) \frac{\partial U_j}{\partial x_k} - \tau\left(V_j, V_k\right) \frac{\partial U_i}{\partial x_k}; \tag{5.9}$$

$$\Phi_{ij} = 2\tau\left(p, S_{ij}\right); \quad S_{ij} = \frac{1}{2}\left(\frac{\partial \left\langle V_i \right\rangle}{\partial x_j} \frac{\partial \left\langle V_j \right\rangle}{\partial x_i} \right); \tag{5.10}$$

$$D_{ij} = 2\nu\tau\left(\frac{\partial V_i}{\partial x_k}, \frac{\partial V_j}{\partial x_k}\right); \tag{5.11}$$

$$T_{ij} = -\frac{\partial}{\partial x_k}\left(\tau\left(V_i, V_j, V_k\right) + \tau\left(p, V_i\right)\delta_{jk} + \tau\left(p, V_j\right)\delta_{ik} - \nu\frac{\partial\left[\tau\left(V_i, V_j\right)\right]}{\partial x_k}\right) \tag{5.12}$$

In the above equations, p' is the pressure field corresponding to the unresolved fluctuations.

$$\nabla^2 p' = -2\frac{\partial U_i}{\partial x_j}\frac{\partial u_j}{\partial x_i} - \frac{\partial u_i}{\partial x_j}\frac{\partial u_j}{\partial x_i} \tag{5.13}$$

Equations (5.8) – (5.13) are invariant to the type of filter and consequently, invoking Germano's averaging invariance property [33], the SFS term must be invariant to the type of averaging, provided the generalized central moments are used. Based on these arguments, PANS is capable of inheriting its model form from either RANS or LES. LES closure models are algebraic in nature and are considered too elementary for PANS purposes as the PANS closure model should closure as the PANS closure model should be able to represent the physics of a larger range of scales including the entire turbulence spectrum.

In this paper, we develop the k-ω version of the PANS model. In PANS, the unresolved specific dissipation rate, ω_u is given by:

$$\omega_u = \frac{\varepsilon_u}{\beta^* k_u} \tag{5.14}$$

where k_u and ε_u are the PANS unresolved kinetic energy and unresolved dissipation rate respectively. β*(=0.09) is a fixed model parameter.

$$k_u = \frac{1}{2}\tau\left(V_i,V_j\right) \tag{5.15}$$

$$\varepsilon_u = \upsilon\tau\left(\frac{\partial V_i}{\partial x_j},\frac{\partial V_i}{\partial x_j}\right) \tag{5.16}$$

The kinetic energy, dissipation and the specific dissipation of the total fluctuations are denoted by k, ε and ω respectively. In PANS, the filter width can be controlled by specifying either the ratios of unresolved-to-total kinetic energy, f_k and unresolved-to-total turbulent frequency, f_ω or the ratios of unresolved-to-total kinetic energy and unresolved-to-total dissipation rate, f_ε. These model parameters are defined as:

$$f_k = \frac{k_u}{k};\ f_\varepsilon = \frac{\varepsilon_u}{\varepsilon} \tag{5.17}$$

$$f_\omega = \frac{\omega_u}{\omega} = \frac{\varepsilon_u / \beta^* k_u}{\varepsilon / \beta^* k} = \frac{f_\varepsilon}{f_k} \tag{5.18}$$

For any filter width, the closure for the SFS term $\tau(V_i,V_j)$ can be obtained by using the Boussinesq approximation:

$$\tau\left(V_i,V_j\right) = -\upsilon_u\left(\frac{\partial U_i}{\partial x_j}+\frac{\partial U_j}{\partial x_i}\right)+\frac{2}{3}k_u\delta_{ij} \tag{5.19}$$

where $\upsilon_u = k_u / \omega_u$ is the eddy viscosity of the unresolved scales. In order to solve equation (5.19) we need to prescribe suitable transport models for k_u and ω_u.

For the PANS k-ω model derivation we start with revised Wilcox k-ω model [19]

$$\frac{\partial k}{\partial t} + \bar{U}_j \frac{\partial k}{\partial x_j} = P - \beta^* k\omega + \frac{\partial}{\partial x_j}\left(\frac{\upsilon_T}{\sigma_k}\frac{\partial k}{\partial x_j}\right) \tag{5.20}$$

$$\frac{\partial \omega}{\partial t} + \bar{U}_j \frac{\partial \omega}{\partial x_j} = \alpha \frac{P\omega}{k} - \beta\omega^2 + \frac{\partial}{\partial x_j}\left(\frac{\upsilon_T}{\sigma_\omega}\frac{\partial \omega}{\partial x_j}\right) \tag{5.21}$$

where $\bar{U}$ is the mean velocity, P is the production of the RANS kinetic energy, ω is the RANS specific dissipation rate, ν_T is the total RANS eddy viscosity $(\upsilon_T = k/\omega)$; β*, α and β are model coefficients.

The evolution equation of kinetic energy for PANS and RANS can be related according to:

$$\frac{\partial k_u}{\partial t} + \bar{U}_j \frac{\partial k_u}{\partial x_j} = f_k\left(\frac{\partial k}{\partial t} + \bar{U}_j \frac{\partial k}{\partial x_j}\right) + \dot{f}_k k \tag{5.22}$$

where $\dot{f}_k$ represents the rate of change of f_k following a mean fluid particle. Here, we will restrict our consideration to constant f_k case $\left(\dot{f}_k = 0\right)$.

Then, the evolution equation for the unresolved kinetic energy can be justifiably written in classical RANS form [33]:

$$\frac{\partial k_u}{\partial t}+U_j\frac{\partial k_u}{\partial x_j}=\mathrm{P}_u-\beta^* k_u\omega_u+T_{ku} \tag{5.23}$$

where, $\mathrm{P}_u=\tau\left(V_i,V_j\right)U_{i,j}$ and $T_{ku}=\left(\nu_t/\sigma_k\, k_{u,j}\right)_{,j}$. The unresolved-scale production $\left(\mathrm{P}_u\right)$ is due to the spectral transfer of kinetic energy from resolved to unresolved scales, and not only due to direct interaction with the mean flow. This spectral-transfer production appears in closed form requiring no further consideration. Substituting the RANS equation for kinetic energy (5.20) into (5.22), we get:

$$\frac{\partial k_u}{\partial t}+U_j\frac{\partial k_u}{\partial x_j}=f_k\left[\mathrm{P}-\beta^* k\omega+\frac{\partial}{\partial x_j}\left(\frac{\nu_t}{\sigma_k}\frac{\partial k}{\partial x_j}\right)\right]+\left(U_j-\bar{U}_j\right)\frac{\partial k_u}{\partial x_j} \tag{5.24}$$

To achieve the required f_k, equations (5.23) and (5.24) must be consistent with one another. From these equations we can write

$$\mathrm{P}_u-\beta^* k_u\omega_u+T_{ku}=f_k\left(\mathrm{P}-\beta^* k\omega+\frac{\partial}{\partial x_j}\left(\frac{\nu_t}{\sigma_k}\frac{\partial k}{\partial x_j}\right)\right)+\left(U_j-\bar{U}_j\right)\frac{\partial k_u}{\partial x_j} \tag{5.25}$$

The relationship between various RANS terms and the corresponding PANS terms are now evident. Equating the source/sink terms (local processes) we get:

$$\mathrm{P}_u-\beta^* k_u\omega_u=f_k\left(\mathrm{P}-\beta^* k\omega\right) \tag{5.26}$$

From this the RANS production can be expressed in terms of PANS variables (noting $\omega=\omega_u/f_\omega$; $k=k_u/f_k$):

$$\mathrm{P} = \frac{1}{f_k}\left(\mathrm{P}_u - \beta^* k_u \omega_u\right) + \beta^* \frac{k_u \omega_u}{f_\omega f_k} \tag{5.27}$$

This relationship will be useful later to close the PANS dissipation equation. Comparing the transport terms of PANS and RANS from equation (5.25):

$$T_{ku} + \left(\bar{U}_j - U_j\right)\frac{\partial k_u}{\partial x_j} = f_k \frac{\partial}{\partial x_j}\left(\frac{\nu_t}{\sigma_k}\frac{\partial k}{\partial x_j}\right) = \frac{\partial}{\partial x_j}\left(\frac{\nu_t}{\sigma_k}\frac{\partial k_u}{\partial x_j}\right) \tag{5.28}$$

The model for the transport term can now be surmised:

$$T_{ku} \equiv \frac{\partial}{\partial x_j}\left(\frac{\nu_t}{\sigma_k}\frac{\partial k_u}{\partial x_j}\right) - \left(\bar{U}_j - U_j\right)\frac{\partial k_u}{\partial x_j} = \frac{\partial}{\partial x_j}\left(\frac{\nu_u f_\omega}{\sigma_k f_k}\frac{\partial k_u}{\partial x_j}\right) - \left(\bar{U}_j - U_j\right)\frac{\partial k_u}{\partial x_j} \tag{5.29}$$

since, $\nu_u / \nu_t = f_k / f_\omega$.

Now the only unclosed term is the transport of SFS kinetic energy due to the resolved velocity fluctuations $\left(U_j - \bar{U}_j\right)$. In the PANS k_u-ε_u context, it was shown by Murthi [34] that the resolved fluctuating scale does not contribute much towards the transport of the unresolved fluctuating field statistics. This is due to the mismatch in length and time scales of the resolved and unresolved fields. A similar assumption in the PANS k_u-ω_u context leads to:

$$\left(\bar{U}_j - U_j\right)\frac{\partial k_u}{\partial x_j} = 0 \tag{5.30}$$

The completed closure model for the SFS transport term from equation (5.29) is:

$$T_{ku} = \frac{\partial}{\partial x_j}\left(\frac{\nu_u}{\sigma_{ku}}\frac{\partial k_u}{\partial x_j}\right) \tag{5.31}$$

where the turbulent Prandtl number $\left(\sigma_{ku}\right)$ is:

$$\sigma_{ku} \equiv \sigma_k \frac{f_k}{f_\omega} \tag{5.32}$$

It was also shown in [34] that for lower Reynolds numbers, the resolved-scale transport may scale linearly with resolved0scale eddy viscosity leading to:

$$\left(\bar{U}_j - U_j\right)\frac{\partial k_u}{\partial x_j} \approx \frac{\partial}{\partial x_j}\left(\frac{\nu_r}{\sigma_k}\frac{\partial k_u}{\partial x_j}\right) \tag{5.33}$$

where $\nu_r = \nu_t - \nu_u$. Upon substitution into equation (5.29), this leads to

$$\sigma_{ku} \equiv \sigma_k \tag{5.34}$$

This completes the modeling of the SFS kinetic energy equation.

We develop the unresolved turbulent frequency equation based on the definition of the resolution control parameter f_ω given by equation (5.18).

$$\frac{\partial \omega_u}{\partial t} + \bar{U}_j \frac{\partial \omega_u}{\partial x_j} = f_\omega\left(\frac{\partial \omega}{\partial t} + \bar{U}_j \frac{\partial \omega}{\partial x_j}\right) = f_\omega\left(\alpha \frac{\mathrm{P}\omega}{k} - \beta\omega^2 + \frac{\partial}{\partial x_j}\left(\frac{\nu_t}{\sigma_\omega}\frac{\partial \omega}{\partial x_j}\right)\right) \tag{5.35}$$

As RANS variables are not known, to close the ω_u equations, all terms must be expressed in PANS variables $(k_u, \omega_u, \mathrm{P}_u)$ and PANS parameters(f_k, f_ω). We then have:

$$\frac{\partial \omega_u}{\partial t} + U_j \frac{\partial \omega_u}{\partial x_j} = \alpha \frac{\mathrm{P}\omega_u}{k_u} f_k - \beta \frac{\omega_u^2}{f_\omega} + \frac{\partial}{\partial x_j}\left(\frac{\nu_t}{\sigma_\omega} \frac{\partial \omega_u}{\partial x_j} \right) + \left(U_j - \bar{U}_j \right) \frac{\partial \omega_u}{\partial x_j} \tag{5.36}$$

The last two remaining unclosed term are the RANS kinetic energy production, P (determined from equation (5.27) and the transport due to the resolved scales -$\left(\bar{U}_j - U_j\right)$ term.

$$\frac{\partial \omega_u}{\partial t} + U_j \frac{\partial \omega_u}{\partial x_j} = \alpha \frac{\mathrm{P}_u \omega_u}{k_u} - \beta' \omega_u^2 + \frac{\partial}{\partial x_j}\left(\frac{\nu_u}{\sigma_{\omega u}} \frac{\partial \omega_u}{\partial x_j} \right) \tag{5.37}$$

where,

$$\beta' = \alpha \beta^* - \frac{\alpha \beta^*}{f_\omega} + \frac{\beta}{f_\omega} \tag{5.38}$$

As in the derivation of the unresolved kinetic energy, we again assume zero resolved-scale transport for high Reynolds number flow [34] leading to:

$$\sigma_{\omega u} \equiv \sigma_\omega \frac{f_k}{f_\omega} \tag{5.39}$$

For the low Reynolds number, we invoke the argument [34] that the resolved-scale transport is proportional to the eddy-viscosity of the resolved fluctuations leading to:

$$\sigma_{\omega u} \equiv \sigma_\omega \tag{5.40}$$

Finally, the two-equation PANS model can be summarized as

$$\frac{\partial k_u}{\partial t} + U_j \frac{\partial k_u}{\partial x_j} = \mathrm{P}_u - \beta^* k_u \omega_u + \frac{\partial}{\partial x_j}\left(\frac{\nu_u}{\sigma_{ku}} \frac{\partial k_u}{\partial x_j} \right) \tag{5.41}$$

$$\frac{\partial \omega_u}{\partial t} + U_j \frac{\partial \omega_u}{\partial x_j} = \alpha \frac{\mathrm{P}_u \omega_u}{k_u} - \beta' \omega_u^2 + \frac{\partial}{\partial x_j}\left(\frac{\nu_u}{\sigma_{\omega u}} \frac{\partial \omega_u}{\partial x_j} \right) \tag{5.42}$$

where,

$$\beta' = \alpha\beta^* - \frac{\alpha\beta^*}{f_\omega} + \frac{\beta}{f_\omega} \tag{5.43}$$

In these equations viscous transport has also been included. The values for various coefficients are:

$$\beta^* = 0.09; \alpha = 5/9; \beta = 0.075; \sigma_k = 2.0; \sigma_\omega = 2.0$$

The PANS k-ω model parameters f_k and f_ω can be varied to resolve the right amount of energy depending on the Reynolds number of the flow and required physical resolution. The sensitivity of the PANS model to the flow Reynolds number manifests via f_ω. The model filter width should be in commensurate with the numerical resolution. Guidelines for judicious prescription of the PANS k-ε model resolution control parameters for a given grid are presented in Girimaji and Abdol-Hamid [10].

In this paper, we will perform simulation by keeping the resolution control parameters f_k and f_ω constant throughout the domain. This facilitates in (i) assessing the effect of f_k and

f_ω in a clear manner; and (ii) minimizing the commutation errors that arise due to spatially-varying filters. The PANS k-ω model simulations for both the flow fields studied were performed for varying f_k. As the Reynolds number considered for both the flow fields is considerably high, the f_ε value was fixed at one leading to $f_\omega = 1/f_k$.

The next step is the verification and validation study. Two test flows are used for this purpose: Flow past a backward facing step and circular cylinder. Verification entails comparison of *a-priori* specified reduction in eddy viscosity against the *a-posteriori* computed value. This comparison establishes if indeed PANS k_u-ω_u delivers the prescribed degree of reduction. In the validation stage we compare PANS k_u-ω_u model results against experimental and detached eddy simulations (DES)/LES results. Also provided are the PANS k_u-ε_u results.

3. Cylinder Flow Simulation

Several investigations have been made to simulate flow past a circular cylinder using variable resolution methods. Travin et al. [35] tested the application of DES model for this flow and met with partial success. Vatsa and Singer [36] used the same DES model on their production code TNLS3D to simulate the circular cylinder test case and found that second-order schemes could capture the flow behavior with reasonable accuracy. Elmiligui et al. [37] implemented the PANS model into the PAB3D code and reported the potential of the PANS model for such complex flows. They did not report any velocity statistics in their study. The current study is aimed at computing the cylinder flow test case using the new formulation proposed in Section 2.

3.1. Simulation set-up

The schematic of the computational domain used to perform the cylinder flow simulations is shown in Figure 24. The inlet is placed at distance of –15d from the cylinder centre. A constant velocity profile with zero turbulence intensity is imposed at the inlet boundary. The total length in the streamwise direction is 30d. The domain stretches from -15d to 15d in the cross flow direction. The spanwise length of the domain which is 2d is identical to the large eddy simulation (LES) domain chosen by Breuer [16] with which the PANS results are compared. Slip boundary conditions are imposed on the top and bottom surfaces of the domain. The lateral walls are defined as periodic boundaries. Outflow boundary conditions are imposed at the domain outlet. The flow is initialized with non-zero values for turbulence quantities. The grid used to perform the simulations is a structured O-grid with a grid resolution of 240 × 320 in the cross-sectional plane. The spanwise width of the domain has 32 control volumes. The grid consists of hexahedral cells with grid clustering in the vicinity of the cylinder. The simulations are set-up and computed using the commercial FLUENT CFD package augmented with used defined functions (UDF).

3.2. Comparison between PANS k_u-ε_u and PANS k_u-ω_u models

The simulations of flow past a circular cylinder at Re_D 1.4×10^5 were performed to access the PANS model performance in these highly unsteady and three-dimensional flows with complex shear layer interactions. The PANS k_u-ω_u simulations were performed for f_k values of 0.5 and 1.0. PANS computation with $f_k = 1.0$ is essentially an unsteady RANS (URANS) computation. The resolution control parameter for the dissipation scales is set to unity for this high Reynolds number simulation i.e. $f_\varepsilon = 1$. So 2.0 for $f_k = 0.5$. These simulations are compared with PANS k_u-ε_u simulation with $f_k = 0.5$ and 1.0. Also data from other experimental and numerical results are plotted alongside for complete validation of the PANS model. Each simulation was performed for a total of $120D/U_o$ time units before any data was collected. This is to allow for statistically steady vortex shedding to be established. Once statistically stationary state is established, the data from the latter part of the simulation is gathered over a period of $150D/U_o$ time-units which includes 60 shedding cycles to compute the flow statistics. For cases with large fluctuations (f_k = 0.5, 0.4), more time was allowed for the flow to settle down and the statistics were compiled over a larger flow time.

3.2.1 Viscosity ratio recovery

Recovery of the prescribed viscosity ratio is critical for successful performance of the PANS closure model as indicated in Chapter III. A comparison of the performance between PANS k_u-ε_u and PANS k_u-ω_u in achieving the specified viscosity reduction is plotted in Figure 25. The PDFs of the computed viscosity ratio plotted in this figure indicate that the PANS k_u-ω_u closure model achieves the pre-specified viscosity in a larger portion of the domain leading to improved accuracy. The narrow PDFs for the PANS k_u-ω_u model imply that there is greater correlation between the unresolved and the resolved field. Increased accuracy is attributed to the improvement of the closure model performance in the near wall region.

3.2.2 Mean velocity statistics

Mean streamwise velocity statistics along the wake centerline for various PANS simulations is compared with DES results of Travin et al. [35] and experimental results of Cantwell and Coles [18] in Figure 26. The DES results predict a very large recirculation bubble in the wake region compared to experimental data. The size of the recirculation bubble predicted by the PANS k_u-ε_u model and the PANS k_u-ω_u models is very similar for matching f_k value of 0.5. The URANS prediction (f_k = 1.0) is more accurate for the RANS k-ω closure. In the far-wake region, the PANS k_u-ε_u with f_k = 0.5 reaches the asymptotic limit predicted by the experiments whereas the PANS k-ω with f_k = 0.5 is more similar to DES results.

Comparison of the mean streamwise velocities at various locations in the near-wake region of the cylinder flow is presented in Figure 27. Mean velocity data from DES is available for this quantity. At x/D = 1.0, the PANS k_u-ε_u with $f_k = 0.5$ predicts the mean velocity statistics with reasonable accuracy. At the centre of the wake defect the PANS k_u-ε_u with $f_k = 0.5$ is more accurate than the PANS k_u-ω_u simulation with matching f_k value. Further away from the trough the PANS k_u-ω_u model shows very good agreement with the experimental data. At x/D = 3.0, the PANS k_u-ω_u with $f_k = 0.5$ behavior is similar to that predicted by the experiments throughout the wake defect. The mean normal velocity statistics at x/D = 1.0 is shown in Figure 28. The agreement of the PANS k_u-ε_u and the PANS k_u-ω_u model results with the measured data is satisfactory. The PANS k_u-ω_u model predictions are more accurate than the PANS k_u-ε_u model predictions and match the experimental results with minimal discrepancy.

3.2.3 Mean integral quantities

The distribution of mean pressure coefficient (C_p) on the cylinder surface is presented in Figure 29. The experimental data plotted alongside for comparison purposes is the laminar separation (LS) case of Cantwell and Coles [18]. Numerical data obtained from DES of Travin et al. [35] is also plotted alongside. In the current simulations the turbulence model is active throughout the domain but the flow Reynolds number is close to that of the LS case. Also, the inflow turbulence level is very low, somewhat simulating laminar flow. Both the PANS k_u-ε_u model computations ($f_k = 1.0$ and 0.5) presented over predict the peak pressure drop whereas the PANS k_u-ω_u model computations are closer to the LS cases presented. As the flow curves over the cylinder surface facing the flow, the pressure variation for PANS k_u-ε_u with $f_k = 0.5$ drops further down while the attached boundary layer transients to turbulence causing delayed separation. The URANS ($f_k = 1.0$) k_u-ω_u simulation also follows a similar trend, but the pressure drop is not as high as predicted by the PANS k_u-ε_u computation. The PANS k_u-ω_u with $f_k = 0.5$ is in satisfactory agreement with the LS cases presented. Its pressure recovery at the back of cylinder is closer to the experimental measurements of Cantwell and Coles [18].

The time-averaged integral quantities presented in Table 3 include the mean drag coefficient C_d, the base pressure at the back of the cylinder C_{pb}, the Strouhal number S_t which gives the frequency at which the harmonic vortices are shed, and the separation angle θ_s. The experimental data and the DES data for both the LS and the TS cases are presented alongside for comparison purposes. In general except for the PANS k_u-ω_u with $f_k = 0.5$ computation which predicts these quantities near to the LS measurements, the rest of the simulations predict these flow quantities closer to the TS limit. Improved near wall attributes of the k-ω model along with the reduction in eddy viscosity in PANS mode causes the PANS k_u-ω_u near wall behavior to be closer to the LS flow conditions enabling it to more closely capture this sub-critical Reynolds number behavior.

4. Backward Facing Step Simulations

VR models have also been tested for the backward facing step (BFS) flow which is the second validation case considered in this study. Basu et al. [38] compared several VR models including DES and PANS k_u-ε_u for this particular test case. Their analysis showed the promising nature of the PANS model in capturing the instantaneous flow structures and the mean flow statistics with reasonable accuracy. Frendi et al. [39] proposed a new formulation for the resolution control parameter f_ε and analyzed the effect of f_ε on the PANS modeling capability to simulate the BFS test case. They also compared the PANS model performance with DES and URANS methods.

4.1. Simulation set-up

The BFS simulations performed to validate the PANS k_u-ω_u model are based on experiments of Driver and Seegmiller [40]. The Reynolds number of the flow (based on free-stream velocity, U_∞ and step height, h) is 37,500. The inlet section of the domain prior to the sudden expansion has a length of $4h$. The length of the domain in the post-expansion section is 30*h*. The vertical height of the domain at the exit is 9*h* making the expansion ratio (ER) equal to 1.125. The width of the domain in the spanwise direction is 4h.

The grid details for the BFS case used in this study are shown in Figure 30. The grid resolution of the inlet section is 50 × 115 × 36 in the streamwise, crosswise and spanwise directions respectively. The grid nodes are placed equidistant in the streamwise and spanwise directions. In the wall-normal direction, the grid nodes are clustered towards the lower wall so that the grid size does not exceed y^+ of unity. In the post-expansion section, 280 grid nodes are placed along the streamwise direction with grid clustering towards the step so that at the step, $x^+ \approx 1$. In the vertical direction a non-uniform distribution of 215 grid nodes of which 100 grid nodes placed within the step height with grid clustering at the wall regions is specified ($y^+ < 1$). The spanwise distribution of the grid nodes is uniform with 36 cells.

The boundary conditions specified are consistent with the experiments. A channel flow profile generated from a RANS simulation is imposed at the inlet. Figure 31 compares the inlet velocity profile used for the BFS simulations with the experimental velocity profile at the inlet showing that the boundary layer thickness prior to the step is closely matched for both the simulations and the experiments (δ_{99} = 1.5h). The top and the bottom walls along with the step are specified with no-slip boundary conditions. The spanwise extremes of the domain are specified as periodic boundaries. Outflow boundary conditions are specified at the outlet.

4.2. Results and comparison studies

The present PANS k_u-ω_u simulations were performed for f_k value of 0.4, 0.5 and 1.0. The statistics obtained from these simulations are compared with experimental results of Driver and Seegmiller [21] and with PANS k_u-ε_u simulations at f_k = 0.2 performed by

Frendi et al. [39]. The PANS k_u-ε_u simulations were performed with spatially varying f_ε whereas the present PANS k_u-ω_u computations were performed with a constant f_ε throughout the domain. The simulations were performed for a total time of 232h/U_o. Initial data corresponding to 145h/U_o were discarded to allow for the passage of initial transience.

4.2.1 Mean velocity statistics

The spanwise-averaged mean x-velocity statistics at various locations downstream of the step are presented in Figure 32. Experimental results and the PANS k_u-ε_u simulations are also plotted alongside for better assessment of the PANS k_u-ω_u model performance. In general, the PANS k_u-ε_u model over-predicts the mean velocity statistics whereas the PANS k_u-ω_u model under predicts these statistics. The PANS k_u-ω_u model predictions improve as we move further downstream from the sudden expansion. Consistent with PANS bridging theory, the accuracy improves as we decrease the f_k value from 1.0 to 0.4.

4.2.2 Turbulent kinetic energy profiles

The time-averaged non-dimensional turbulent kinetic energy profiles at various locations downstream of the step are presented in Figure 33. The thin lines in these figures represent the unresolved part k_u and the total turbulent kinetic energy shown as thick lines. These two quantities is compared with experimental and the PANS k_u-ε_u model simulations. In the vicinity of the wall, PANS k_u-ω_u model with $f_k = 0.4$ shows very good agreement with the experiments whereas the PANS k_u-ε_u model shows reasonable agreement with the experiments away from the wall ($y/h > 4.0$). This is consistent with the general nature of k-ε and k-ω models: former is better in free shear flows and letter is superior in near-wall region. The unresolved part of the turbulent kinetic energy which is obtained from model equations is considerably lesser than the total turbulent kinetic energy as observed in the plots and it decreases as we reduce f_k value. Although there are discrepancies between the PANS data and the experimental results, the maximum discrepancy is within 6% of the experimental data and it decreases further downstream of the step.

4.2.3 Spanwise-averaged pressure coefficient and skin-friction coefficient

Figure 34 shows the distribution of spanwise-averaged mean static pressure downstream of the step along the lower wall for various f_k values simulated. PANS k_u-ε_u data is not available to make comparisons with the present simulations. Close to the step (x/h < 4.0), the pressure coefficient (C_p) distribution for the different simulations plotted is identical. In the region $4 < x/h < 8$, the PANS model computation with the smallest f_k is the most accurate. Away from the step, the simulations over-predict the recovery of C_p.

The distribution of the step-side mean skin friction coefficient (C_f) is shown in Figure 35. Before the trough, f_k = 1.0 simulations is closer to the measured value. After the peak, the PANS simulations with lower f_k are more accurate than the unsteady RANS (f_k = 1.0) simulations. The PANS simulations performed predict slow recovery of C_f with f_k = 0.4 results being the most accurate in comparison to the experimental data. Towards the exit, the simulations under predict the C_f distribution.

4.2.4 Reattachment length

Table 4 presents the reattachment lengths (x_r) predicted by various simulations. The experimental data predicts the reattachment of the flow to occur at x/h = 6.26. In the present simulations, the reattachment length is determined from spanwise averaged mean skin friction coefficient (C_f) variation on the bottom wall beyond the step. The accuracy of the PANS k_u-ω_u model predictions improve with decreasing f_k value. The PANS k_u-ω_u

model with f_k = 0.4 predicts the reattachment length closest to the experimental data among the simulations compared with x_r = 6.58.

4.2.5 Turbulent structures

The increase in the physical resolution of the simulation with decrease in the f_k value is clearly shown in Figure 36 and Figure 37. The rationale for improved accuracy with decreasing f_k value is apparent from the instantaneous iso-surface contours of vorticity shown in these figures. These qualitative results reflect the PANS model capability to capture the three-dimensional effects and the evolution of the turbulent eddies. For f_k = 1.0 simulations, the flow is laminar-like and two-dimensional as there are no vortical structures with x-direction as the axis-of -rotation. Reducing the f_k value leads to formation of the Kelvin-Helmholtz instabilities and the breakdown of the larger vortices into finer scales of motion as the flow is convected downstream. The three-dimensionality and eddy break-up is even more enhanced for the f_k = 0.4 simulations clearly reflecting the reduced damping by the model equations as desired.

5. Conclusions

This study presents a new formulation of the PANS VR model. The nature of the PANS VR model permits selecting any formulation of the RANS model and hybridizing it to provide closure for sub-filter stresses. The RANS k-ω model which has several proven advantages over the k-ε model is chosen as the closure model to chosen as the closure model. The present study is the first implementation of the PANS k_u-ω_u model to complex problems of engineering relevance. Two flow problems were modeled using the PANS k_u-ω_u model.

The cylinder flow simulations performed comparing the different PANS formulations indicate that the near-wall behavior for the PANS k_u-ω_u formulation is in very good agreement with the experimental observations. As shown by the mean velocity statistics, the PANS k_u-ε_u model seems to capture the far wake asymptotic behavior fairly accurately. The PANS k_u-ω_u model with reduced f_k values predicts the mean integral quantities to agree with the LS data which is the expected behavior for this simulated flow Reynolds number. However the PANS k_u-ε_u model predict the separation to be turbulent and thereby over predict the separation and the pressure at the back of the cylinder.

The PANS k_u-ω_u model is also applied to a backward facing step flow. Comparison between the k-ε and k-ω model formulations for the PANS model imply that the PANS k-ω model is better suited to simulate this case as the model shows satisfactory agreement with the experimental observation. The flow structures from the simulations reveal the effect of reducing the f_k value which the PANS filter parameter. The PANS k_u-ω_u model with $f_k = 1.0$ completely fails to capture any unsteadiness. The reduced f_k simulations capture the unsteady three-dimensional characteristics for this flow. For the smallest f_k simulated the vortices are sharper and more complex leading to better visualization of the evolving flow as it moves away from the sudden expansion.

CHAPTER VI

EDDY VISCOSITY CLOSURE MODEL FOR RAPIDLY DISTORTED TURBULENCE

1. Introduction

The physical foundation for the eddy viscosity formulation is the assumption of local equilibrium [41] wherein production and dissipation are nearly in balance. This is achieved when the mean velocity gradient driven production process is in balance with the non-linear processes of cascade and dissipation. Eddy viscosity models (EVM) fail to capture the correct turbulence effects when there is even a slightest shift away from equilibrium assumption [42] and even worse at the rapid distortion (RD) limit. Rapidly distorted turbulence represents the limit in which the linear processes completely dominate the non-linear effects. The characteristic frequency of the linear process is the mean strain rate (S) and the corresponding frequency of the non-linear process is ε/k (where k and ε are the turbulent kinetic energy and dissipation). In equilibrium turbulence the dimensionless parameter Sk/ε takes a value in the range 3 -5 and in RD limit the value is even larger. The nature of turbulence is fundamentally different in rapid distortion regime when compared to the near-equilibrium regime. In the near equilibrium regime, the turbulence stresses are amenable to a viscous constitutive relation – stress is proportional to strain rate – validating the eddy viscosity closure paradigm. In the RD regime, however, the turbulent stresses are proportional to the total strain rate – the hallmark of elastic behavior. Also in the RD limit the pressure strain term in the Reynolds stress evolution equation slows down the *isotropization* process which is the redistribution of turbulent stresses among components by the active strain rate to make turbulence more isotropic [43]. The application of the eddy viscosity model in the elastic region leads to unphysical high shear stress values violating the

Realizability constraint[1] [44]. The realizability condition can be written in several forms as indicated by Ghosal [45]. The exaggerated shear stress values in turn lead to over prediction of turbulence and gross errors in the calculation as observed by Kato and Launder [46] while simulating flow past a square cylinder. Ever since several limiting functions have been applied to EVM to limit this anomalous growth in turbulent kinetic energy production [46, 47]. While these methods have been reasonably successful, they do not directly address the issue of rapid distortion limiting behavior. The goal of this paper is to modify the EVM at large strain rates to render the closure model consistent with rapid distortion physics.

Our objective in the present study is two-fold. First, we develop modifications to EVM guided by algebraic Reynolds stress model (ARSM) to yield reasonable behavior in RD limit. Second, we perform computations using the proposed models to evaluate their performance in complex engineering flows.

The organization of this paper is as follows: In Section 2, we present the standard EVM and outline the difficulties encountered in RD limit. A strategy for making EVM consistent with RD physics is formulated in Section 3 and a closure model is proposed. Section 4 presents the details of the high lift airfoil configuration which is the test case considered to validate the proposed model. The computational details concerning our simulations for this study are presented in Section 5. Section 6 presents the results comparing the performance of the various models computed for the airfoil test case. In Section 7, we summarize the important conclusions from this study.

---

[1] Realizability is a mathematical constraint based on Cauchy Schwartz inequality for the Reynolds stress tensor which is a second-order positive semi-definite tensor.

2. Standard Eddy Viscosity Model

The standard EVM Boussinesq constitutive relation to calculate the Reynolds stresses is given by:

$$\overline{u_i u_j} = -2\nu_T S_{ij}^* + \frac{2}{3} k \delta_{ij} \tag{6.1}$$

where, $\overline{u_i u_j}$ is the Reynolds stress component, ν_T is the turbulent eddy viscosity, S_{ij} is the active strain rate $S_{ij}^* = \frac{1}{2}\left(\partial U_i / \partial x_j + \partial U_j / \partial x_i\right)$, k is the turbulent kinetic energy, and δ_{ij} is the Dirac-delta function. The turbulent eddy viscosity in the above formula is calculated using the Prandtl-Kolmogorov formula:

$$\nu_T = C_\mu k^2 / \varepsilon \tag{6.2}$$

The Boussinesq constitutive relation given by (6.1) can be written in terms of normalized anisotropy tensor [48] as:

$$b_{ij} = \frac{\overline{u_i u_j}}{2k} - \frac{1}{3}\delta_{ij} = -C_\mu \frac{k}{\varepsilon} S_{ij}^* = -C_\mu S_{ij} \tag{6.3}$$

where $S_{ij} = \frac{1}{2}\frac{k}{\varepsilon}\left(\partial U_i / \partial x_j + \partial U_j / \partial x_i\right)$ is the normalized strain rate. In the standard model C_μ is a constant (=0.09) and thus we have the typical viscous constitutive relation where stress is proportional to strain rate. By its very definition b_{ij} is bounded. $-1/3 \le b_{ij} \le 2/3$. The right hand side is however unbounded.

Typical values of turbulence to mean shear time scale ratio $\left(Sk/\varepsilon\right)$ for flow past an airfoil is shown in Figure 38. Upstream of the airfoil Sk/ε is very large and beyond the limits to which the standard EVM are designed to be valid. Turbulence is in *rapid distortion* state in this region of the domain. In the RD limit $\left(|S| \gg \varepsilon/k\right)$, S_{ij}^* can take extremely large values. Thus in the RD limit, the standard model violates realizability [44]. Durbin [47] outlines a practical resolution to the realizability problem by restricting the growth of the turbulent time-scale, τ $\left(= k/\varepsilon\right)$ to limit b_{ij} to the range $-1/3 \le b_{ij} \le 2/3$. Durbin's correction has been a popular choice to correct the stagnation point anomaly for bluff body flows. The correction is a simple inequality relation which in terms of C_μ variation for 2D flows can be written as [47]:

$$C_\mu \le \frac{0.4714}{\sqrt{S_{ij}S_{ij}}} \tag{6.4}$$

This correction is only applicable for stagnation point flows and is not a general fix for turbulence in the RD limit as mentioned in the introduction.

Detailed rapid distortion analysis [48] shows that the Reynolds stress is proportional to total strain:

$$\overline{u_i u_j} \sim \int S_{ij} dt \tag{6.5}$$

This implies that the Boussinesq constitutive relations are qualitatively incorrect for turbulence in the RD limit. We propose new modifications to two-equation EVM thereby enabling the model application to turbulent flow situations in the RDT limit. The modifications are easily amenable to hybridization which is the final goal of our proposition. The natures of the proposed modifications are based on varying the model parameter C_μ in (6.2). For standard EVM, C_μ is a constant (= 0.09) and its value is calibrated for homogeneous shear flows. In the first modification, C_μ variation is based on algebraic Reynolds stress model (ARSM) of Girimaji [49]. The second modification proposed is based on simplifying the ARSM model of Girimaji [49] in the RDT limit.

3. Model Derivation and Implementation

3.1. Variable C_μ model (1): Modification based on Girimaji ARSM

The first form of C_μ modification is derived from the ARSM model of Girimaji [49]. The constitutive relation for the anisotropy tensor in its most general form for two-dimensional mean flow is given by [49] (Equation 16):

$$b_{ij} = G_1 S_{ij} + G_2\left(S_{ik}W_{kj} - W_{ik}S_{kj}\right) + G_3\left(S_{ik} - \tfrac{1}{3}S_{mn}S_{mn}\delta_{ij}\right) \tag{6.6}$$

where, $G_1 - G_3$ are the unknown coefficients, W_{ij} is the normalized rotation rate given by:

$$W_{ij} = \frac{1}{2}\frac{k}{\varepsilon}\left(\frac{\partial U_i}{\partial x_j} - \frac{\partial U_j}{\partial x_i}\right) \tag{6.7}$$

The coefficients $G_1 - G_3$ can be evaluated from (see [49] for details) :

$$\begin{gathered} G_1\left[L_1^0 - \eta_1 L_1^1 G_1\right] = L_2 + \frac{\eta_1}{3}L_3G_3 + 2\eta_2 L_4 G_2; \\ G_2 = \frac{-L_4G_1}{L_1^0 - \eta_1 L_1^1 G_1}; \quad G_3 = \frac{2L_3G_1}{L_1^0 - \eta_1 L_1^1 G_1}. \end{gathered} \tag{6.8}$$

where, η_1 and η_2 are the invariants of the strain and rotation rate tensors given by:

$$\eta_1 = S_{ij}S_{ij}$$

$$\eta_2 = W_{ij}W_{ij} \tag{6.9}$$

The other parameters defined for completeness are:

$$L_1^0 \equiv \frac{C_1^0}{2} - 1;\ L_1^1 \equiv C_1^1 + 2;\ L_2 \equiv \frac{C_2}{2} - \frac{2}{3};\ L_3 \equiv \frac{C_3}{2} - 1;\ L_4 \equiv \frac{C_4}{2} - 1.$$

$$C_1^0 = 3.4;\ C_1^1 = 1.8;\ C_2 = 0.36;\ C_3 = 1.25;\ C_4 = 0.40. \tag{6.10}$$

In the first form of variable C_μ model being proposed in this work, we formulate C_μ to vary depending on η_1 and η_2. The model is a linear truncated version of the Girimaji ARSM model [49]. The Reynolds stress anisotropy constitutive relation given by equation (6.6) becomes:

$$b_{ij} = G_1 S_{ij} \tag{6.11}$$

Comparing equations (6.11) and (6.3), we get: $-G_1 = C_\mu$. From Girimaji [49], $G1$ is calculated using:

$$G_1 = \begin{cases} \dfrac{L_1^0 L_2}{\left(L_1^0\right)^2 + 2\eta_2 \left(L_4\right)^2} & \text{for } \eta_1 = 0; \\ \dfrac{L_1^0 L_2}{\left(L_1^0\right)^2 - \frac{2}{3}\eta_1 \left(L_3\right)^2 + 2\eta_2 \left(L_4\right)^2} & \text{for } L_1^1 = 0; \\ -\dfrac{p}{3} + \left(-\dfrac{b}{2} + \sqrt{D}\right)^{1/3} + \left(-\dfrac{b}{2} - \sqrt{D}\right)^{1/3} & \text{for } D > 0; \\ -\dfrac{p}{3} + 2\sqrt{\dfrac{-a}{3}} \cos\left(\dfrac{\theta}{3}\right) & \text{for } D < 0 \text{ and } b < 0; \\ -\dfrac{p}{3} + 2\sqrt{\dfrac{-a}{3}} \cos\left(\dfrac{\theta}{3} + \dfrac{2\pi}{3}\right) & \text{for } D < 0 \text{ and } b > 0. \end{cases} \qquad (6.12)$$

where, the following definitions have been used:

$$\begin{gathered} p \equiv -\frac{2L_1^0}{\eta_1 L_1^1};\; r \equiv -\frac{L_1^0 L_2}{\left(\eta_1 L_1^1\right)^2}; \\ q \equiv \frac{1}{\left(\eta_1 L_1^1\right)^2}\left[\left(L_1^0\right)^2 + \eta_1 L_1^1 L_2 - \tfrac{2}{3}\eta_1 \left(L_3\right)^2 + 2\eta_2 \left(L_4\right)^2\right]; \\ a \equiv \left(q - \frac{p^2}{3}\right);\; b \equiv \frac{1}{27}\left(2p^3 - 9pq + 27r\right). \\ D = \frac{b^2}{4} + \frac{a^3}{27} \end{gathered} \qquad (6.13)$$

The modification for C_μ in terms of G_1 is implemented as presented above without any limiting function as in Durbin correction [47].

3.2. Variable C_μ model (2): Modification based on Girimaji ARSM in the RDT limit

The variation of C_μ as a function of η_1 for various η_2 computed from equation (6.12) is plotted in Figure 39. For smaller values of η_1, C_μ is practically constant and as η_1

increases the different η_2 manifolds converge on the $\eta_2 = 0$ manifold indicating that $\eta_2 = 0$ is a good approximation for large η_1 (~ Sk/ε). In the RDT limit ($\eta_1 >> 1$), the cubic equation (6.8) degenerates to a quadratic equation given by:

$$G_1\left[-\eta_1 L_1^1 G_1\right] = L_2 + \frac{\eta_1}{3} L_3 G_3 + 2\eta_2 L_4 G_2;$$

$$G_2 = \frac{-L_4}{-\eta_1 L_1^1}; \quad G_3 = \frac{2L_3}{-\eta_1 L_1^1}. \tag{6.14}$$

Further approximating that $\eta_2 = 0$ (based on Figure 39) in equation (6.14), we get an expression for C_μ as:

$$-G_1 = C_\mu = \frac{0.3668}{\sqrt{\eta_1}} \tag{6.15}$$

We implement this into the CFD solver as a limit on the C_μ coefficient as:

$$C_\mu = \min\left[0.3668\left(\frac{\varepsilon}{Sk}\right), 0.09\right] \quad \text{for RANS } k\text{-}\varepsilon \text{ model}$$

$$\beta^* = \min\left[0.3668\left(\frac{0.09\omega}{S}\right), 0.09\right] \quad \text{for RANS } k\text{-}\omega \text{ model} \tag{6.16}$$

The proposed modification is such that for smaller values of Sk/ε the coefficient C_μ remains constant and as Sk/ε reaches RDT limit, the coefficient C_μ varies so as to limit the growth of turbulent kinetic energy consistent with rapid distortion physics.

3.3. Model implementation

For the purposes of this study, the background model used to implement the variable C_μ modification discussed above is the RANS k-ω model of Wilcox [19]. To ensure correct log-law slope of κ^{-1} the closure coefficient, σ_ω is specified as:

$$\sigma_\omega = \frac{\kappa^2}{\sqrt{\beta^*}\left(\frac{\beta}{\beta^*} - \alpha\right)} \tag{6.17}$$

where, κ(= 0.41) is the von Kármán constant. α (= 0.556) and β(= 0.075) are the k-ω model coefficients. The model coefficient σ_k is specified such that:

$$\left(\frac{\sigma_\omega}{\sigma_k}\right)_{C_\mu = 0.09} = \left(\frac{\sigma_\omega}{\sigma_k}\right)_{C_\mu\,\mathrm{var}\,iable} \tag{6.18}$$

In Figure 39, we plot the variation of C_μ as a function of η_1 for the various models proposed. The realizability line shown in the figure is based on the Durbin's realizability criteria presented in Equation (6.4). It is clear that having constant C_μ (=0.09) violates realizability condition for $\eta_1 \geq 20$. The C_μ variation as per the Girimaji ARSM model [49] which is the variable C_μ model (1) satisfies realizability for all values of η_1 and η_2 and so does the variable C_μ model (2). Hence it is clear from this figure that all of the proposed C_μ models satisfy realizability condition thereby assuring realistic flow predictions.

4. Model Assessment for the Airfoil Flow

Flow past an airfoil provides a rigorous evaluation of the proposed realizable, variable C_μ two equation turbulence model. The computational analysis for each study was performed using the commercial CFD software tool FLUENT. The two C_μ modifications proposed in Section 3 are implemented into the FLUENT solver via compiled user defined functions (UDF).

Current simulations for the airfoil flow are based on the geometry and flow conditions first considered in the ECARP project [50] and later in the LESFOIL project [51]. The geometry of the flow is an Aerospatiale A-airfoil. The Reynolds number based on the chord length, C is 2.1×10^6. The angle of attack, α is 13.3^o which is the angle of attack at which maximum lift is achieved for this particular geometry. The freestream Mach number is 0.15. The Aerospatiale A-airfoil has been used as a test case to examine the ability of EVM as well as large eddy simulations (LES). In ECARP project [50] a wide range of turbulence models from simple algebraic models to more complex Reynolds stress models were used to assess their performance for this flow. The conclusion from this project reported that two-equation turbulence models over predict the turbulent kinetic energy in the in the leading edge region. The models fail to predict trailing edge separation. All of the EVM models need some sort of modifications to limit the growth of production of turbulence. Modifications of the standard models improve the results in the separation region but these modifications are not based on physical reasoning and are ad-hoc.

The LESFOIL project was conceived to assess the feasibility of performing LES for separated flows at high Reynolds numbers. Issues considered included performance of the sub-grid scale models, development of efficient numerical schemes, and also evaluate near-wall models based on eddy-viscosity concept. LESFOIL project concluded that successful LES computations are only possible by resolving near-wall turbulence and transition simulated properly. LESFOIL project concluded that hybrid turbulence models such as detached eddy simulations [6] (DES) and other hybrid RANS/LES models are better suited for this flow.

The airfoil test case chosen is an ideal test for evaluating the variable C_μ model as the standard EVM violates realizability condition for this flow. At the leading edge the geometry of the flow causes the flow to be highly strained as the flow curves over the airfoil leading edge causing EVM to predict overproduction of turbulence and hence causing excessive amounts of turbulent kinetic energy at the leading edge even though experiments predict this flow to be practically laminar at the leading edge and turbulence creeps in into the flow only towards the trailing edge.

5. Details of the Geometry and the Computational Set-up

Figure 40 presents the airfoil geometry and the various flow features of the Aerospatiale A-airfoil as observed in experimental studies performed at ONERA and reported in the ECARP project [50]. At the leading edge the flow is laminar with a laminar boundary layer. The flow transitions to turbulence at around $x/C = 0.12$ forming a separation bubble in this region. The turbulent boundary layer which is attached to the geometry separates at around $x/C = 0.83$. In the suction side of the airfoil the boundary layer is tripped to turbulence at around $x/C = 0.3$.

The computational grid (see Figure 41) considered in this study is a structured grid based on the mandatory grid used in the ECARP project [50]. The grid resolution considered is 512×180. This grid resolution was identified as appropriate for the current study after a grid resolution analysis. Figure 42 and Figure 43 present the results of coefficient of pressure (C_p) distribution and skin friction coefficient (C_f) respectively along the airfoil surface for the various grids considered with the standard RANS k-ω model as the turbulence model. From these figures it is clear that 512×180 grid is adequate for trustworthy computations. The entire curved region is considered as inlet boundary. Constant velocity is specified at the inlet such that the free-stream Mach number matches the experimental conditions. The outlet is defined as pressure outlet with the flow exiting to atmospheric conditions. The airfoil is defined as a no-slip boundary. The numerical schemes used in the computation are summarized in Table 5.

6. Results and Discussion

6.1. *Qualitative comparison between standard EVM and Variable C_μ EVM*

Figure 44 and Figure 45 provide a qualitative comparison between the standard and the variable C_μ EVM model. The flow fields predicted by the two C_μ modifications are qualitatively similar. Figure 44 displays the contours of the turbulent kinetic energy in the vicinity of the airfoil. In Figure 44a, the contours obtained from the standard model indicate that upstream of the stagnation point there is a region of high turbulent kinetic energy. However the flow features as observed in experiments and illustrated in Figure 40 indicate that the region upstream of the stagnation point is practically laminar. Spurious behavior of the flow near the leading edge affects rest of the flow computation downstream. On the other hand, the variable C_μ model computations are consistent with the experimental observations for the variation of turbulent kinetic energy in the vicinity of the airfoil as can be observed in Figure 44b. We can infer that upstream of the stagnation point, the flow is practically laminar and turbulence creeps into the boundary layer as the flow proceeds downstream towards the trailing edge. The reasons for anomalous increase in the turbulent kinetic energy upstream of the stagnation point in Figure 45a can be obtained by observing the contours of production of turbulence in Figure 45a and Figure 45b. The standard model predicts very high values for production of turbulence in the upstream region because in this region production of turbulence grows as square of the strain rate as dictated by the EVM equations $\left(\mathrm{P} = \nu_T S^2\right)$. The variable C_μ model predicts lesser values for the production of turbulence in the upstream region as the model restricts the growth of production by reducing the value of the model constant C_μ in the upstream region. This is evident in Figure 46 which shows the contours of variation of the coefficient C_μ for different models proposed. In the upstream region, $Sk/\varepsilon >> 1$ and this state of turbulence is governed by RDT. In RDT limit, production of turbulence is proportional to the strain rate rather than square of the strain rate [44]. In the regions of high Sk/ε the proposed variable C_μ models reduce the value of C_μ to near zero, thereby reducing the turbulent viscosity and hence limiting the production of turbulent kinetic energy. The variable C_μ model (2) shows a slightly different behavior in the variation of C_μ than the variable C_μ model (1). The C_μ variation for the latter is over a larger portion of the domain. The variable C_μ model predictions are in agreement with RDT in regions of high Sk/ε.

6.2. Velocity and turbulent profiles

Figure 47 presents the streamwise velocity profiles along four wall stations on the suction side at x/C = 0.5, 0.825, 0.9 and 0.96. The velocity profiles at locations x/C = 0.5 and x/C = 0.825 are along the wall normal direction whereas the velocity profiles at x/C = 0.9 and x/C = 0.96 are taken along the direction normal to the chord. The Durbin correction is also plotted alongside the variable C_μ results for holistic comparison. Comparing between the standard k-ω model and the variable C_μ model we see that the modifications significantly improve the accuracy of the results and the results from the modified models are in better agreement with the experimental data than the standard model results. At x/C = 0.5, all of the variable C_μ models are in good agreement with the measurements in the vicinity of the wall. The variable C_μ model (1) shows the best agreement among the models compared at this station. As we proceed downstream towards the trailing edge, very close to the wall the Durbin correction shows the best agreement among the modifications compared but, further away from the wall the variable C_μ models are more accurate with the variable C_μ model (1) being the most closest to the experimental measurements. At stations x/C = 0.825, 0.9, and 0.96 the variable C_μ model (2) over predicts the velocity distribution in the vicinity of the wall and hence is unable to capture the extent of separation at the trailing edge. All the modified models predict separation to have occurred prior to the x/C = 0.96 station as can be observed in Figure 47d. Overall, the variable C_μ model (1) predicts the most accurate velocity profiles among the models compared.

Figure 48 displays the normal Reynolds stress profiles on the suction side at the same streamwise locations as the velocity profiles. All the modified models capture the variation of the Reynolds stresses accurately close to the wall. At the station x/C = 0.5, all the modifications over-predict the Reynolds stresses in the outer region of the boundary layer. As the flow over the airfoil decelerates downstream, the variable C_μ model (2) predicts quantitatively good results in comparison to the other two C_μ modifications and the Durbin correction in the outer region of the boundary layer at stations x/C = 0.825, 0.9 and 0.96. The predictions from the standard k-ω model are out of bounds of the plot area.

6.3. Streamline contours at trailing edge

The streamline patterns at the trailing edge of the airfoil as predicted by various models are shown in Figure 49. These patterns help us visualize the shape and size of the separation bubble at the trailing edge for different simulations. The standard model does not predict any separation at the trailing edge as can be seen in this figure. Among the modified models, the separation bubble predicted by the variable C_μ model (1) is closest to experimental observations. Variable C_μ model (2) also predicts separation at the trailing edge, but the degree of separation is very small. The separation bubble for experiments starts at around x/C = 0.83.

6.4. Distribution of pressure and skin friction coefficient

The distribution of wall pressure coefficient (C_p) along the airfoil surface as predicted by different models is shown in Figure 50. The standard k-ω model heavily under-predict the peak pressure on the suction side at the leading edge as the model predicts anomalous behavior in this region of the flow field. All of the variable C_μ models computed predict the C_p distribution on the suction side with reasonable accuracy, but in the region x/C > 0.5, the C_p distribution as predicted by these models is slightly below the experimental data.

The skin friction coefficient (C_f) distribution on the suction side of the airfoil is presented in Figure 51. All of the computational results plotted over-predict C_f prior to x/C = 0.5 station of the airfoil. This is due to the fact that the computations performed have the turbulence model active throughout the domain and there is no special treatment for transition. As the flow becomes turbulent in the experiments, the agreement between the experiments and the simulations improves. The fact that the standard k-ω model fails to capture trailing edge separation is clearly evident from the C_f plot. All three variable C_μ models agree very well with experimental measurements for the C_f distribution near the trailing edge. The variable C_μ model (2) slightly over-predicts C_f and thereby shows delayed separation in comparison to the other two modifications proposed and this is evident in the streamline contours of Figure 49.

6.5. Lift and Drag coefficients

The lift (C_L) and drag (C_D) coefficients from the various computations are presented in Table 6. The standard k-ω model predicts increased C_D and reduced C_L when compared to the experimental data. The variable C_μ models predict the force coefficients with reasonable accuracy. The models over predict C_D but the variable C_μ model (2) computation is closest to the experimental measurements. In terms of C_L prediction, the both the variable C_μ models under-predict this data.

7. Conclusion

Current study is aimed at improving the performance of standard two-equation RANS model in the RDT limit of turbulence where the turbulence to mean shear time-scale ratio is very large. This study has direct implication in development of more accurate closure models for PANS methodology. Many of the flow fields that we encounter in aerodynamics design are complex and exhibit features that the standard EVM are not designed to simulate. We propose two different modifications to the standard EVM. The modifications are based on varying C_μ. First, C_μ is modified based on the current strain rate and rotation rate tensors via the principles used in ARSM and second, a C_μ modification based on ARSM in the RDT limit is proposed. The proposed modifications are validated for a high lift airfoil configuration which exhibits complex physics phenomenon for the turbulence model to capture.

The variable C_μ models proposed and validated in this study address the issue of out-of equilibrium turbulence as in the case of the airfoil flow. All of the proposed modifications satisfy realizability and predict a physically realistic flow field. The modified models capture the phenomenon of trailing edge separation but predicted separation occurs after the location indicated by the experimental measurements. Among the modification proposed, the variable C_μ model (1) performs the best overall. The model captures the velocity profile with reasonable accuracy and the degree of separation predicted by the model is in agreement with experimental observations.

The modifications proposed in this study are applicable to any two-equation RANS model and since the formulation is not obtained from an inequality relation as in the Durbin correction it can be easily hybridized to be incorporated into PANS methodology.

CHAPTER VII

SUMMARY AND CONCLUSIONS

The main concern of this study is the continued development and validation of PANS, a variable resolution model for turbulent flow computations. Research efforts are directed towards analyzing the performance of the PANS model in simulating fundamental engineering flows. Four important studies are identified to provide justification for the PANS modeling capability as a VR model.

- First, we would like to know whether the computed flow field using the PANS model reflects the correct amount of physical fidelity intended i.e. whether the model equations provide the right amount of viscous dissipation and Chapter III verifies this aspect of PANS modeling and we also compare our approach with other VR models to evaluate the merits of these approaches. PANS, which achieves hybridization by modifying the transport equations provides for predictable physical resolution whereas VR models which reduce the constant C_μ to achieve hybridization produce an over-damped solution and hence are unpredictable. Results from this study establish the correctness of PANS modeling paradigm and also verifies the filtering consistency.

- Second, we study the fluctuations obtained from PANS decomposition. Many of the proposed VR models produce non-physical fluctuations. Our goal is to examine whether these fluctuations adhere to turbulence theory and hence follow the established turbulence scaling laws. In chapter IV, we develop a new framework to analyze the PANS fluctuations and establish that the characteristic length and time scales constructed from the unresolved turbulent flow field adhere to the turbulence scaling arguments. The ratios of these characteristic length and time scales are shown to have a universal behavior. Results from this study validate the PANS model and establish its suitability as VR model.

- Third, we examine the near-wall behavior of the PANS model. PANS model inherits the properties of the parent RANS model. PANS k_u-ε_u model does not capture the near-wall behavior accurately. We formulate the PANS k_u-ω_u model in Chapter V wherein we use the RANS k-ω model as the closure model which is proven to simulate wall-bounded flows with greater accuracy than RANS k-ε model. We show in Chapter V that the PANS k_u-ω_u model results show better agreement with experimental data for the test cases simulated as it captures the wall statistics more accurately than the PANS k_u-ε_u model. PANS k_u-ω_u model provides for application of the PANS VR model to a wide ranging of engineering flows and can be tuned to provide the best physical resolution possible with given computational resources.

- Finally, one of the observations from the PANS k_u-ω_u results for the BFS was the over-prediction of the turbulent kinetic energy in the outer layer of the boundary. This is common in flows where the state of turbulence is elastic in nature and is completely governed by RDT. To better understand the reasons for this anomalous behavior, we approach this problem in the RANS paradigm since the PANS closure model derives much of its properties from the parent RANS model. In Chapter VI, we analyze the behavior of standard RANS k-ω in flows where turbulence is in the RDT limit and propose modifications to improve the performance of the standard RANS models which are designed only for near-equilibrium flow situations. The modifications proposed on Chapter VI are based on sound physics and we show that the modified models can be used to successfully compute complex aerodynamic flow situations. The form of the proposed modifications also makes to easy amenable to hybridization and hence can be incorporated into PANS methodology.

An important aspect of partial averaging that has not been address in this study is the issue associated with commutation errors. In all the simulations presented in this work, the filter parameters f_k and f_ε/f_ω are maintained constant throughout the domain. By applying this homogeneous filter to the test cases which have a finite domain we introduce commutation errors into the solution. Future studies using the PANS model would likely include f_k varying as a function of space and time depending on the formula presented in Chapter III.

The nature of decomposition in PANS facilitates using any of the RANS models to provide closure for the SFS term. The SST model of Menter [52] which combines the advantages of both RANS k-ε and RANS k-ω models is a suitable choice for PANS closure. Preliminary studies have been conducted to formalize PANS-SST model. Future studies need to implement the PANS-SST model into CFD solvers and also investigate the effectiveness of various other RANS models to provide closure for the SFS term.

REFERENCES

[1] Hanjalic, K., 2005, Will RANS survive LES? A view of perspectives. *Journal of Fluids Engineering - Transactions ASME,* **127**(5), 831-839.

[2] Speziale, C.G., 1998, Turbulence modeling for time-dependent RANS and VLES: A review. *AIAA Journal,* **36**(2), 173-184.

[3] Spalart, P.R., 2000, Strategies for turbulence modelling and simulations. *International Journal of Heat and Fluid Flow,* **21**(3), 252-263.

[4] Girimaji, S.S., 2006, Partially-averaged Navier-Stokes model for turbulence: A Reynolds-averaged Navier-Stokes to direct numerical simulation bridging method. *Journal of Applied Mechanics-Transactions ASME,* **73**(3), 413-421.

[5] Sagaut, P., 2001, *Large eddy simulations for incompressible flows: an introduction* (Berlin, Springer)

[6] Spalart, P.R., Jou, W.-H., Streles, M., and Allmaras, S., 1997, Comments on the feasibility of LES for wings and on a hybrid RANS/LES approach, in *Proceedings of first AFOSR International Conference on DNS/LES*, Greyeden Press, Ruston, LA.

[7] Khorrami, M.R., Singer, B.A., and Berkman, M.E., 2002, Time-accurate simulations and acoustic analysis of slat free shear layer. *AIAA Journal,* **40**(7), 1284-1291.

[8] Fasel, H.F., von Terzi, D.A., and Sandberg, R.D., 2006, A methodology for simulating compressible turbulent flows. *Journal of Applied Mechanics-Transactions ASME,* **73**(3), 405-412.

[9] Batten, P., Goldberg, U., and Chakravarthy, S., 2002, LNS - An approach towards embedded LES, *AIAA 2002 - 0427*

[10] Girimaji, S.S., and Abdol-Hamid, K.S., 2005, Partially-averaged navier stokes model for turbulence: Implementation and validation, *AIAA 2005-0502*

[11] Girimaji, S.S., Jeong, E., and Srinivasan, R., 2006, Partially averaged Navier-Stokes method for turbulence: Fixed point analysis and comparison with

unsteady partially averaged Navier-Stokes. *Journal of Applied Mechanics-Transactions ASME,* **73**(3), 422-429.

[12] Lakshmipathy, S., 2004, *PANS method of turbulence simulation of high and low Reynolds number flows past a circular cylinder,* M.S. Thesis, Texas A&M University

[13] Germano, M., 1999, From RANS to DNS: Towards a bridging model. *ERCOFTAC SERIES,* **7** 225-236.

[14] Speziale, C.G., 1997, Computing non-equilibrium turbulent flows with time-dependent RANS and VLES, *15th ICNMFD*

[15] Schiestel, R., and Dejoan, A., 2005, Towards a new partially integrated transport model for coarse grid and unsteady turbulent flow simulations. *Theoretical and Computational Fluid Dynamics,* **18**(6), 443-468.

[16] Breuer, M., 2000, A challenging test case for large eddy simulation: High Reynolds number circular cylinder flow. *International Journal of Heat and Fluid Flow,* **21**(5), 648-654.

[17] Fluent Inc. FLUENT 6.2 user's guide 2006

[18] Cantwell, B., and Coles, D., 1983, An experimental study of entrainment and transport in the turbulence near wake of a circular cylinder. *Journal of Fluid Mechanics,* **136** 321-374.

[19] Wilcox, D.C., 2002, *Turbulence Modeling for CFD* (La Cañada, Calif., DCW Industries)

[20] Lakshmipathy, S., and Girimaji, S.S., 2006, Partially-averaged Navier-Stokes method for turbulent flows: k-ω model implementation, *AIAA 2006-119*

[21] Driver, D.M., and Seegmiller, H.L., 1985, Features of a reattaching turbulent shear layer in divergent channel flow. *AIAA Journal,* **23**(2), 163-171.

[22] Sagaut, P., Deck, S., and Terracol, M., 2006, *Multiscale and Multiresolution Approaches in Turbulence* (London, Imperial College Press)

[23] Frohlich, J., and von Terzi, D., 2008, Hybrid LES/RANS methods for the simulation of turbulent flows. *Progress in Aerospace Sciences,* **44**(5), 349-377.

[24] Muschinski, A., 1996, A similarity theory of locally homogeneous and isotropic turbulence generated by a Smagorinsky-type LES. *Journal of Fluid Mechanics,* **325** 239-260.

[25] Hunt, J.C.R., Moin, P., Lee, M., Moser, R.D., Spalart, P., Mansour, N.N., Kaimal, J.C., and Gaynor, E., 1988, *Cross correlation and length scales in turbulent flows near surfaces* (Secaucus, NJ, US, Springer-Verlag)

[26] Lakshmipathy, S., and Girimaji, S.S., 2007, Extension of Boussinesq turbulence constitutive relation for bridging methods. *Journal of Turbulence,* **8**(31), 1-21.

[27] Singh, S.P., and Mittal, S., 2004, Energy spectra of flow past a circular cylinder. *International Journal of Computational Fluid Dynamics,* **18**(8), 671-679.

[28] Lee, K., Yu, D.Z., and Girimaji, S.S., 2006, Lattice Boltzmann DNS of decaying compressible isotropic turbulence with temperature fluctuations. *International Journal of Computational Fluid Dynamics,* **20**(6), 401-413.

[29] Menter, F.R., 1992, Influence of freestream values on k-omega turbulence model predictions. *AIAA Journal,* **30**(6), 1657-1659.

[30] Kolmogorov, A.N., 1942, Equations of turbulent motion of an incompressible fluid. *Izvestia Academy of Sciences, USSR; Physics,* **6**(1 and 2), 56-58.

[31] Wilcox, D.C., 1988, Reassessment of the scale-determining equation for the advanced turbulence models. *AIAA Journal,* **26**(11), 1299-1310.

[32] Bardina, J.E., Huang, P.G., and Bardina, J.E., 1997, Turbulence modeling validation, *AIAA 97-2121*

[33] Germano, M., 1992, Turbulence: the filtering approach. *Journal of Fluid Mechanics,* **238** 325-336.

[34] Murthi, A., 2005, *Effect of turbulent transport models and grid spacing on pans calculations of a lid-driven cavity,* M.S. Thesis, Texas A&M University

[35] Travin, A., Shur, M., Strelets, M., and Spalart, P., 2000, Detached-eddy simulations past a circular cylinder. *Flow Turbulence and Combustion,* **63** 293-313.

[36] Vatsa, V.N., and A., S.B., 2003, Evaluation of a second-order accurate Navier-Stokes code for detached eddy simulation past a circular cylinder, *AIAA 2003-4085*

[37] Elmiligui, A., Abdol-Hamid, K.S., Massey, S.J., and Pao, S.P., 2004, Numerical study of flow past a circular cylinder using RANS, hybrid RANS/LES and PANS formulations, *AIAA 2004-4959*

[38] Basu, D., Hamed, A., and Das, K., 2005, DES, hybrid RANS/LES and PANS models for unsteady separated turbulent flow simulations, American Society of Mechanical Engineers, New York, NY 2255-2260.

[39] Frendi, A., Tosh, A., and Girimaji, S., 2007, Flow past a backward-facing step: Comparison of PANS, DES and URANS results with experiments. *International Journal for Computational Methods in Engineering Science and Mechanics,* **8**(1), 23 - 38.

[40] Driver, D.M., Seegmiller, H.L., and Marvin, J.G., 1987, Time dependent behavior of a reattaching shear layer. *AIAA Journal,* **25**(7), 914-919.

[41] Launder, B.E., Sandham, N.D., and Isaac Newton Institute for Mathematical, S., 2002, *Closure strategies for turbulent and transitional flows* (Cambridge, UK, Cambridge University Press)

[42] Craft, T.J., Launder, B.E., and Suga, K., 1996, Development and application of a cubic eddy-viscosity model of turbulence. *International Journal of Heat and Fluid Flow,* **17**(2), 108-115.

[43] Lavin, T.A., 2007, *Reynolds and Favre-averaged rapid distortion theory for compressible, ideal-gas turbulence,* M. S. Thesis, Texas A&M University

[44] Durbin, P.A., and Reif, B.A.P., 2001, *Statistical Theory and Modeling for Turbulent Flows* (Chichester, NY, Wiley)

[45] Ghosal, S., 1999, Mathematical and physical constraints on large-eddy simulation of turbulence. *AIAA Journal,* **37**(4), 425-33.

[46] Kato, M., and Launder, B.E., 1993, Modelling flow-induced oscillations in turbulent flow around a square cylinder. *ASME -Publications,* **157** 189 - 199.

[47] Durbin, P.A., 1996, On the k-3 stagnation point anomaly. *International Journal of Heat and Fluid Flow,* **17**(1), 89-90.

[48] Pope, S.B., 2000, *Turbulent Flows* (Cambridge, UK, Cambridge University Press)

[49] Girimaji, S.S., 1996, Fully explicit and self-consistent algebraic Reynolds stress model. *Theoretical and Computational Fluid Dynamics,* **8**(6), 387-402.

[50] Haase, W., European Computational Aerodynamics Research, P., European Commission. Directorate-General Xii, S.R., and Development, 1997, *ECARP : European Computational Aerodynamics Research Project : validation of CFD codes and assessment of turbulence models* (Braunschweig/Wiesbaden, Vieweg)

[51] Mellen, C.P., Frohlich, J., and Rodi, W., 2003, Lessons from LESFOIL project on large-eddy simulation of flow around an airfoil. *AIAA Journal,* **41**(4), 573-581.

[52] Menter, F.R., 1994, Two-equation eddy-viscosity turbulence models for engineering applications. *AIAA Journal,* **32**(8), 1598-1605.

APPENDIX A

The figures and tables referred to in the various chapters of this dissertation are presented in this appendix.

Table 1. Summary of test case for the cylinder flow simulations

Case	f_k	f_ε	*Grid*
Coarse	0.5	1.0	170 × 240 × 32
Medium	0.5	1.0	240 × 320 × 32
Fine	0.5	1.0	320 × 320 × 36

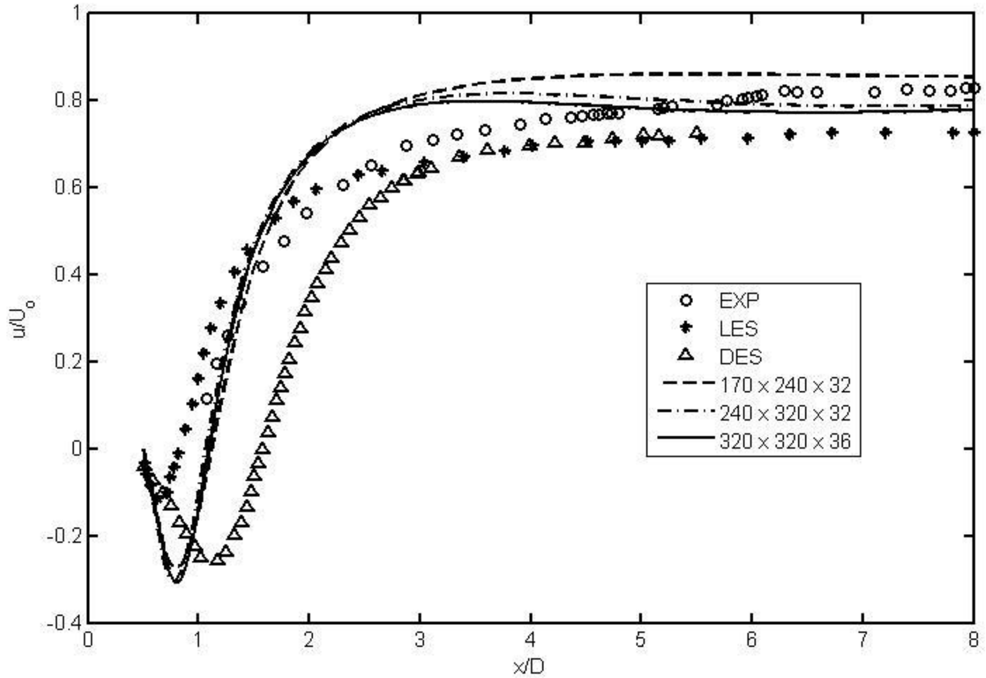

Figure 1. Mean streamwise velocity statistics along wake centerline for various grids

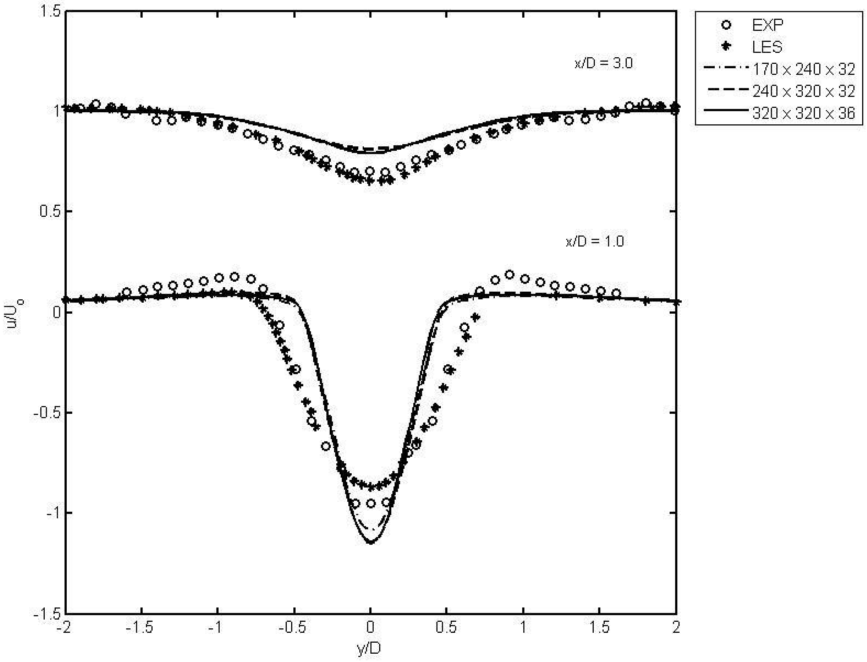

Figure 2. Mean streamwise velocity statistics at various x locations for various grids

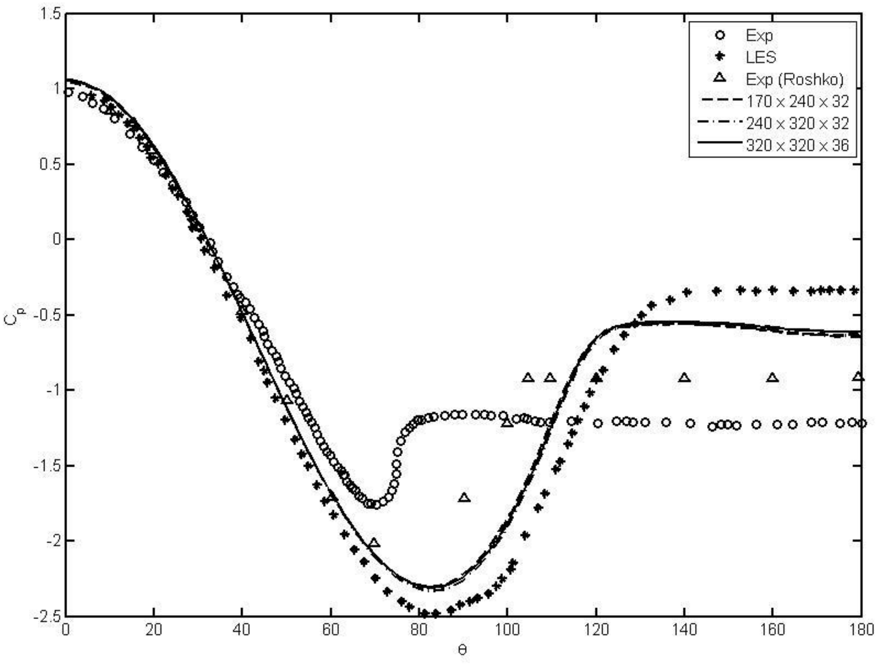

Figure 3. C_p distribution along the cylinder surface for various grids

Table 2. Summary of test case for the BFS simulations

Case	f_k	f_ε	*Grid*[1]
Coarse	0.4	1.0	50 × 115 × 36
			170 × 102 × 36
Medium	0.4	1.0	50 × 115 × 36
			280 × 215 × 36
Fine	0.4	1.0	50 × 115 × 36
			680 × 304 × 36

---

[1] First line is grid details for inlet section and second line is grid details for step section

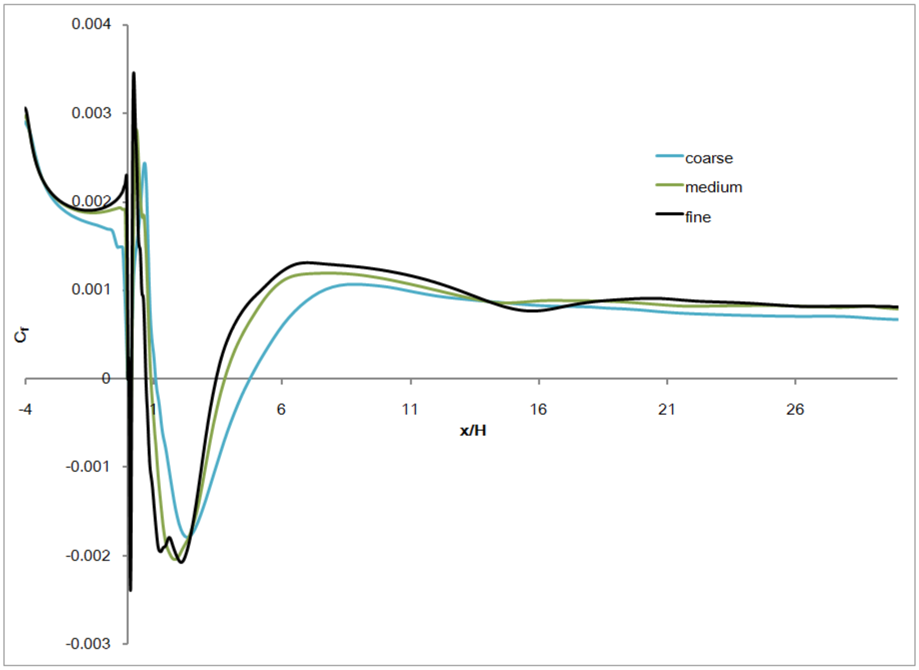

Figure 4. C_f distribution along the bottom wall for various grids

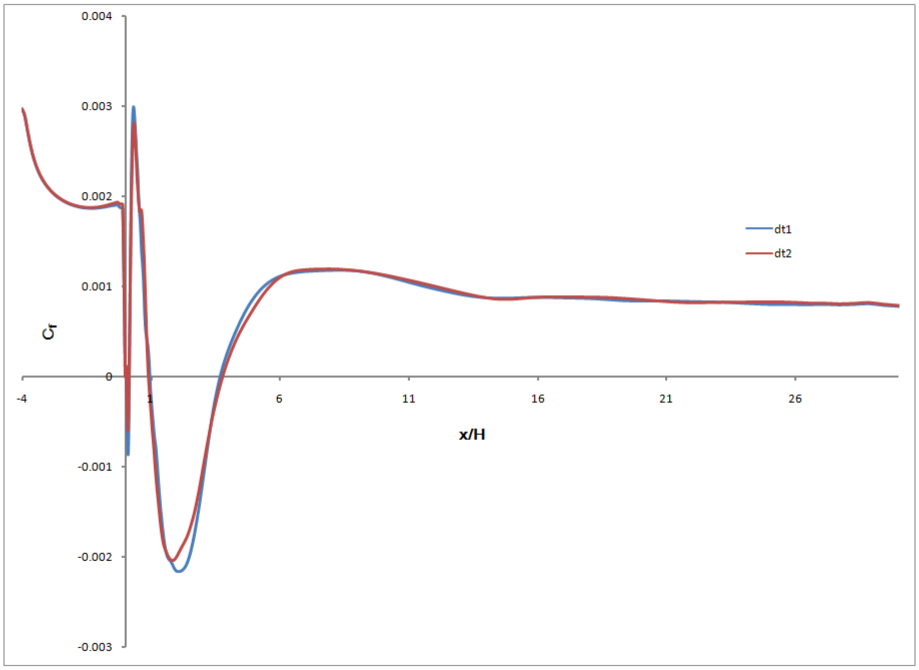

Figure 5. C_f distribution along the bottom wall for different times

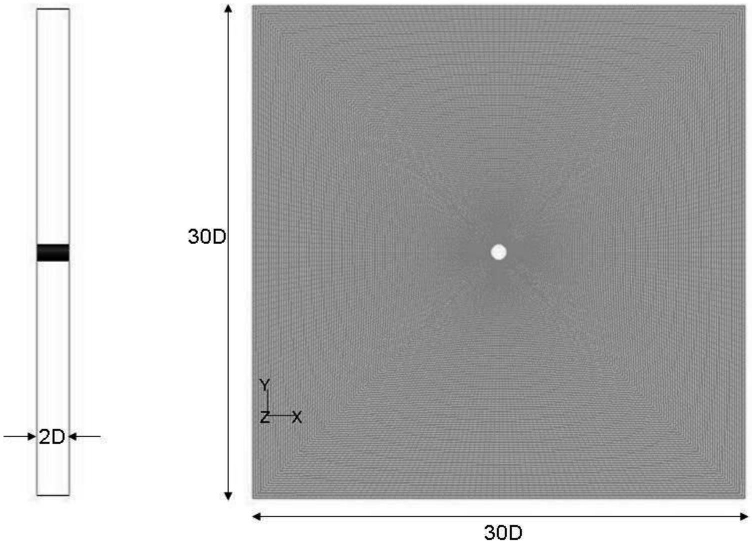

Figure 6. Computational domain for the cylinder flow simulations

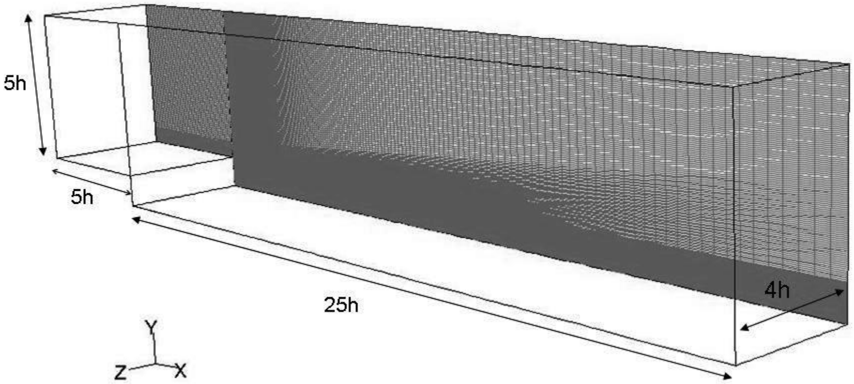

Figure 7. Computational domain for the backward facing step simulations

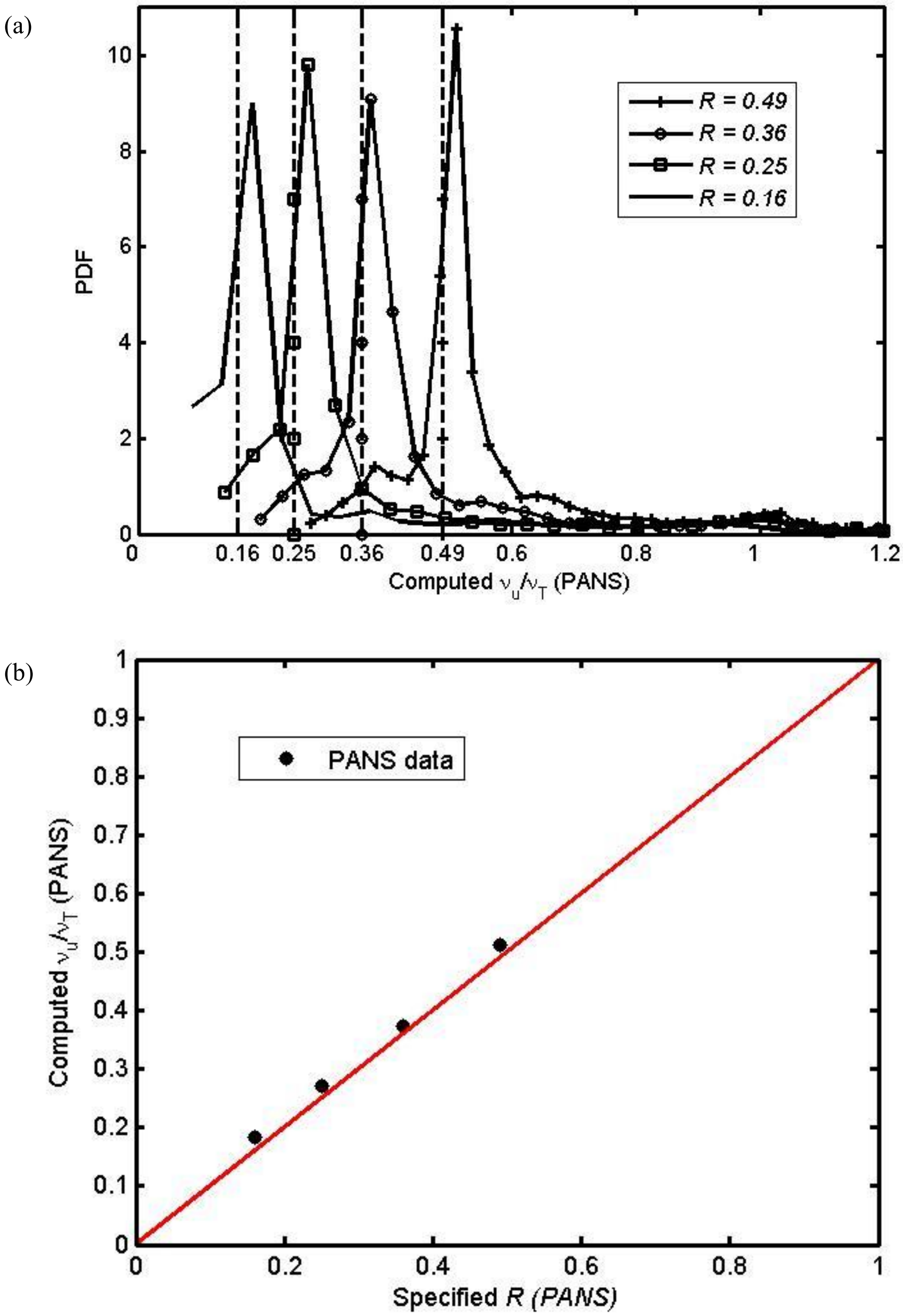

Figure 8. PANS computation. (a) PDF of computed viscosity ratio: Specified value (dashed line). (b). Curve-fit for the computed viscosity ratio peaks

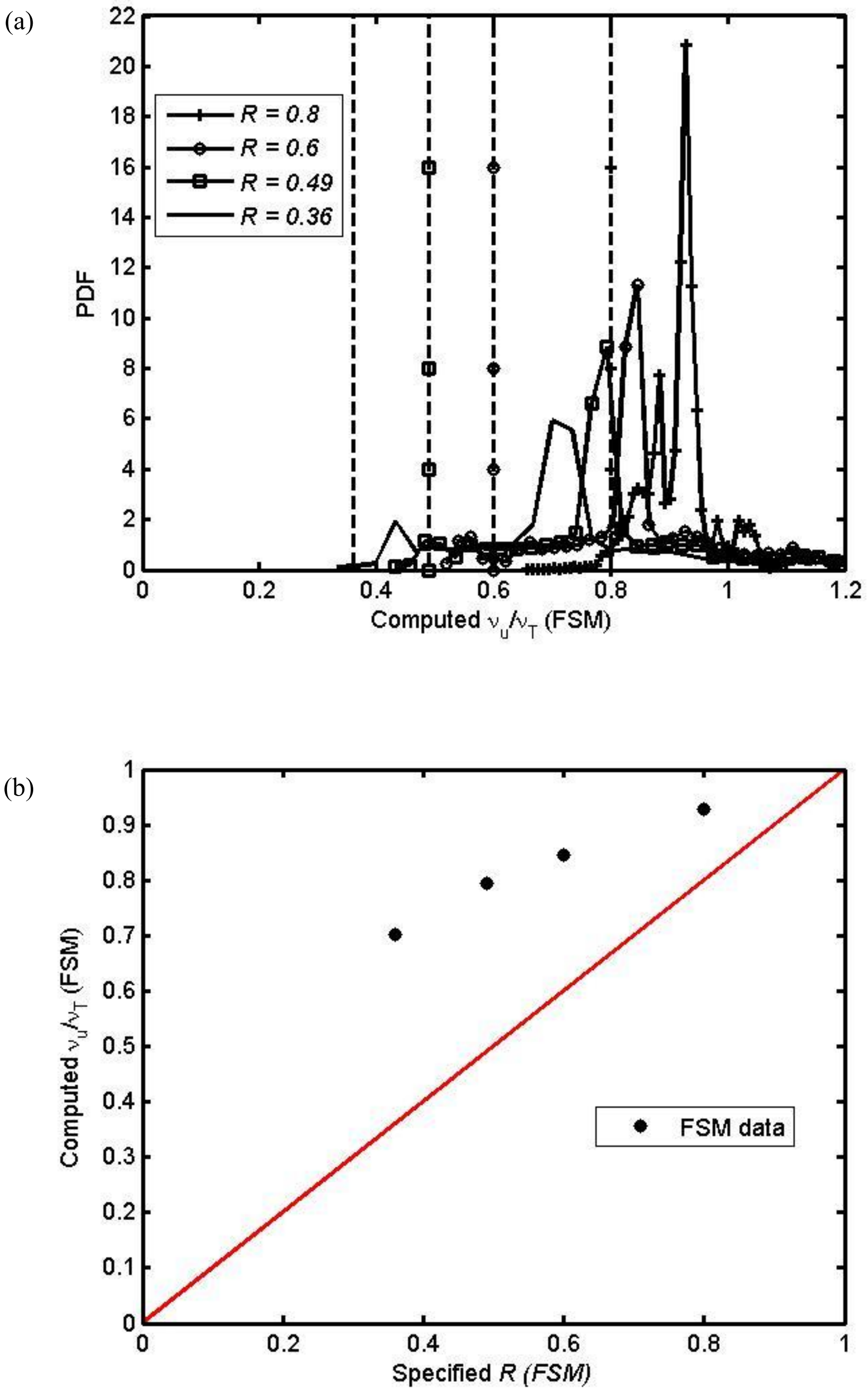

Figure 9. FSM computation. (a). PDF of computed viscosity ratio: Specified value (dashed line). (b). Curve-fit for the computed viscosity ratio

(a)

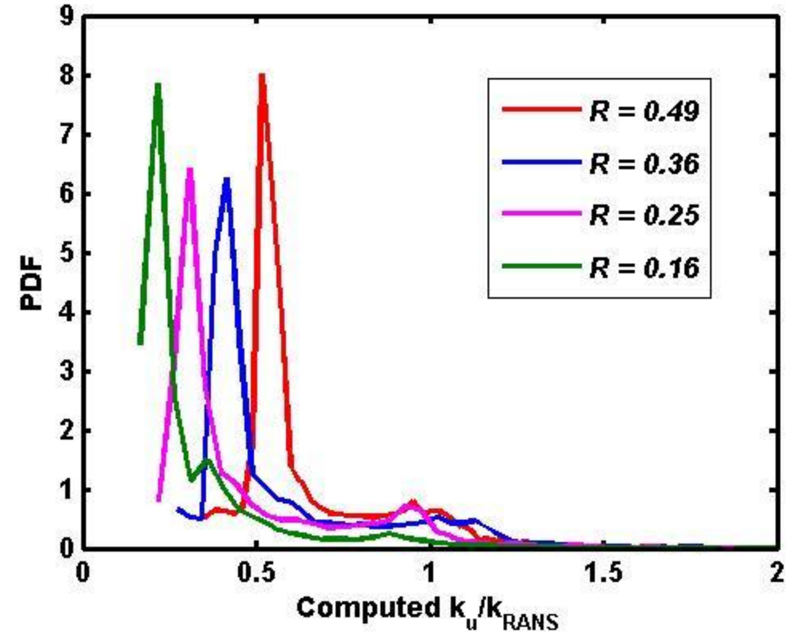

(b)

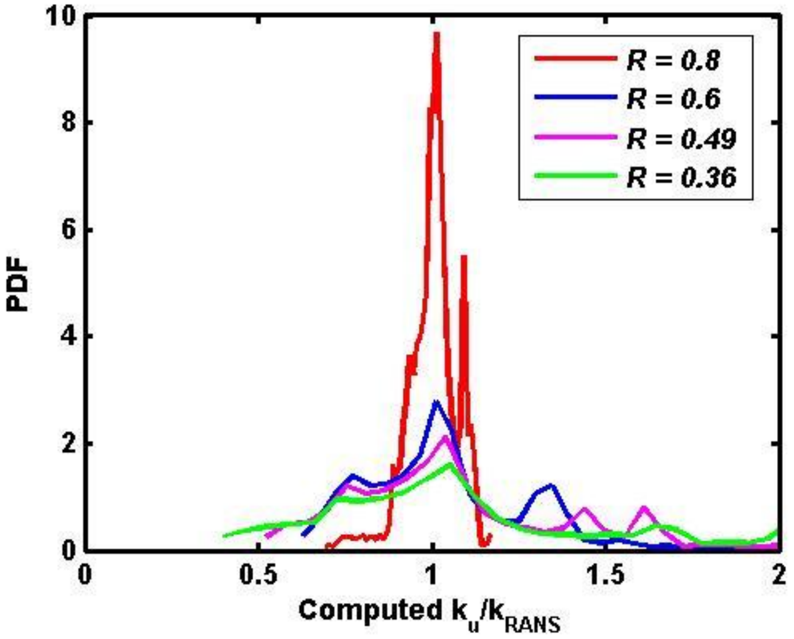

Figure 10. PDF of computed ratio of unresolved kinetic energy ratios. (a). PANS computations. (b) FSM computations

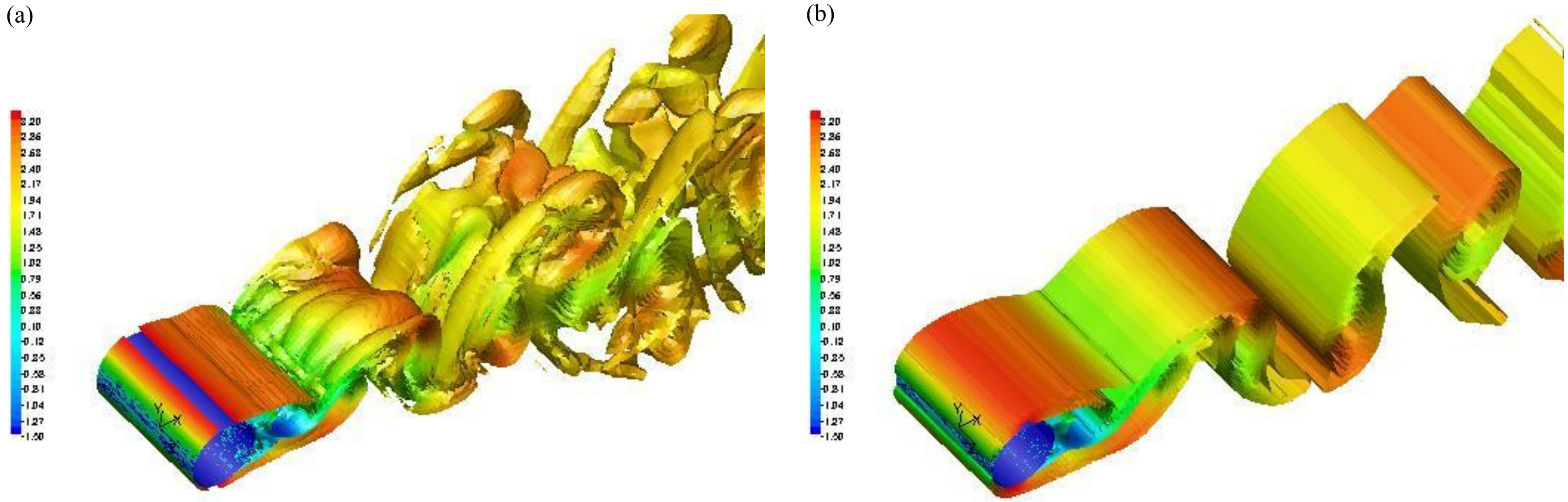

Figure 11. Iso-vorticity contours colored by x-velocity. (a) PANS. (b) FSM

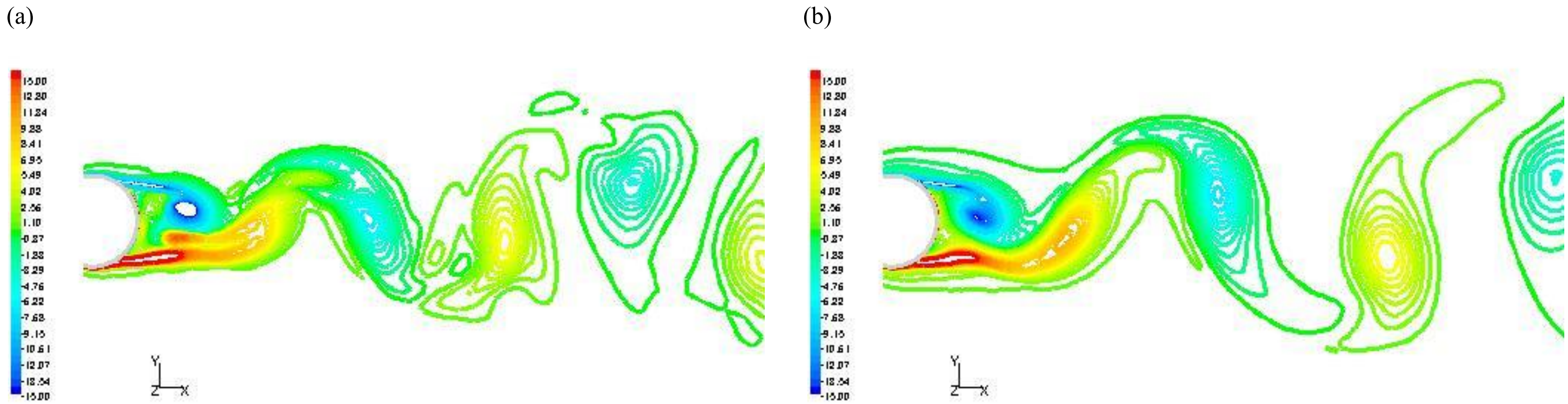

Figure 12. x-vorticity contours. (a) PANS. (b) FSM

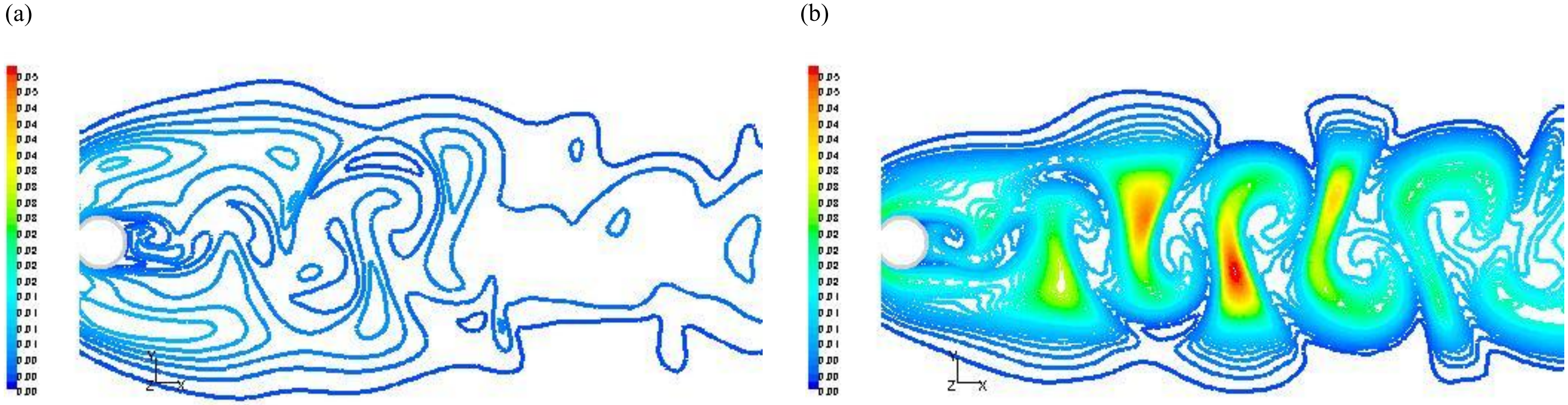

Figure 13. Contours for instantaneous eddy viscosity. (a) PANS. (b) FSM.

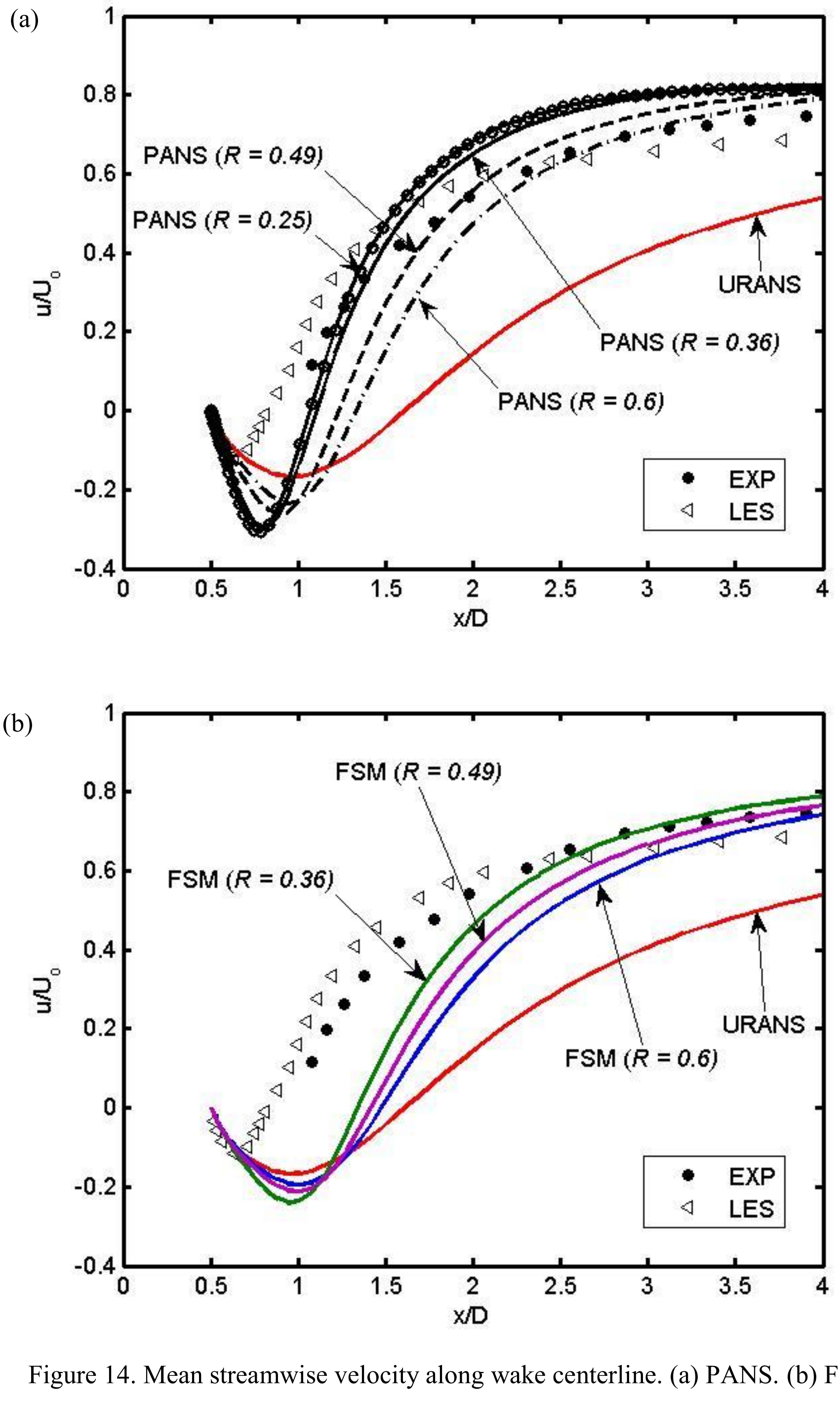

Figure 14. Mean streamwise velocity along wake centerline. (a) PANS. (b) FSM.

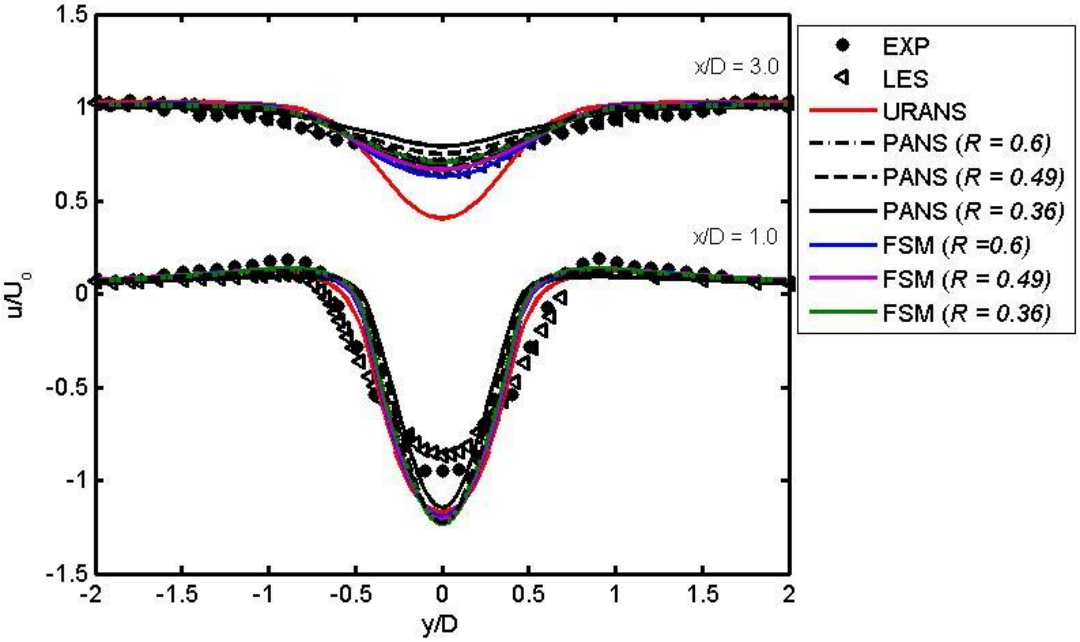

Figure 15. Mean streamwise velocity at various x-planes

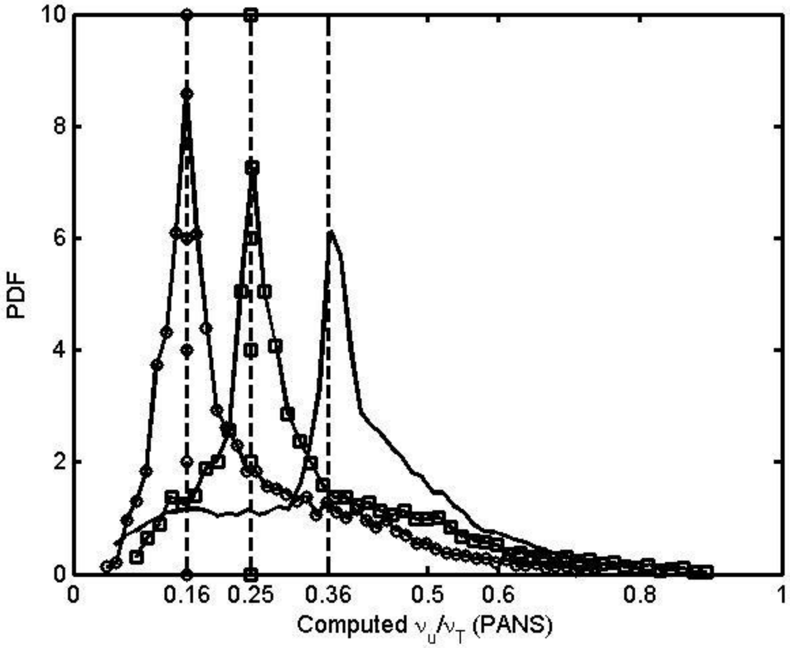

Figure 16. PDF of computed viscosity ratio in PANS k-ω calculation: Specified value (dashed line)

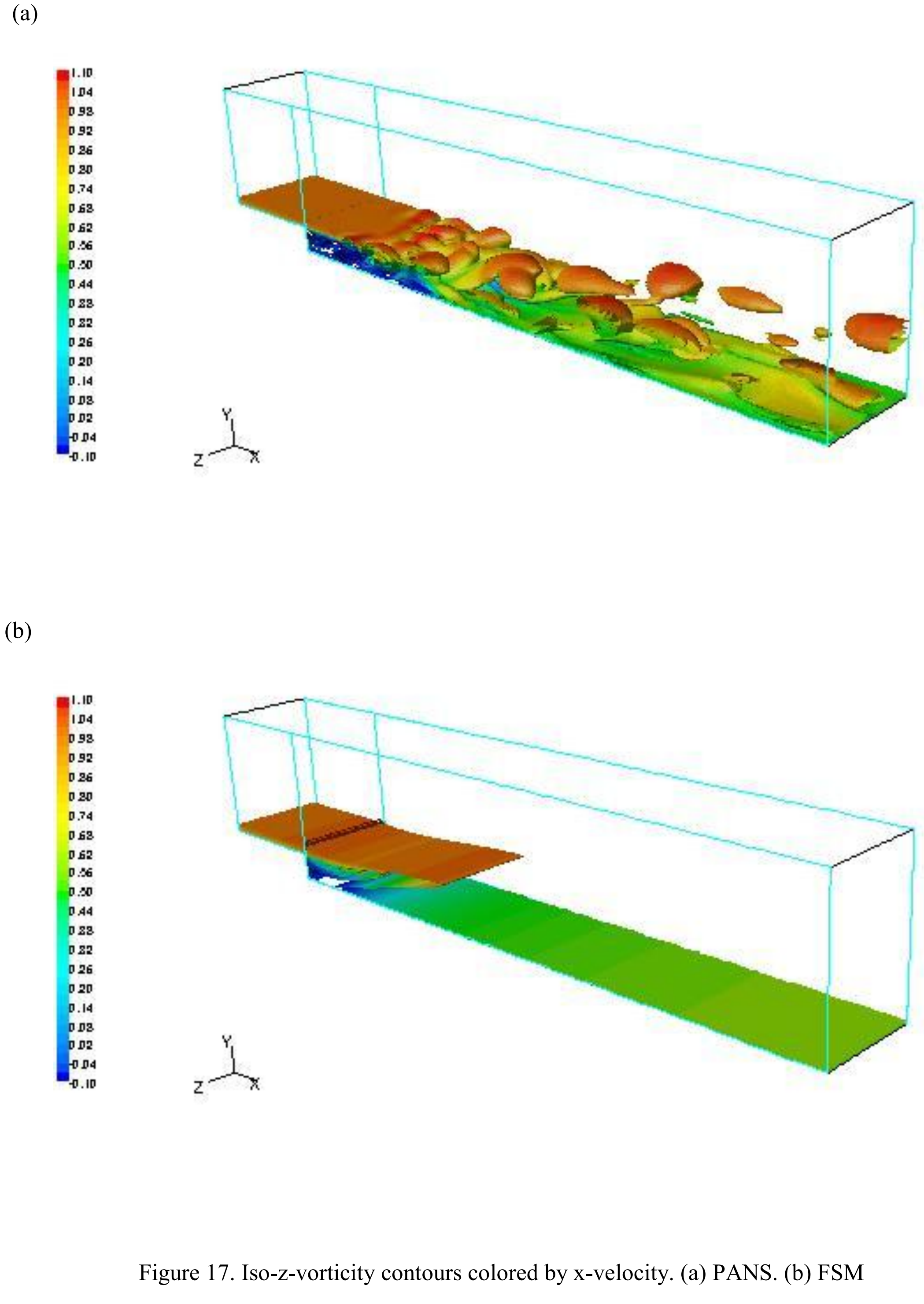

Figure 17. Iso-z-vorticity contours colored by x-velocity. (a) PANS. (b) FSM

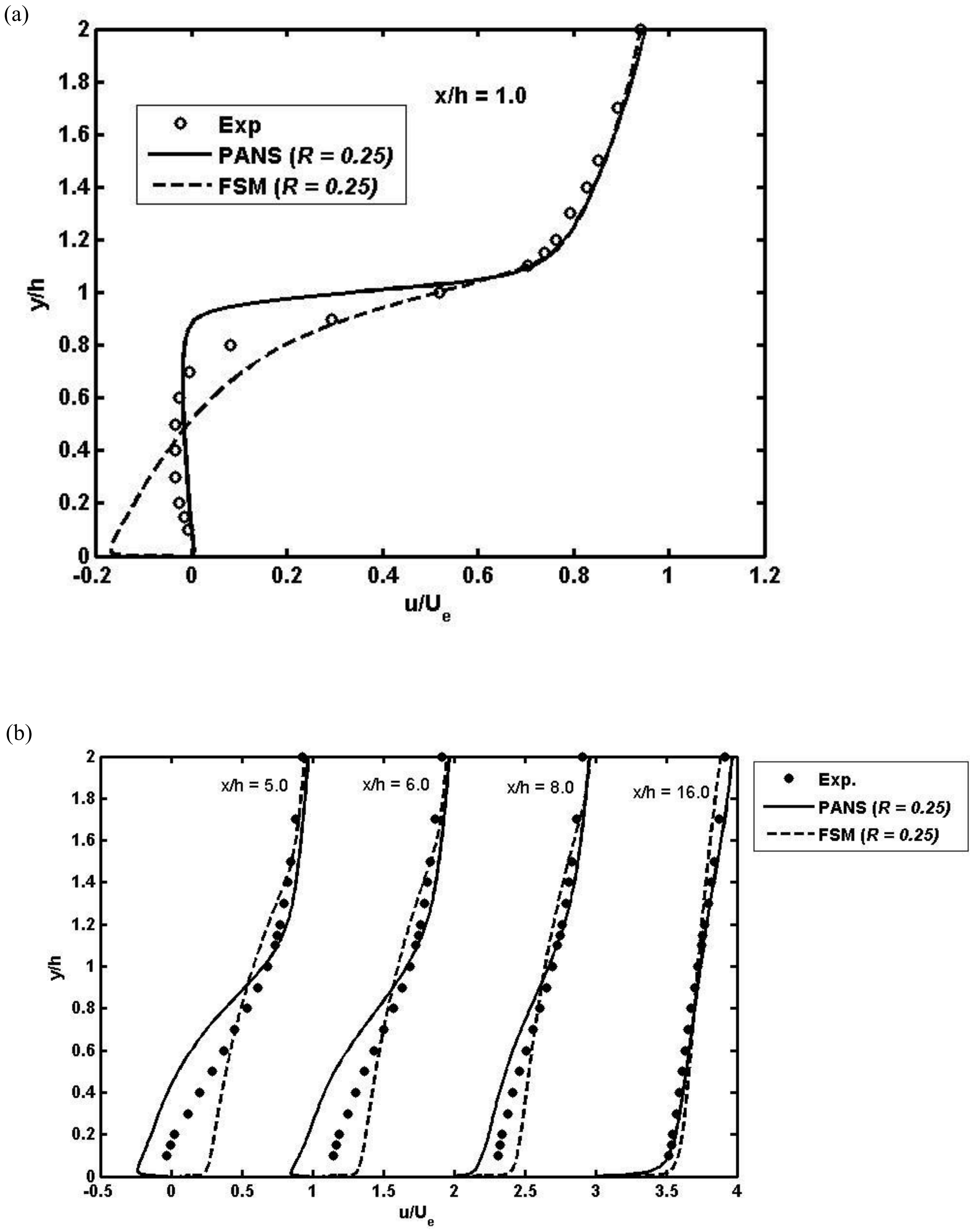

Figure 18. Comparison between PANS and FSM. (a) Streamwise x-velocity at x/H = 1.0. (b). Mean streamwise velocity at various x-planes

(a)

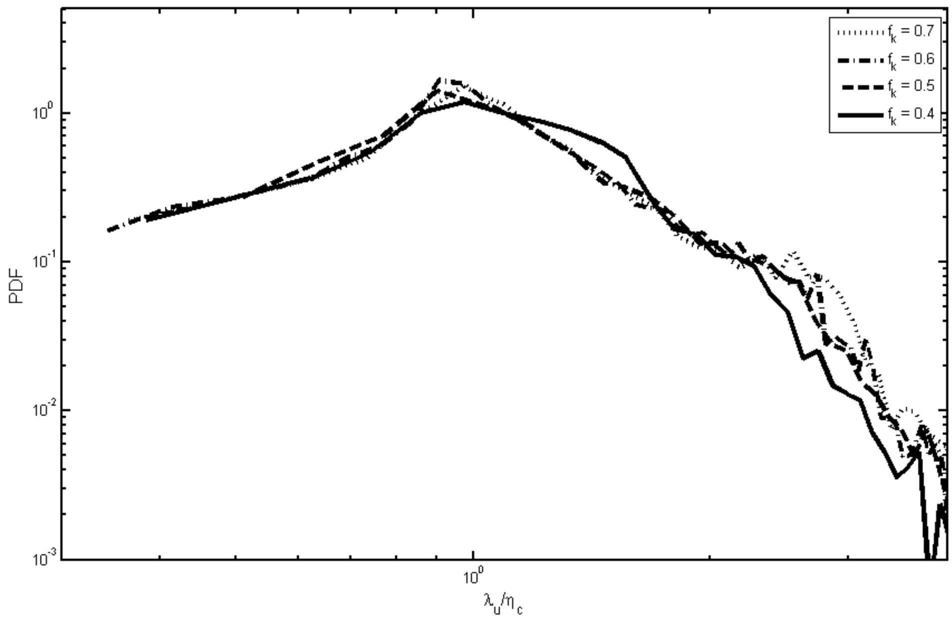

(b)

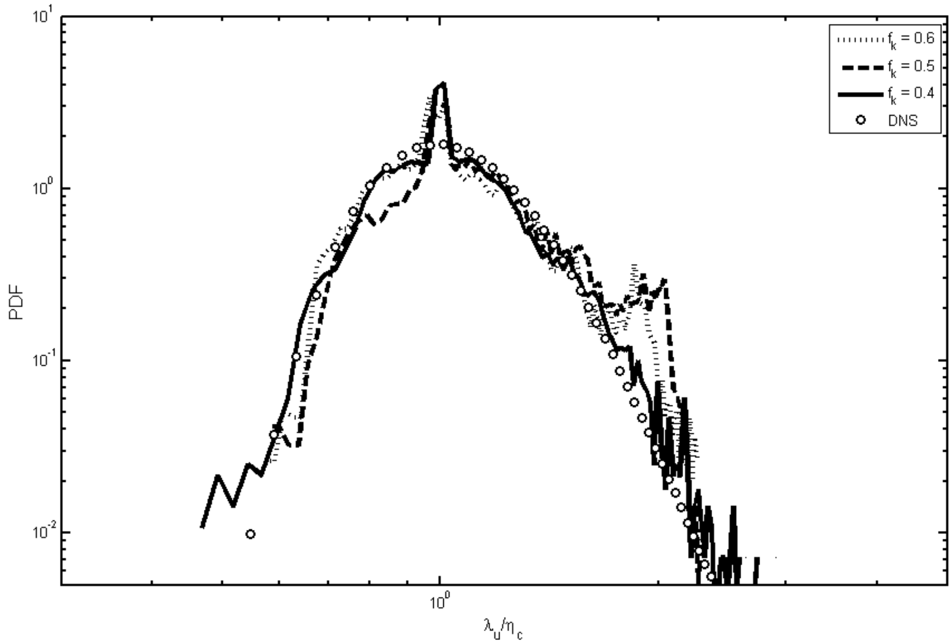

Figure 19. PDF of λ_u/η_c for various f_k values. (a) Cylinder flow simulations. (b) BFS simulations

(a)

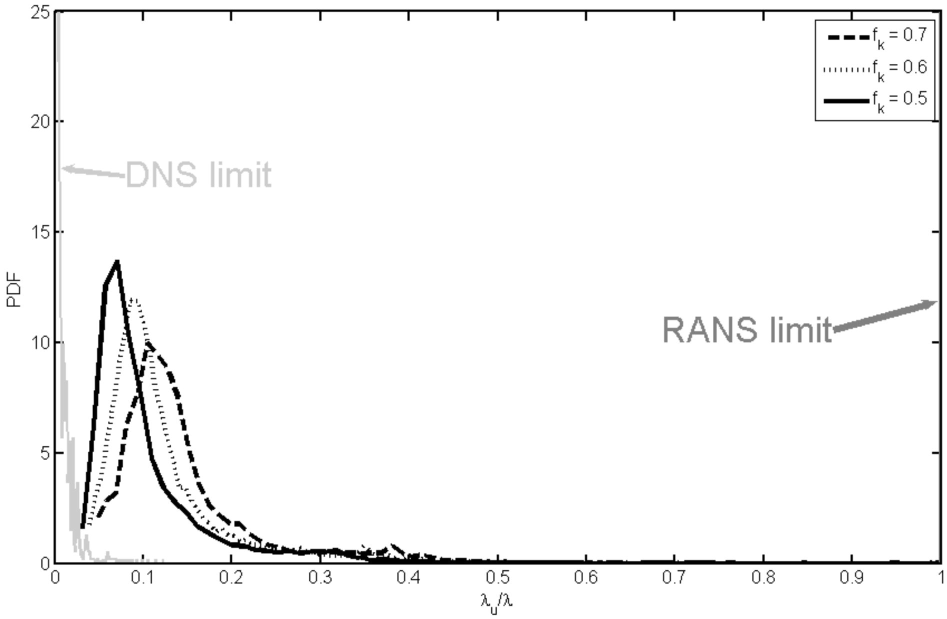

(b)

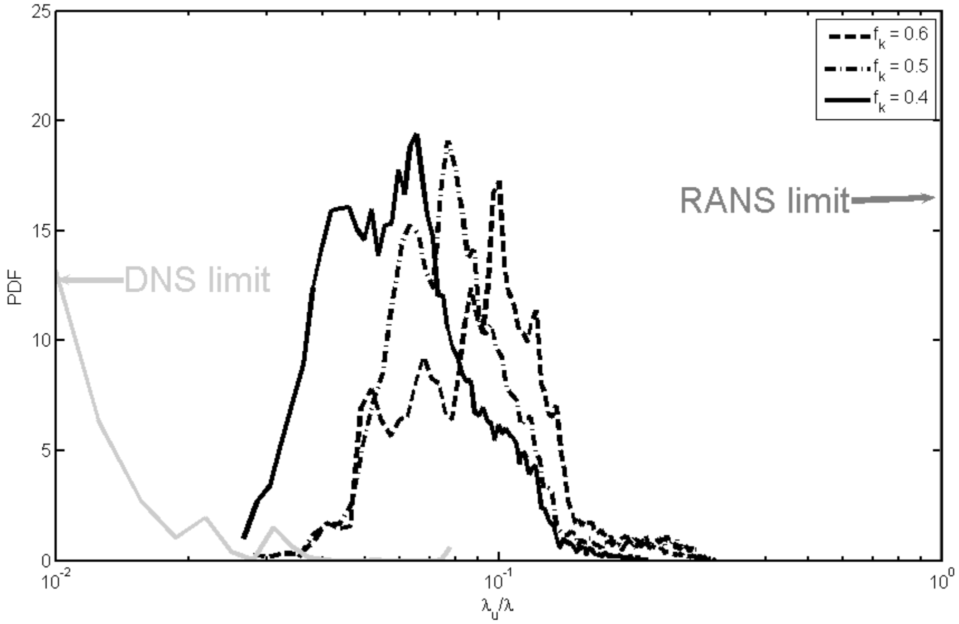

Figure 20. PDF of λ_u/λ for various f_k values. (a) Cylinder flow simulations. (b) BFS simulations

(a)

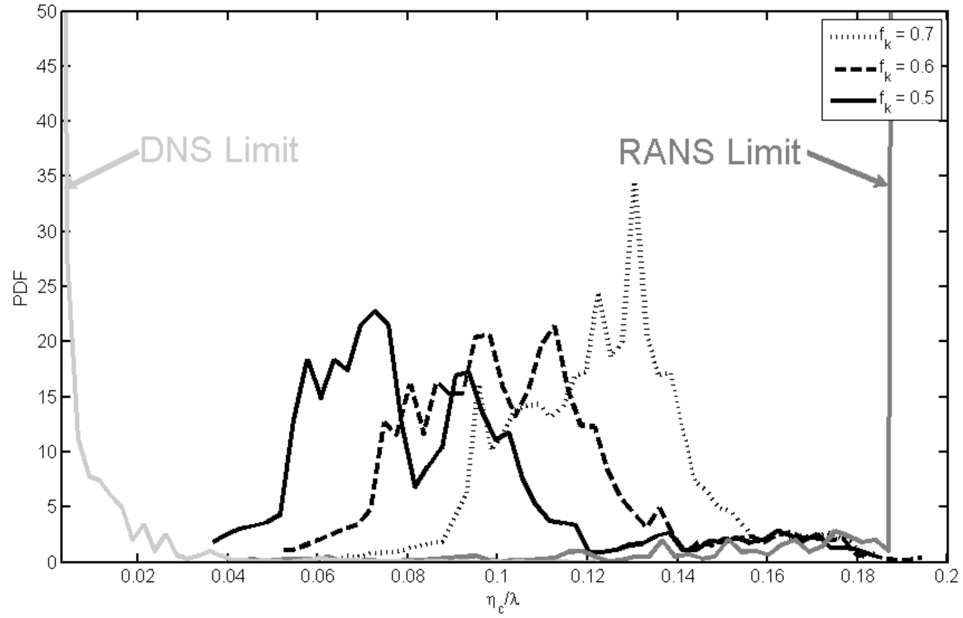

(b)

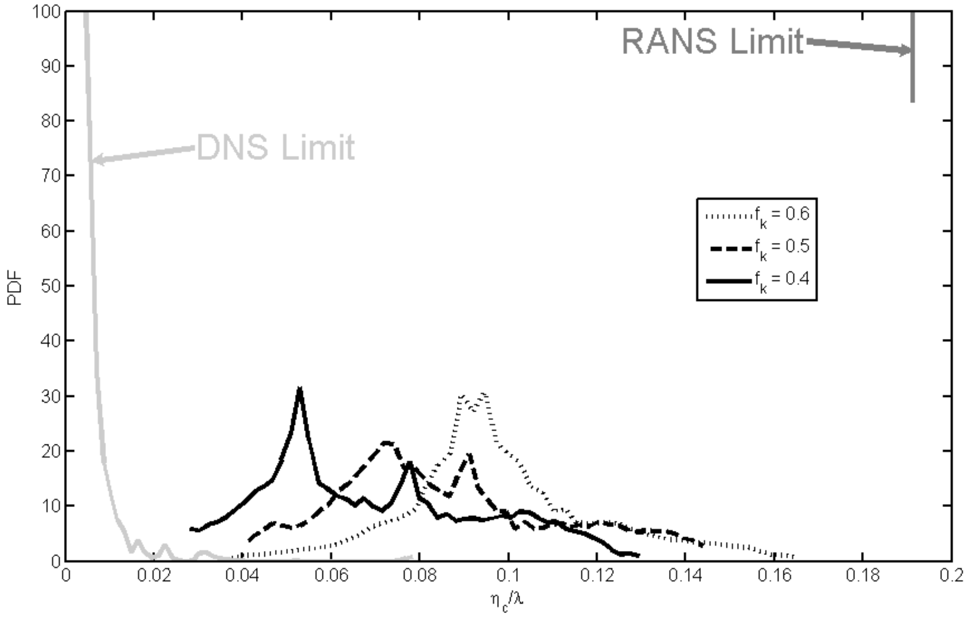

Figure 21. PDF of η_c/λ for various f_k simulations. (a) Cylinder flow simulations. (b) BFS simulations

(a)

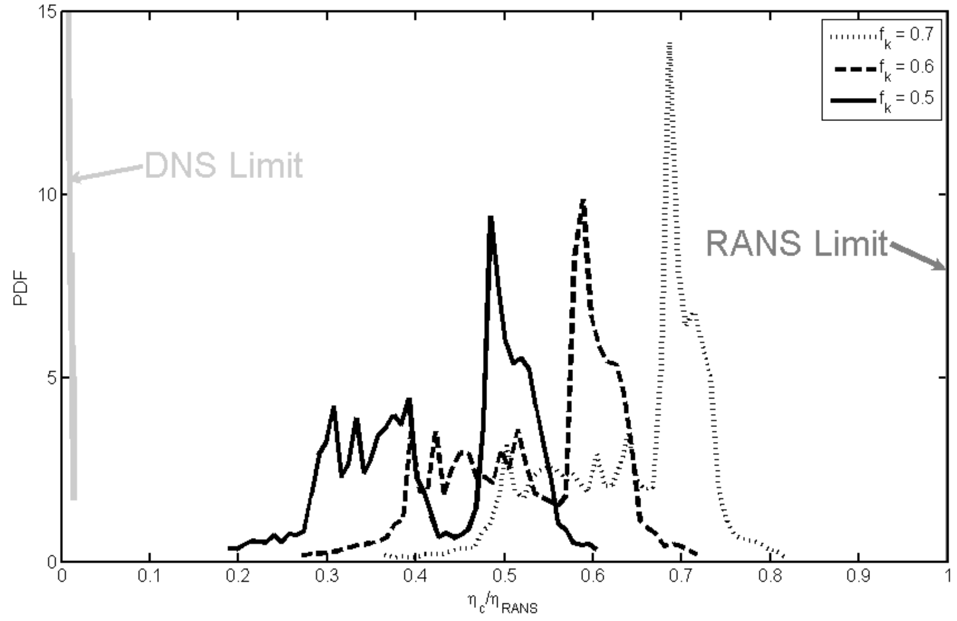

(b)

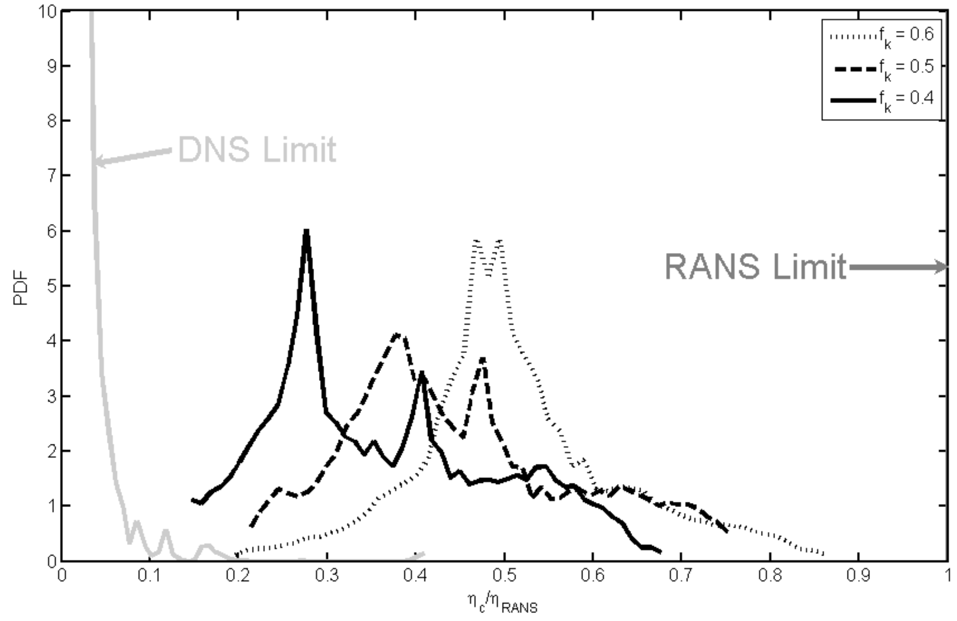

Figure 22. PDF of η_c/η_{RANS} for various *f*$_k$ values. (a) Cylinder flow simulations. (b) BFS simulations

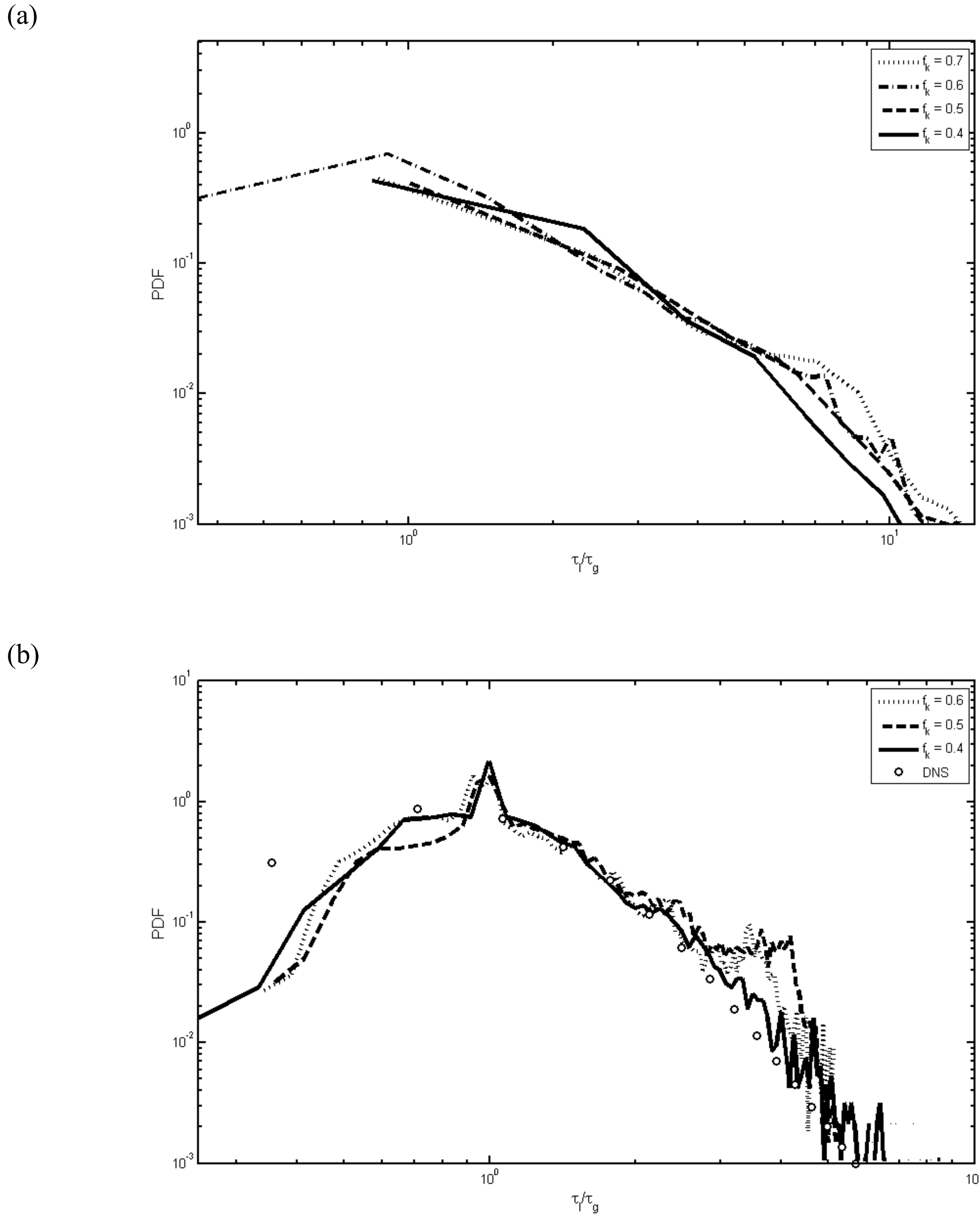

Figure 23. PDF of τ_l/τ_g for various f_k values. (a) Cylinder flow simulations. (b) BFS simulations

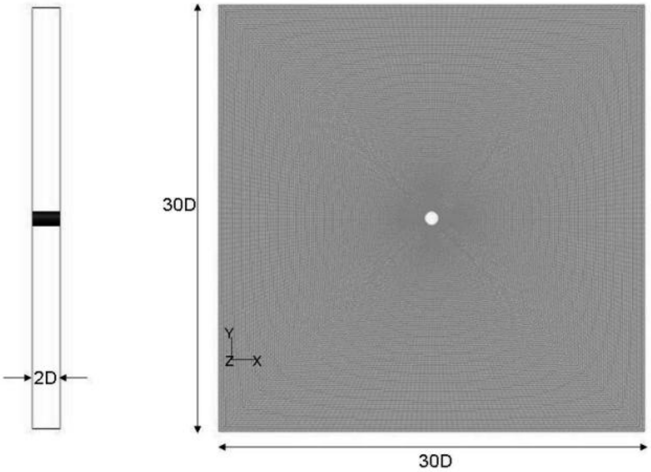

Figure 24. Computational domain for cylinder flow simulations

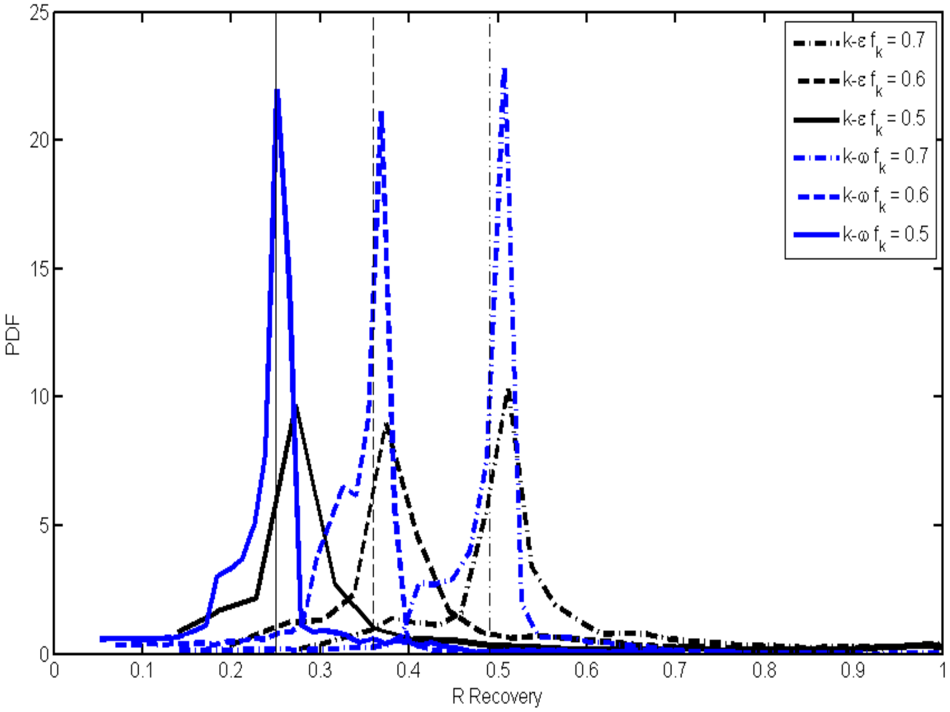

Figure 25. PDFs comparing viscosity ratio recovery for PANS k_u-ε_u and PANS k_u-ω_u

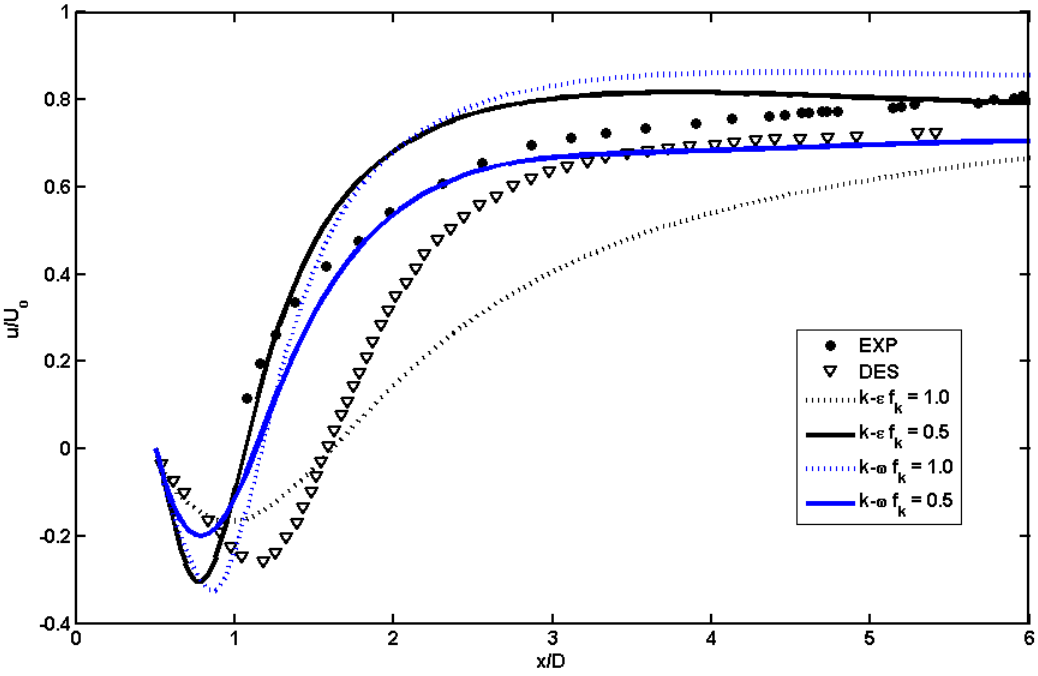

Figure 26. Mean streamwise velocity statistics along the wake centerline

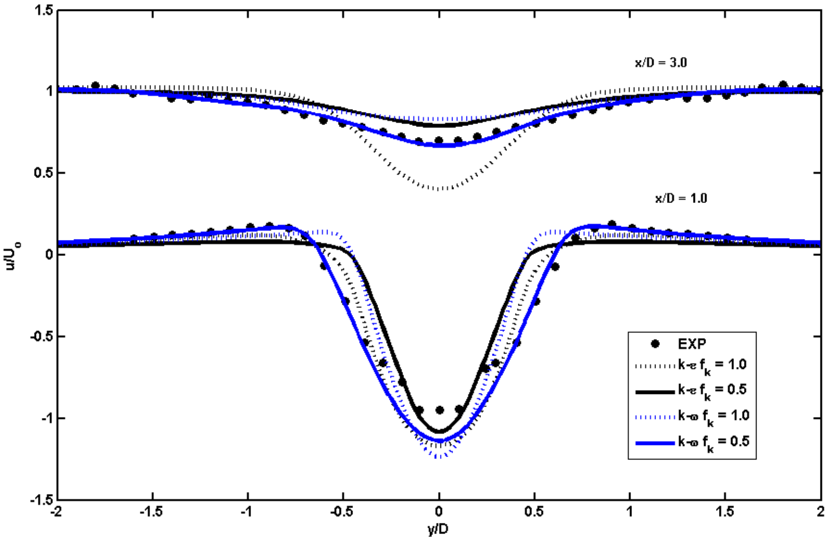

Figure 27. Mean streamwise velocity statistics at various locations in the near wake

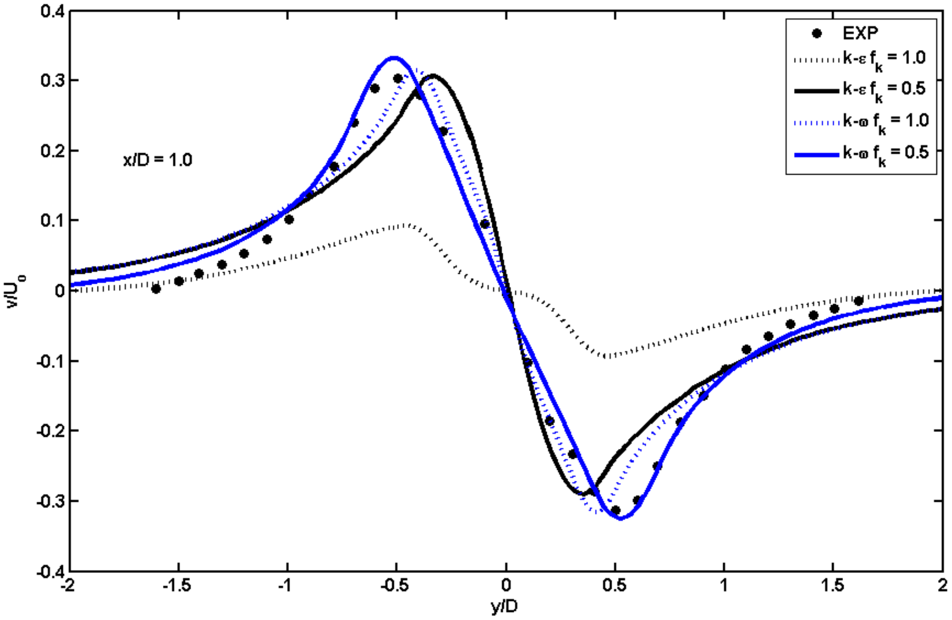

Figure 28. Mean normal velocity at x/D = 1.0

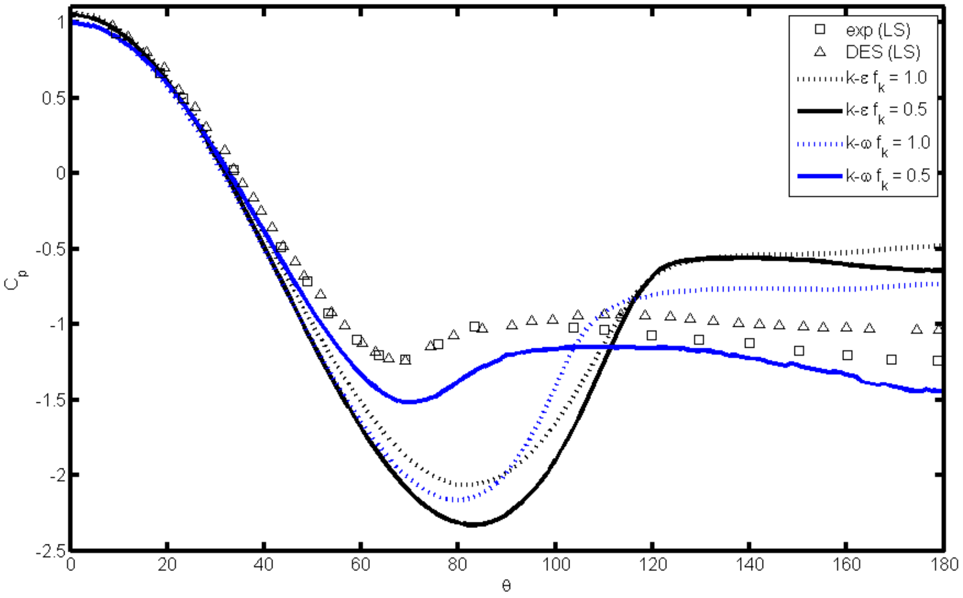

Figure 29. Coefficient of pressure distribution along the cylinder surface

Table 3. Mean integral quantities for cylinder flow simulations

Case	**Grid Resolution**	C_d	C_{pb}	S_t	θ_s
Exp. [18] (LS)		1.237	-1.21	0.179	77^o
DES [35] (LS8)	150 x 109 x 42	1.08	-1.04	0.21	77^o
Exp. (TS)		0.62 – 0.74	-0.85	0.28	110^o
DES [35] (TS5)	150 x 109 x 42	0.65	-0.7	0.28	93^o
PANS (fk = 1.0 (k-ε)	240 x 320 x 32	–	-0.48	–	108.4^o
PANS (f_k = 0.5) (k-ε)	240 x 320 x 32	0.67	-0.64	0.274	110.4^o
PANS (f_k = 1.0) (k-ω)	240 x 320 x 32	0.59	-0.737	0.272	101.3^o
PANS (f_k = 0.5) (k-ω)	240 x 320 x 32	1.18	-1.44	0.202	83.4^o

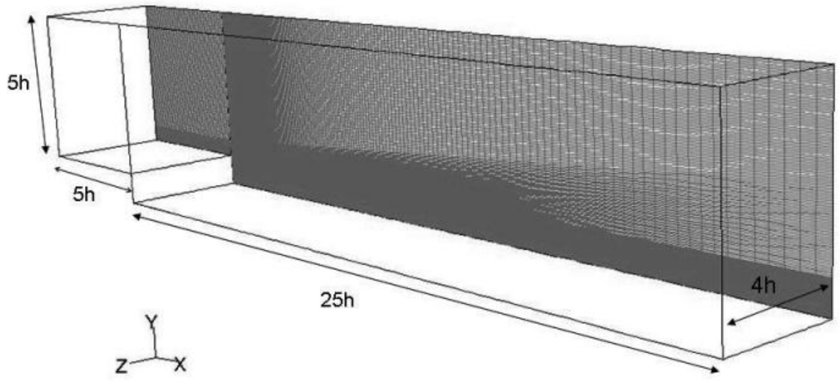

Figure 30. Computational domain for the BFS simulations

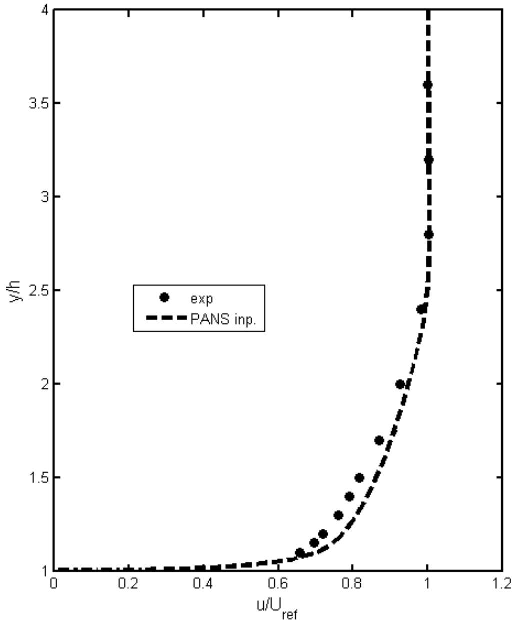

Figure 31. Velocity input profile for PANS

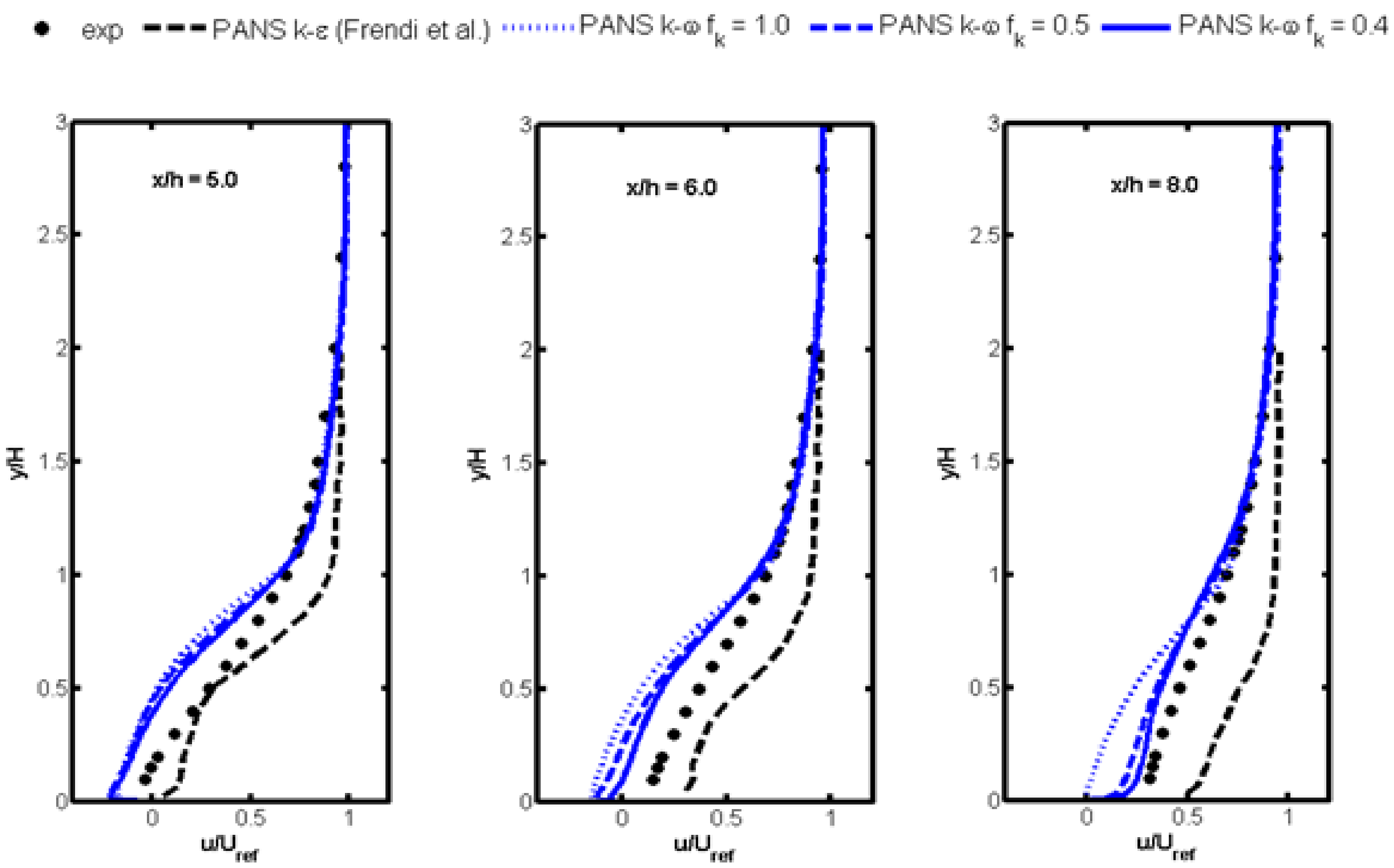

Figure 32. Spanwise-averaged mean x-velocity statistics at various downstream locations

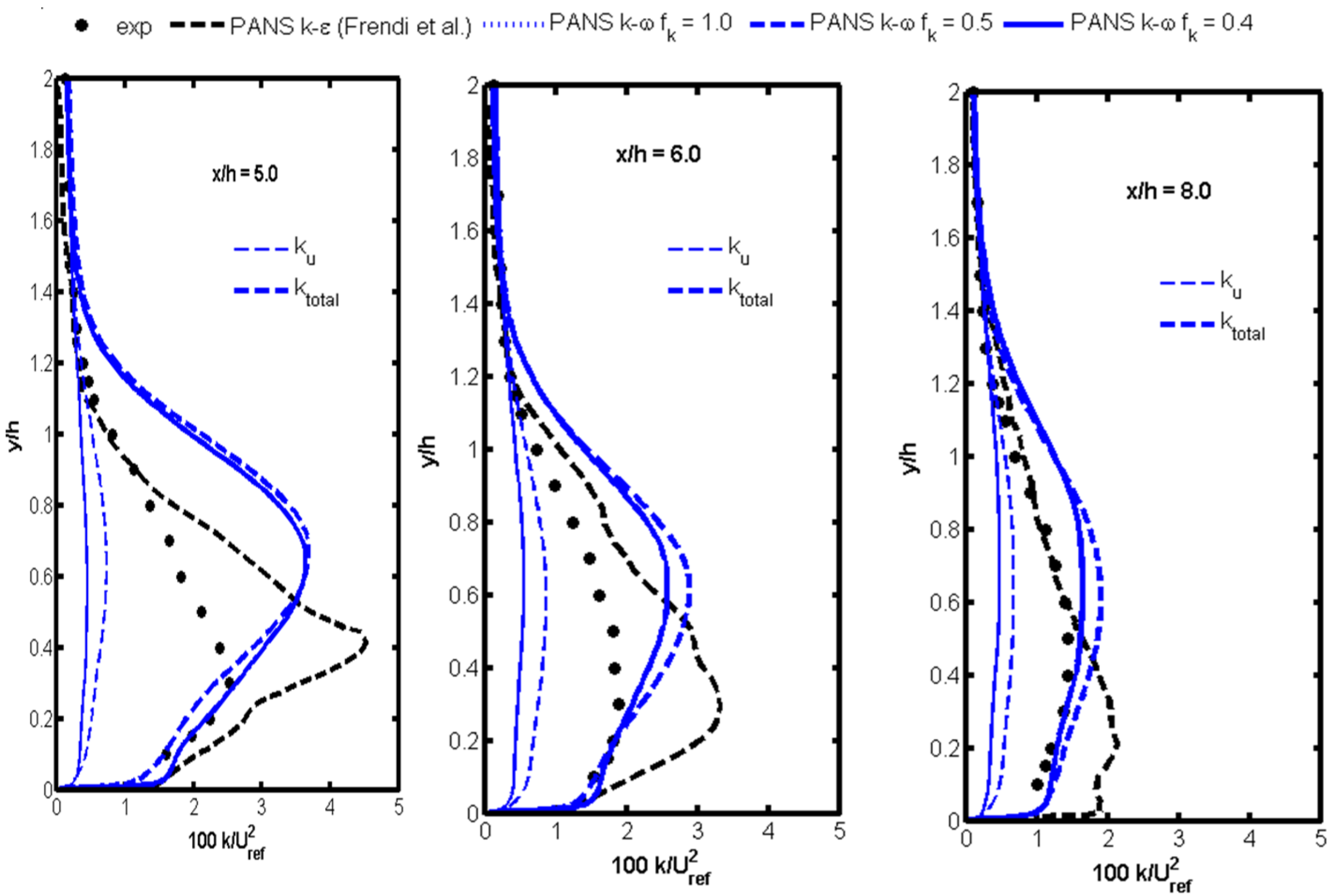

Figure 33. Time-averaged mean turbulent kinetic energy profiles

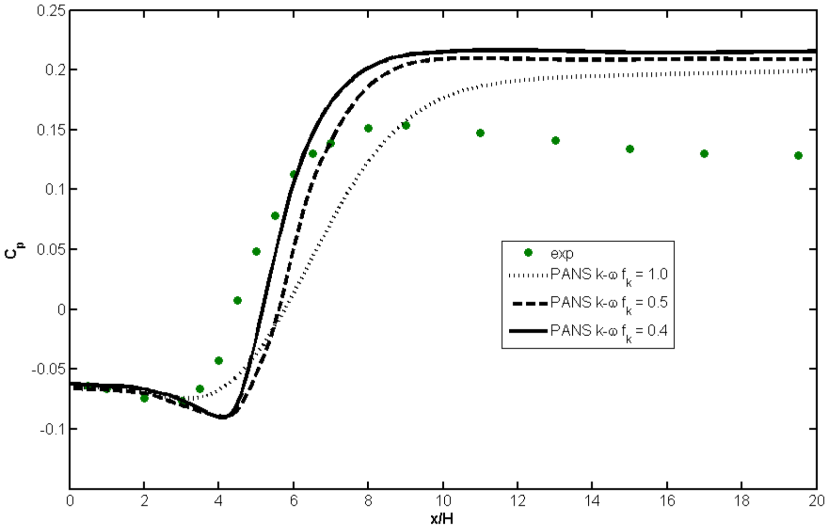

Figure 34. C_p distribution along the step-side wall

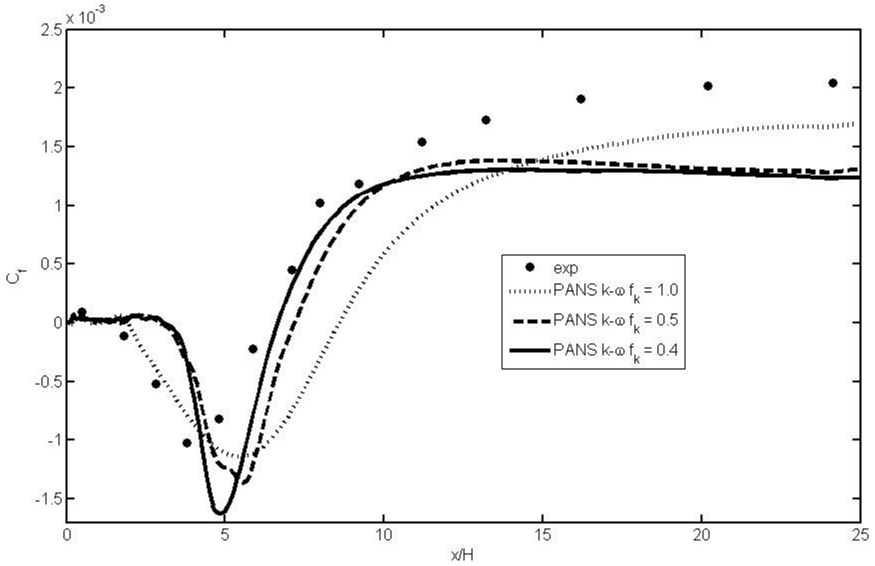

Figure 35. C_f distribution along the step-side wall

Table 4. Comparison of reattachment length for various PANS calculations

	f_k = 0.4 (k-ω)	**f_k = 0.5 (k-ω)**	**f_k = 1.0 (k-ω)**	**Exp.**
x_r (x/h)	6.58	7.15	8.57	6.26

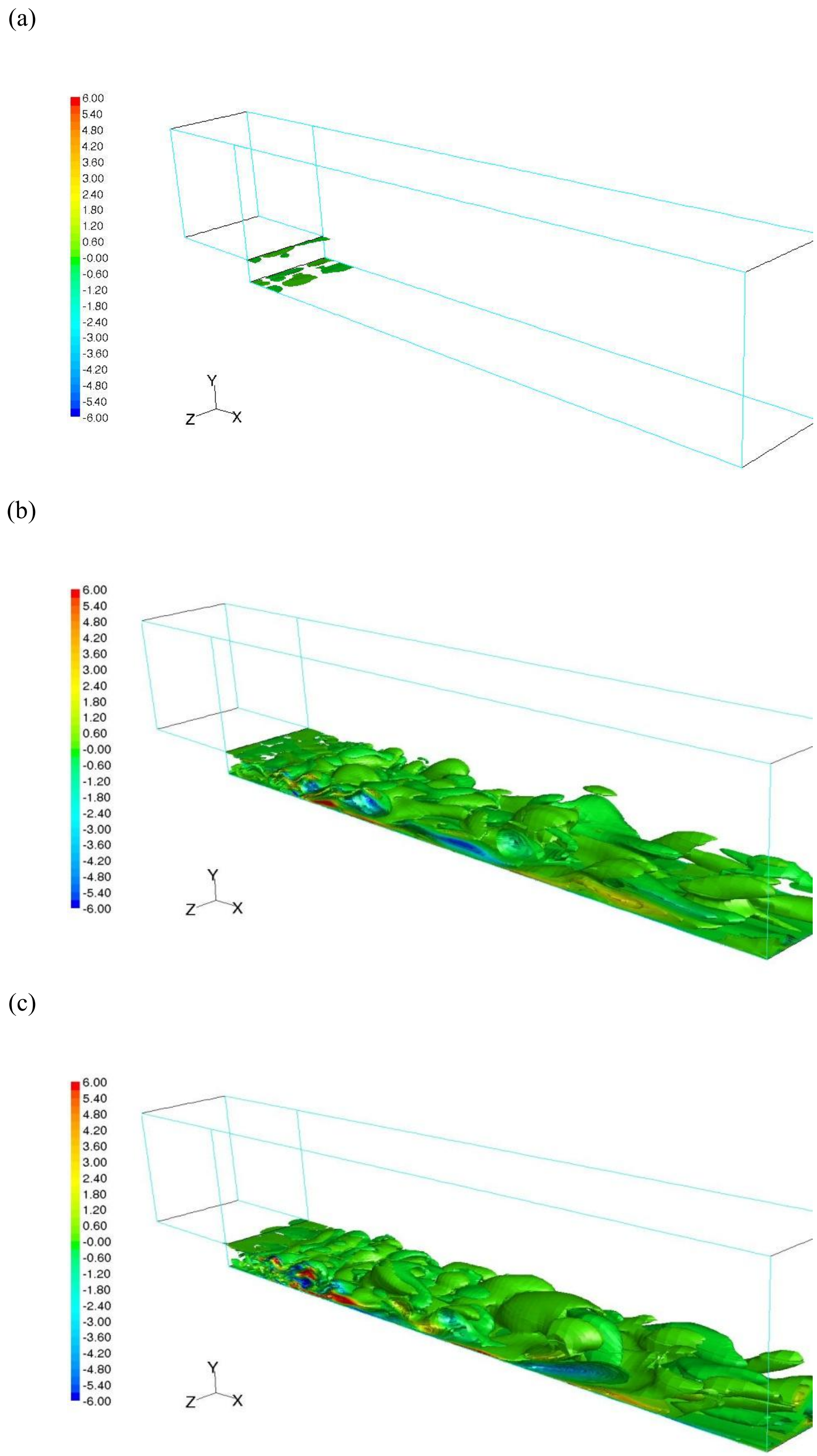

Figure 36. Instantaneous iso-x-vorticity contours for various f_k values. (a) $f_k = 1.0$.(b) $f_k = 0.5$. (c) $f_k = 0.4$.

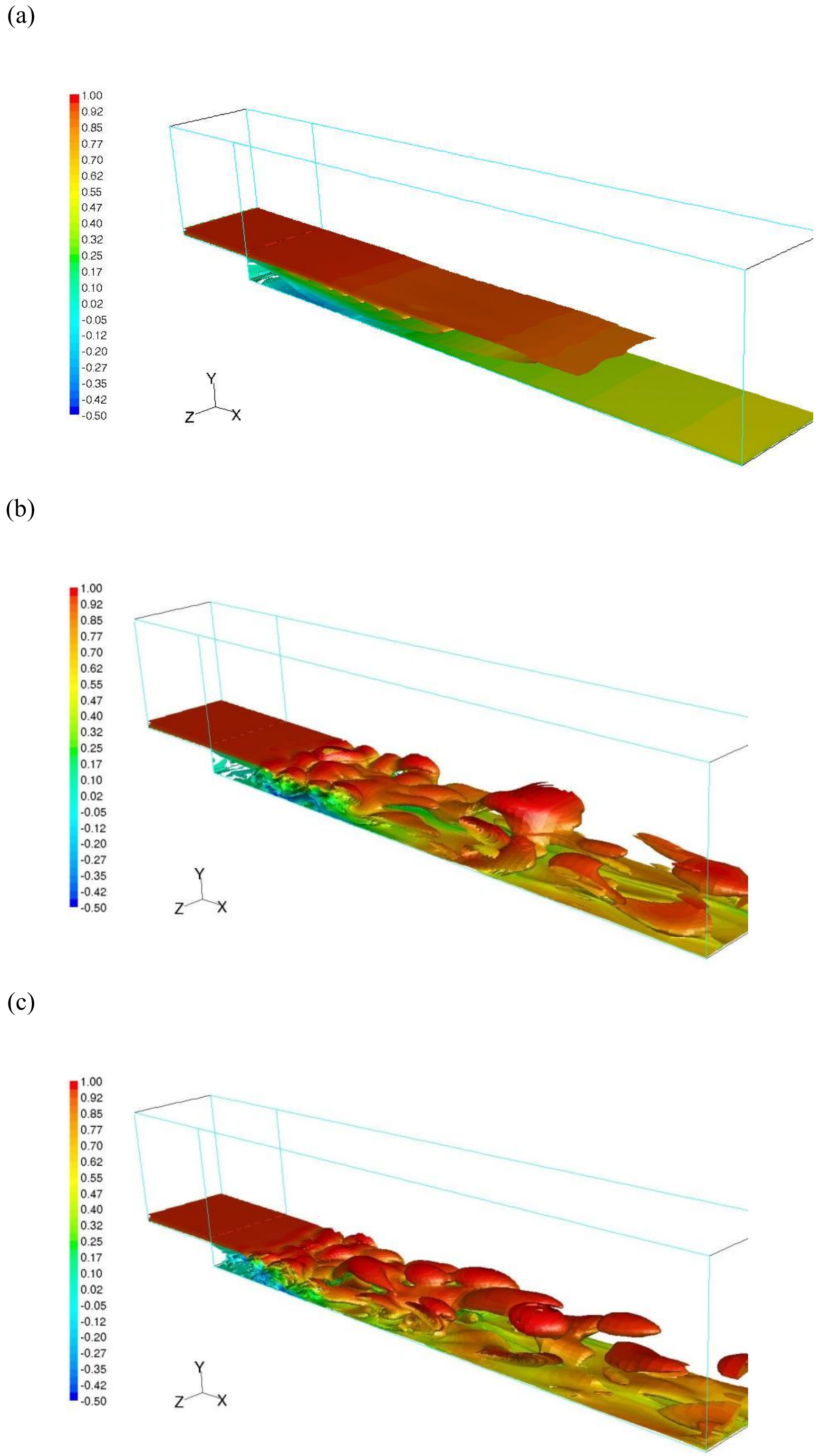

Figure 37. Instantaneous iso-z-vorticity contours for various f_k values. (a) $f_k = 1.0$.(b) $f_k = 0.5$. (c) $f_k = 0.4$

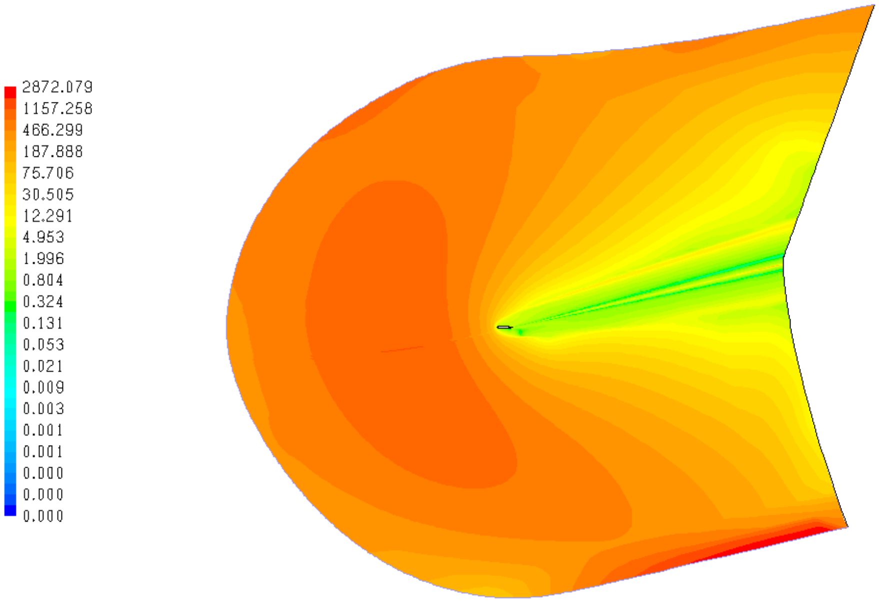

Figure 38. Contours of *Sk/ε* for the entire airfoil computational domain

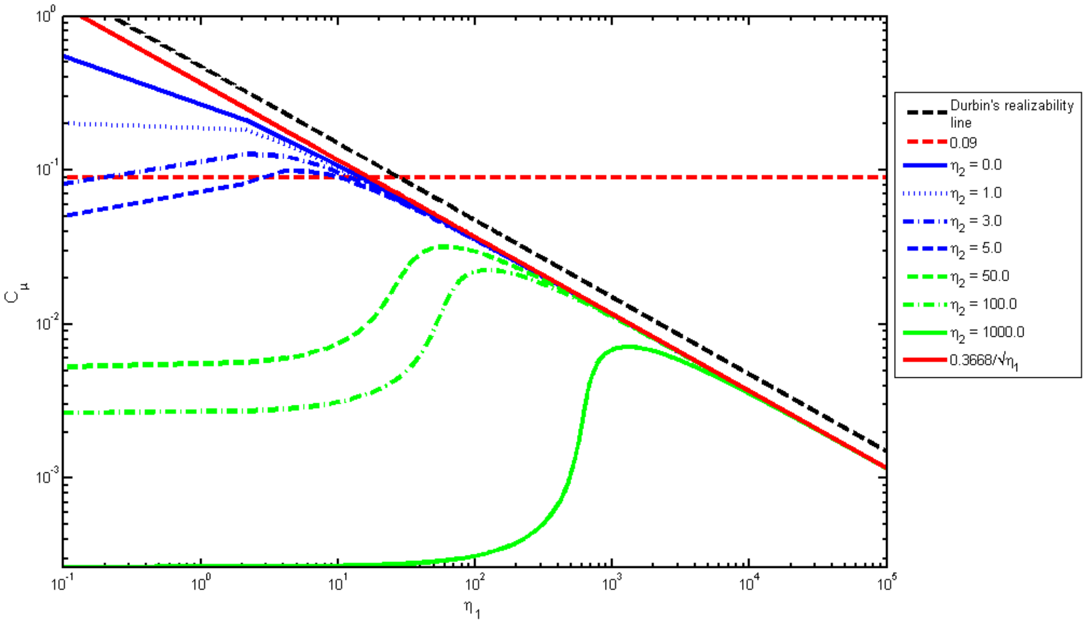

Figure 39. Variation of C_μ as a function η_1 for various η_2

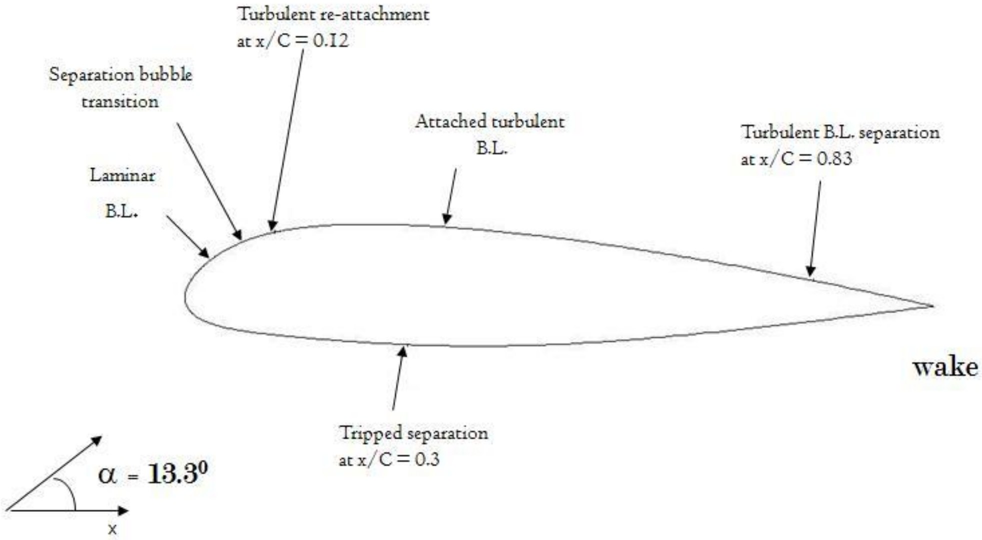

Figure 40. Aerospatiale A-airfoil geometry and flow features

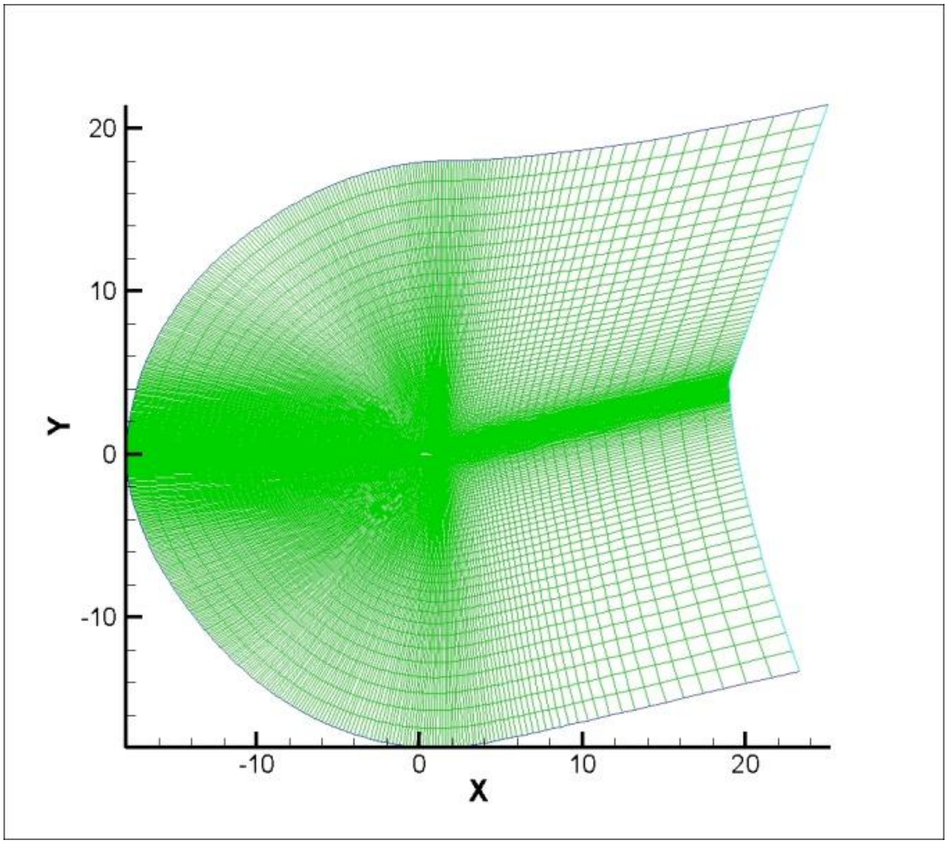

Figure 41. Computational grid for the A-airfoil

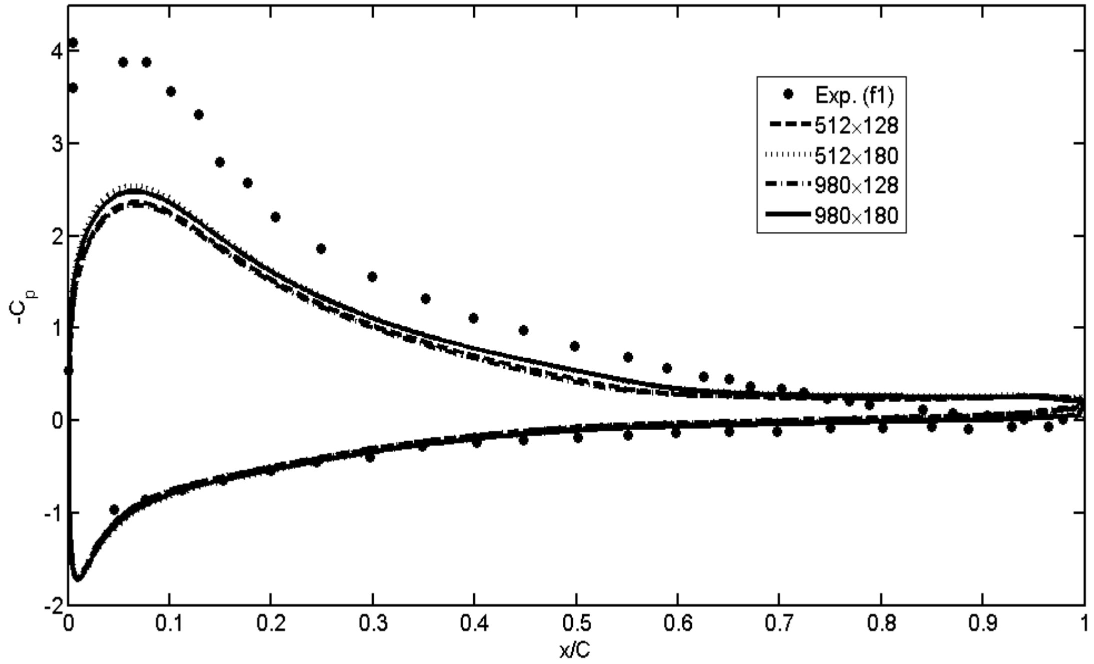

Figure 42. C_p distribution along the airfoil surface for various grids (Std. k-ω model)

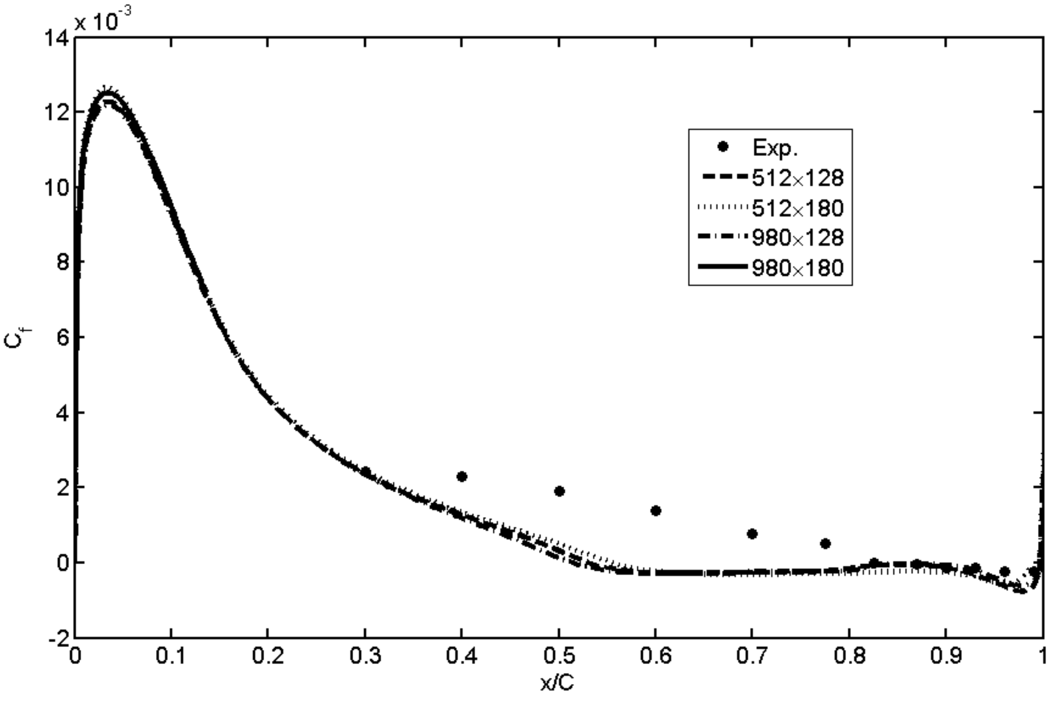

Figure 43. C_f distribution on the suction side for various grids (Std. k-ω model)

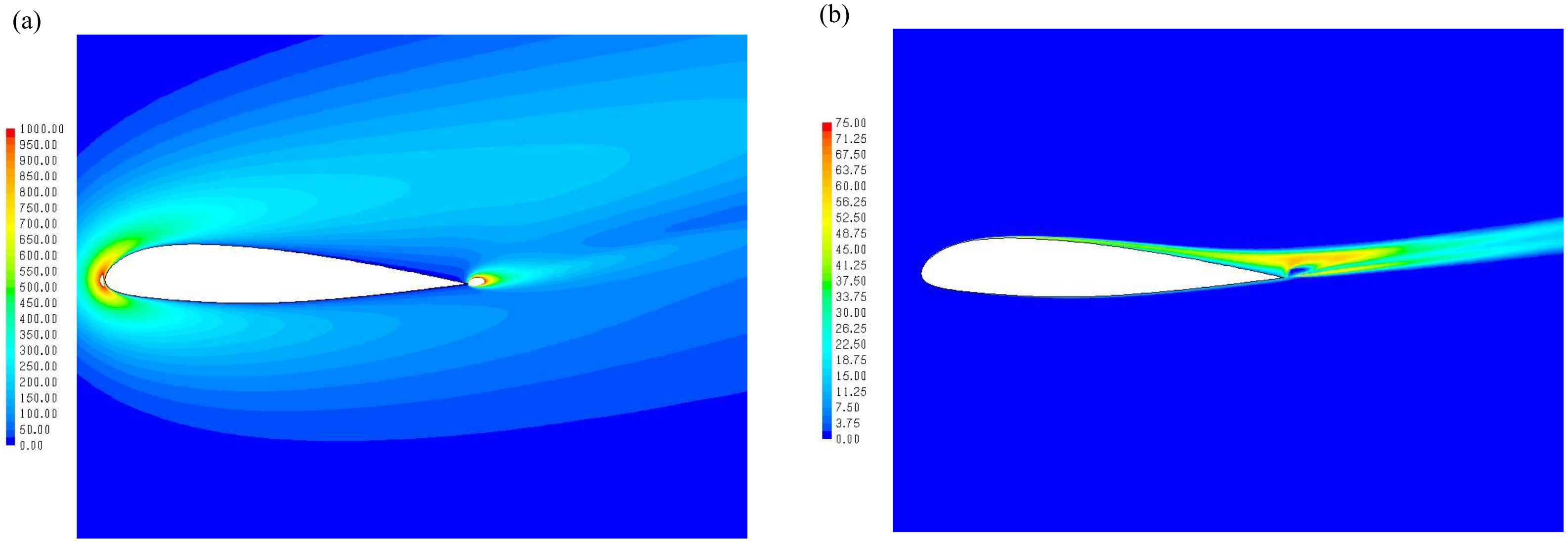

Figure 44. Contours of turbulent kinetic energy. (a) Std. EVM. (b) Variable C_μ EVM.

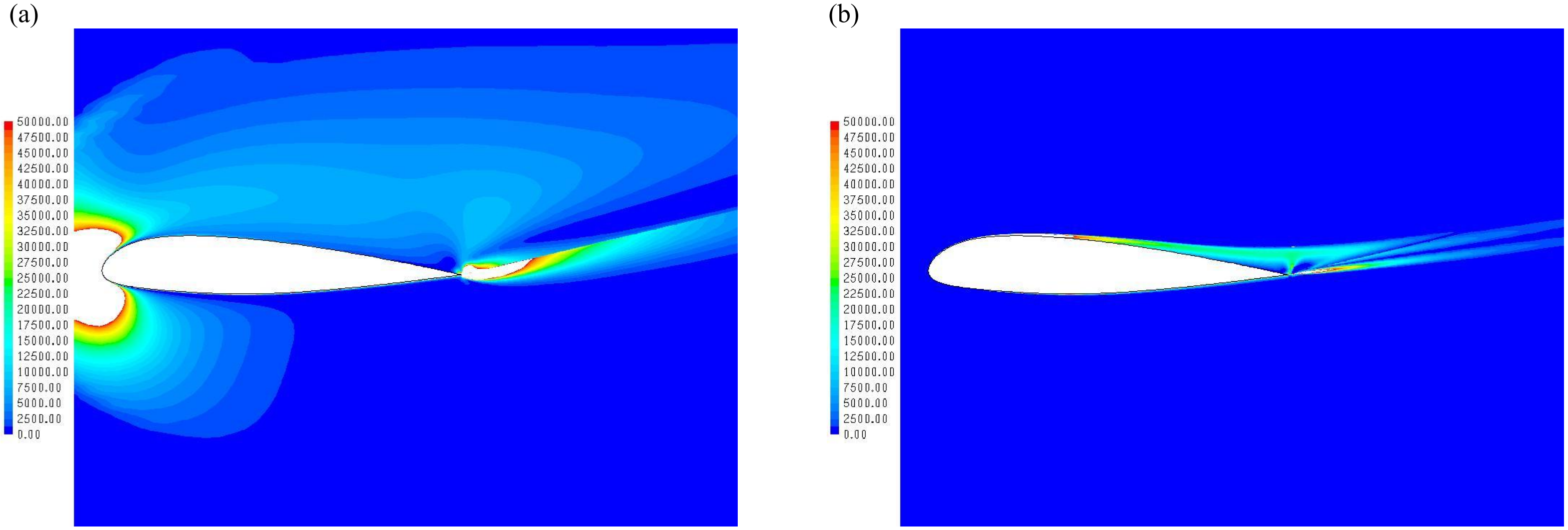

Figure 45. Contours of Production of turbulence. (a) Std. EVM. (b) Variable C_μ EVM.

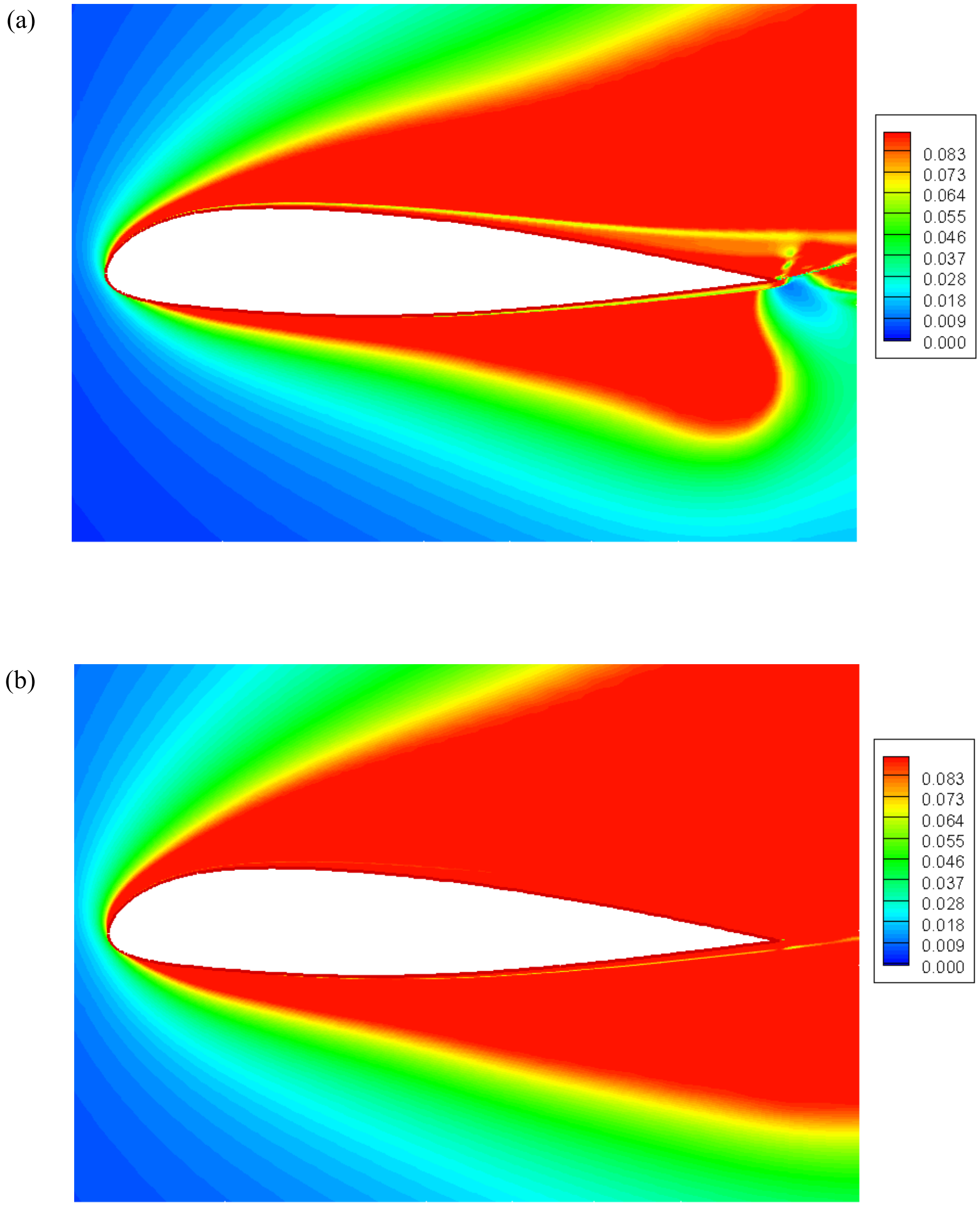

Figure 46. Contours of C_μ variation for different models. (a) k-ω Var. C_μ (1). (b) k-ω Var. C_μ (2)

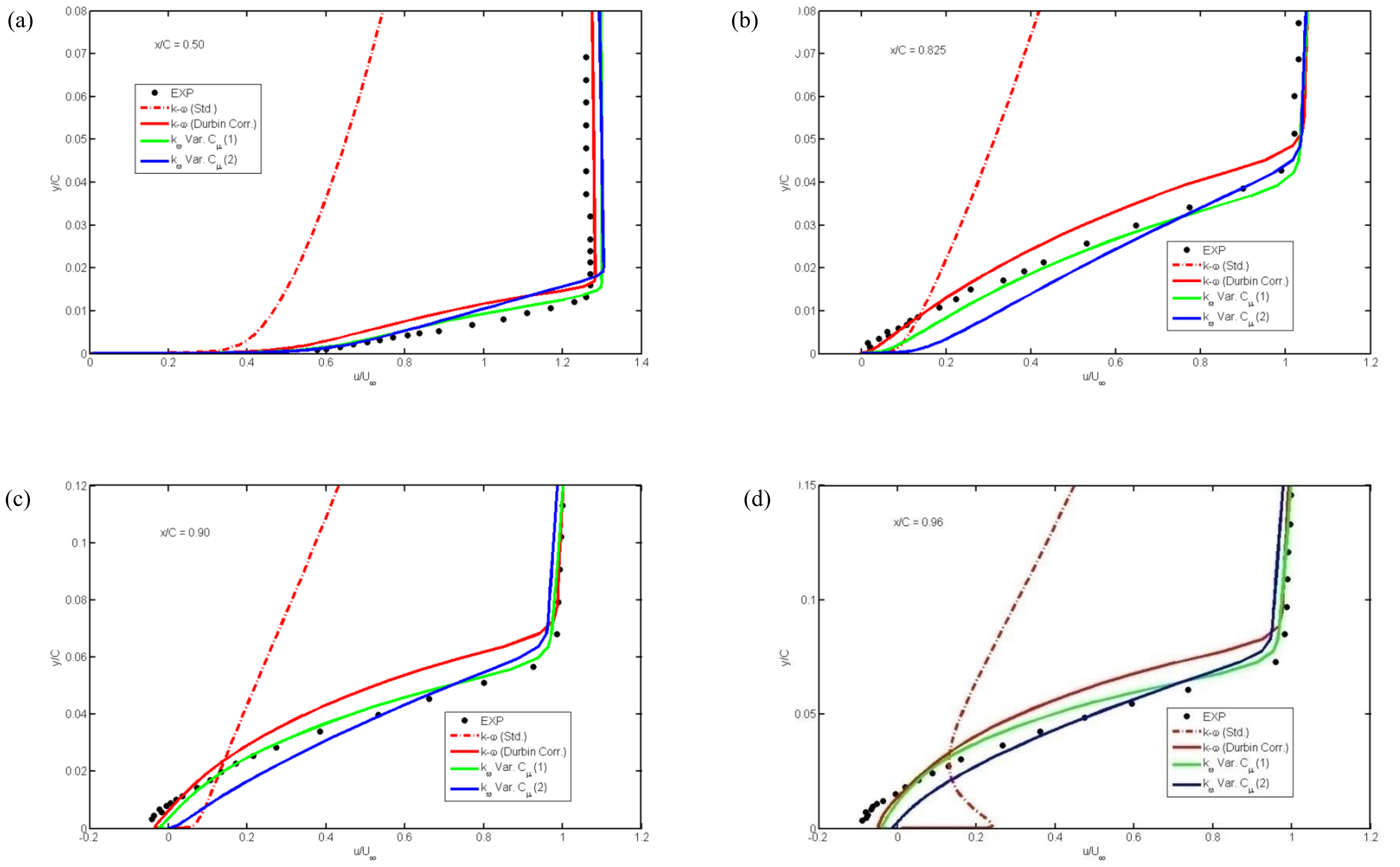

Figure 47. Normalized velocity profiles at various stations on the suction side of airfoil. (a) x/C = 0.5. (b) x/C = 0.825. (c) x/C = 0.9. (d) x/C = 0.96

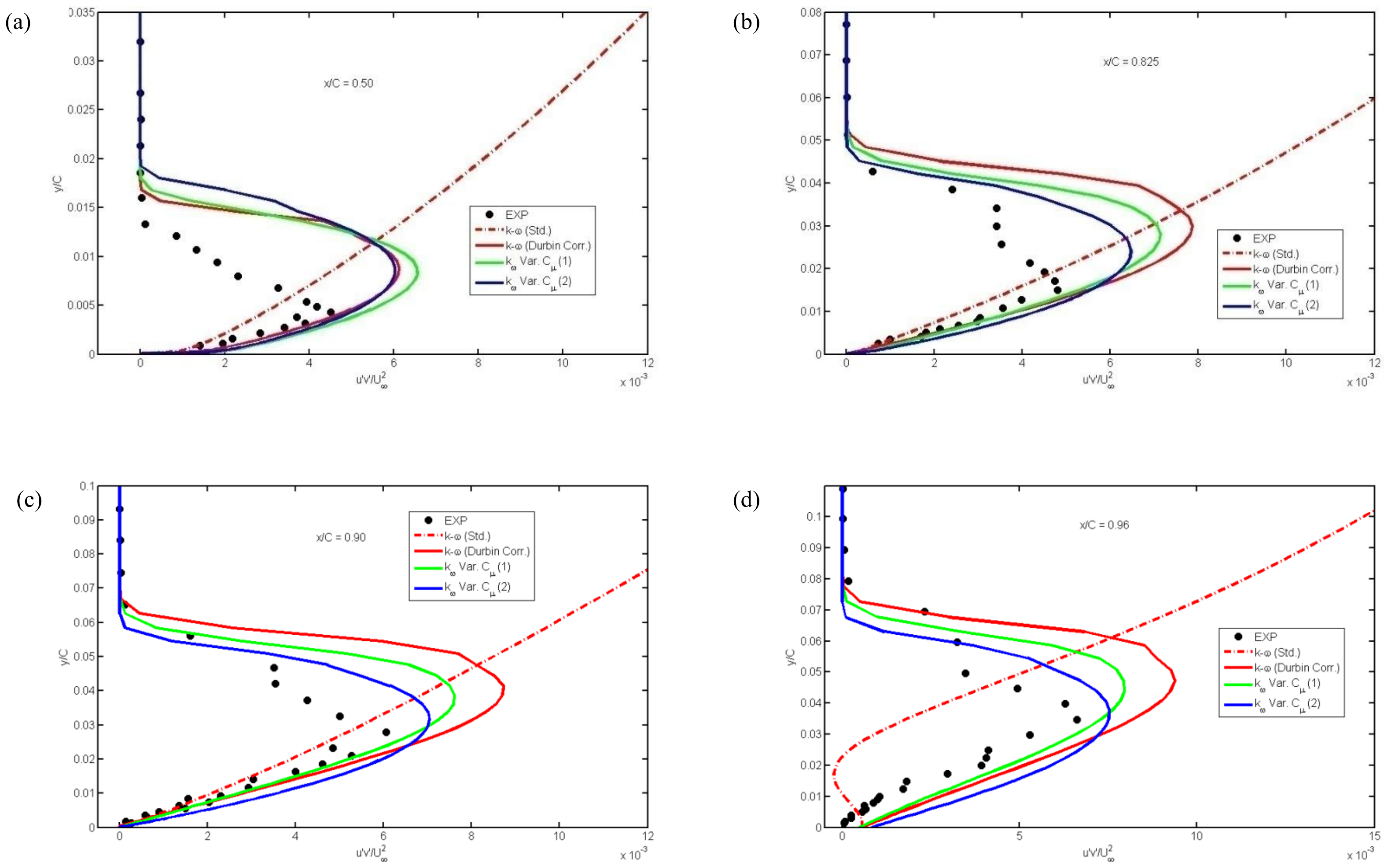

Figure 48. Normalized Reynolds stress $u'v'$ at various stations on the suction side of airfoil. (a) x/C = 0.5. (b) x/C = 0.825. (c) x/C = 0.9. (d) x/C = 0.96

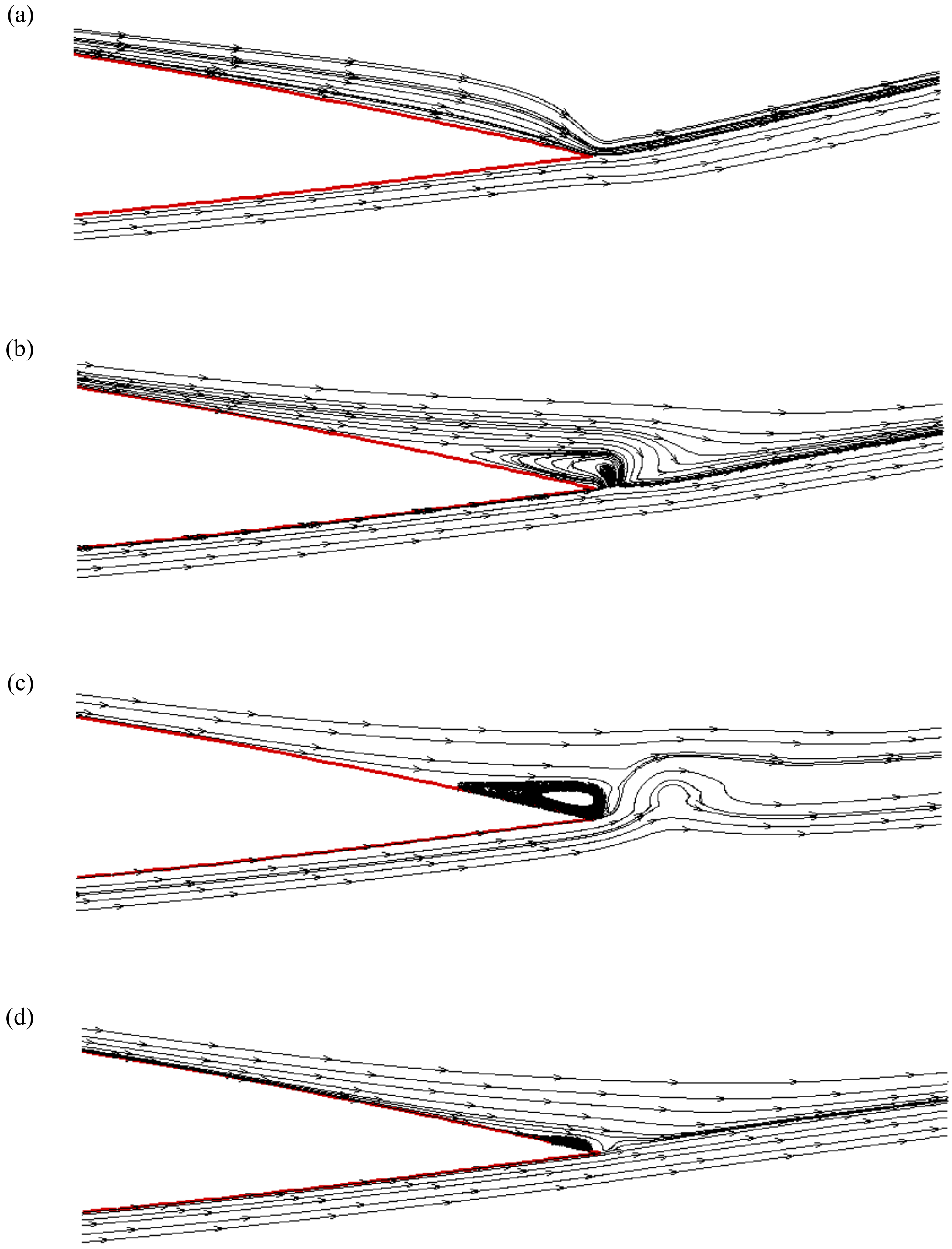

Figure 49. Streamline contours at the trailing edge for various models. (a) k-ω (std.). (b) k-ω (Durbin). (c) k-ω Var. C_μ (1). (d) k-ω Var. C_μ (2).

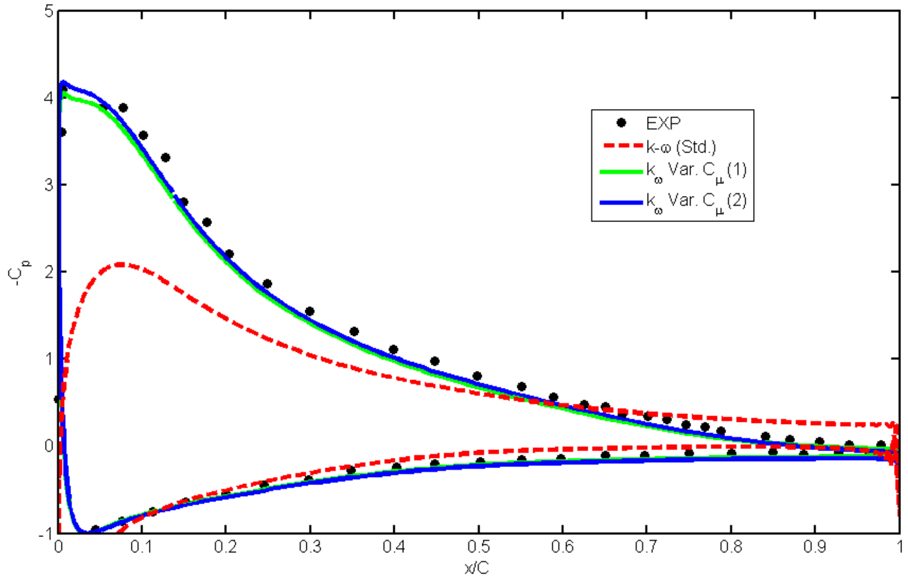

Figure 50. C_p distribution along the airfoil surface from various C_μ computations

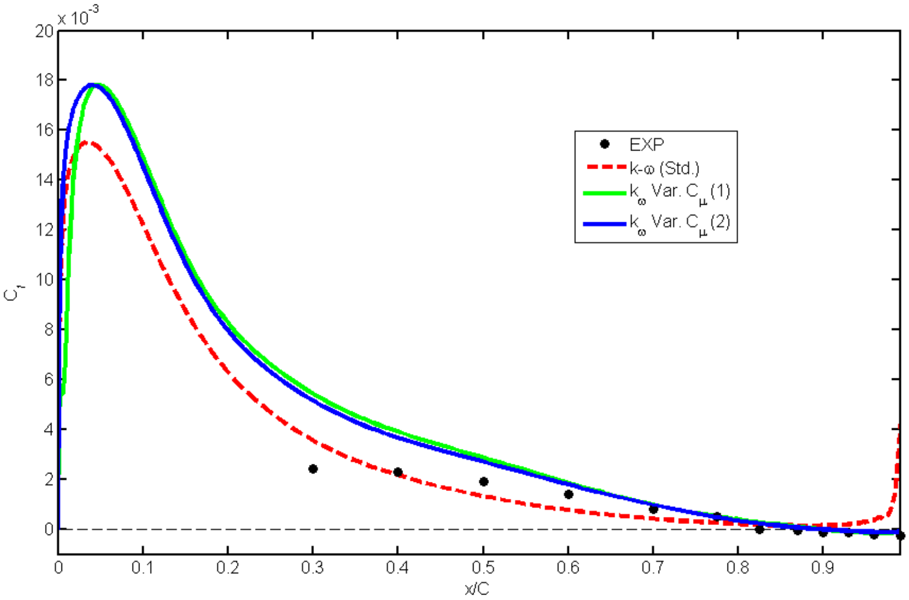

Figure 51. C_f distribution along the airfoil surface from various C_μ computations

Table 5. Numerical discretization schemes

Pressure:	Second-order
Momentum:	Third order MUSCL
Kinetic energy:	Second-order upwind
Specific dissipation	Second-order upwind
Pressure-velocity coupling:	SIMPLEC (5 sub-iterations)

Table 6. Force coefficients

Case	C_D	C_L
Experimental	0.0208 - 0.0212	1.55 – 1.575
Standard k-ω	0.28	1.08
Var. C_μ k-ω (1)	0.0252	1.492
Var. C_μ k-ω (2)	0.0248 – 0.0256	1.534 – 1.542

VITA

Name: Sunil Lakshmipathy

Address: Department of Aerospace Engineering, Texas A&M University
Mail Stop #3141, College Station, Texas 77843

Email Address: sunil_l@tamu.edu

Education: B.E., Mechanical Engineering, Bangalore University, 2000
M.S., Aerospace Engineering, Texas A&M University, 2004
Ph.D., Aerospace Engineering, Texas A&M University, 2009